Functional materials for MEMS based gas sensors

Ramachandrappa Venkatesh, M.

DOI
10.4233/uuid:5bef3e79-1cab-411d-86dd-b9a518628824

Publication date
2022

Document Version
Final published version

Citation (APA)
Ramachandrappa Venkatesh, M. (2022). *Functional materials for MEMS based gas sensors*. [Dissertation (TU Delft), Delft University of Technology]. https://doi.org/10.4233/uuid:5bef3e79-1cab-411d-86dd-b9a518628824

Functional Materials for MEMS based gas sensors

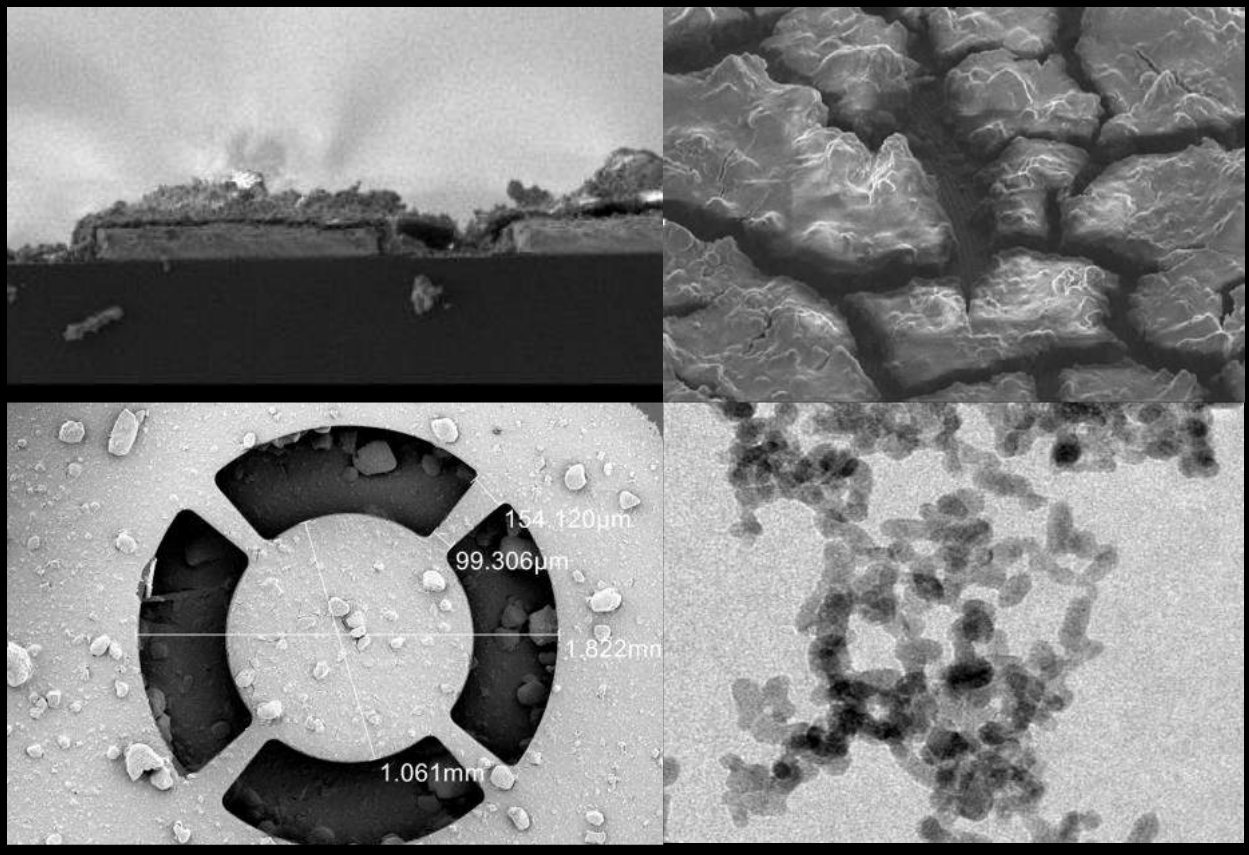

Manjunath Ramachandrappa Venkatesh

Functional materials for MEMS based gas sensors

Functional materials for MEMS based gas sensors

Proefschrift

ter verkrijging van de graad van doctor
aan de Technische Universiteit Delft,
op gezag van de Rector Magnificus Prof.dr.ir. T.H.J.J. van der Hagen,
voorzitter van het College voor Promoties,
in het openbaar te verdedigen op
maandag 21 maart 2022 om 12:30 uur

door

Manjunath RAMACHANDRAPPA VENKATESH

Elektrotechnisch ingenieur,
Technische Universiteit Delft, Nederland,
geboren te Bangalore, India.

Dit proefschrift is goedgekeurd door de promotoren

Samenstelling promotiecommissie bestaat uit:

Rector magnificus,	voorzitter
Prof.dr. G. Q Zhang,	Technische Universiteit Delft, promotor
Dr.ir. A. Bossche,	Technische Universiteit Delft, copromotor
Onafhankelijke leden:	
Prof.dr. Paddy French,	Technische Universiteit Delft
Prof.dr.ir. Jaap M.J.den Toonder,	Technische Universiteit Eindhoven
Prof.dr. Z.W. Liu,	Tsinghua University, China
Prof.dr.ir Willem D. van Driel,	Technische Universiteit Delft
Prof.dr. P.G. Steeneken,	Technische Universiteit Delft
Prof.dr. Lina Sarro,	Technische Universiteit Delft, reservelid

TU Delft Delft University of Technology

Beijing Research Centre

at the Institute of Semiconductors of Chinese Academy of Science

Keywords: Metal Organic Framework, SnO_2 nanoparticles, MEMS gas sensor

An electronic version of this dissertation is available at
`http://repository.tudelft.nl/`.

This thesis is dedicated to my Mother, my late Father and my teachers.

Contents

1

Introduction

1

1.1. More than Moore Roadmap - Sensors

With the development of the first transistor in 1947, the progress of semiconductor industry is mainly driven by Moore's Law. Moore's law published in 1965, states that the number of transistors on a chip doubles every 2 years[1]. The increase in the number of transistors on a chip is relative to the production of smallest feature size transistor using the available semiconductor equipments during the period. In 1971, the feature size of the minimum transistor was 10μm and, in 2018 the feature size currently produced is 7nm. This continuous progress led to miniaturization of the chips and reduction of the cost per chip.

Moore's law further enabled the growth of the semiconductor industry starting from materials, semiconductor devices, instruments to a complete electronic systems for many applications. However, Moore's law mainly focused on increasing the capability of the semiconductor chips for information processing termed as digital content as described in Figure 1.1[1][2]. The devices forming the digital content block are developed with a baseline CMOS technology for CPUs, memory and logic circuits. The non-digital blocks developed with silicon technology include devices for sensing and interacting with the environment, Analog/RF devices for communications, passives and power devices. It is seen that the scaling of More than Moore technology does not follow a similar guideline based on Moore's law due to the diversity of system requirements. This diversity require development of integration concepts such as system-in-package (SiP). In order to increase the functionality per chip for the integration of non-digital content, a new direction was developed in the International Technology Roadmap of Semiconductors (ITRS) known as More than Moore (MtM).

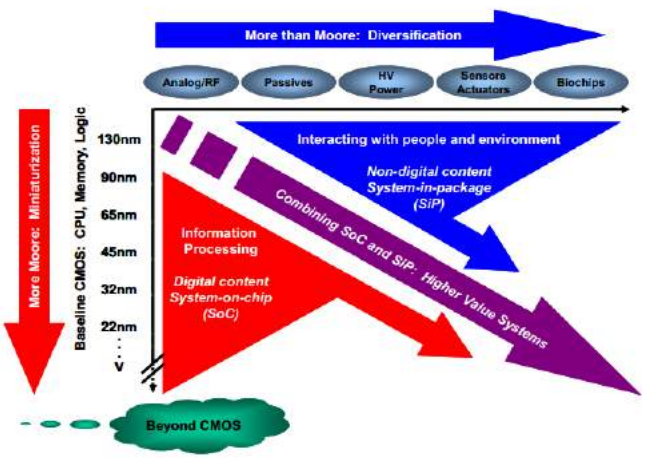

Figure 1.1: International Technology Roadmap for Semiconductors [1][2]

Among the components of the non-digital block, sensors form the most important devices developed in the electronics industry. In a broader perspective, we can classify sensors as natural and artificial man-made devices. Natural sensors are sensors that are present in living organisms. In humans, there are mainly five senses, such as, hearing, vision, taste, smell and touch. When we see an object, the light reflected from the object is captured by the sensory layers of the eyes. The photoreceptors in the retina respond to this light to produce a signal that are transmitted to the optic cortex through the optic nerve. The result of this process is vision[3]. The artificial man-made sensors can be defined as devices that enable interaction with the environment receiving a stimulus, and responds with an electrical signal as output[4]. The stimulii that are received by a sensor may include property, condition or quantity within the environment in which a sensor is placed. Some examples of such stimuli are, light intensity, sound, force, acceleration, infrared radiation, magnetic flux, electric field and chemical composition.

A generic block diagram of a sensor is shown in Figure 1.2. A sensor can be classified as direct sensor and a hybrid sensor. A direct sensor can convert a stimulus into an electrical signal. An example of a direct sensor is a photosensor such as photodiode. Based on the photoeffect, a photodiode generates a current when light falls on the p-n junction. A hybrid sensor require one or more transducers before a direct sensor to convert the stimulus into an electrical signal. Transducers are devices that convert one form of energy into another form of energy. An example of a hybrid sensor is a label-based optical biosensor known as fluorescent-based immunoassays for the detection of biological components in liquids. In this sensor, a label with a bio-recognition element binds to a specific molecule in the liquid sample to generate a fluorescent signal. The fluorescence excitation is achieved by using a laser and the resulting image is captured by a CCD camera to quantify the presence of biological component in the sample. The combination of the two devices makes this device a hybrid biochemical sensor for the detection of biological components in liquids[5].

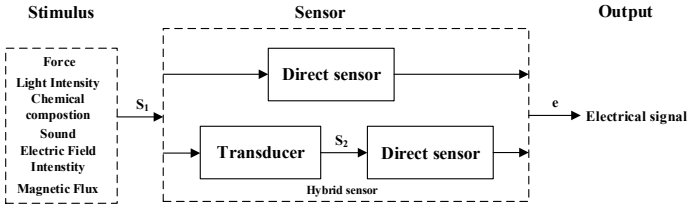

Figure 1.2: Block diagram of a sensor: Direct sensor and Hybrid sensor[4].

Based on the stimulus received at the input of the sensor, they can be classified as physical sensor and chemical sensor. A physical sensor measures physical quantities such as force, temperature or pressure. A chemical sensor

is a device that detects and measures the chemical/biological components, composition or concentration of the analyte in liquid or gas phase. In this thesis, the focus is on one particular type of chemical sensor used to detect and measure the concentration of gases present in the atmosphere or a gas sample in a cell. These types of chemical sensors are called gas sensors. In the next section, an overview and need for gas sensors is discussed.

1.2. Need for Gas Sensors

Air in the atmosphere contains a mixture of several gases. The major components in the air include nitrogen (78.1%), Oxygen (20.9%) and argon (0.9%). The other components in the atmosphere include water vapor, carbon dioxide, and a number of trace gases. Plants and living organism affect the composition of the gases in the atmosphere by the process of respiration. Plants take up carbon dioxide for photosynthesis and release oxygen to the atmosphere. On the other hand, animals during respiration process inhale oxygen for biochemical reactions in the bodies to produce energy and release carbon dioxide in the atmosphere[6].

In living organisms, the olfactory system is the sensor system responsible for the sensation of smell. The olfactory system's main parts consist of the nasal cavity, olfactory epithelium, and olfactory receptors. On average, a person breathes approximately 15 times per minute, which accounts for 500ml of air per breath, which sums to 10,800 liters per day[7]. During the inhalation process, the air is sampled into the nasal cavity due to the relative negative pressure created by the diaphragm in the lungs. The air molecules interact with the sensory cells in the olfactory epithelium called olfactory receptor cells (ORC). The ORCs contain about several hundred olfactory sensory neurons that respond to range of gas molecules in the inhaled air. In humans, the number of olfactory sensory neurons is in the order of 10^6 to 10^8[7]. The signals produced by the interaction of gas molecules with olfactory receptors cells are transmitted to the brain. The olfactory system uses a combination of receptor coding schemes to form a specific pattern for an odor and helps to discriminate among the different odors. Although the biological olfactory system in humans is capable of detecting and distinguishing several hundreds of odors, there are limitations due to the amount of ORCs. In contrast, a canine olfactory system has several hundred times the ORCs found in the human olfactory system that allows the detection of low concentrations of odors and gases in the atmosphere. This is one of the prime reasons that canines are often used in the detection of explosives such as TNT in landmines[7][8]. Thus the human olfactory system has limitation in the detection of extremely low concentrations of many gases in the atmosphere that are harmful to humans resulting in sickness and long term health concerns.

Air pollution can be defined as the introduction of gases higher than the nominal concentration to the environment that are harmful to humans and living organisms[9]. The sources of air pollution are mainly due to large-scale activities of humans such as industrial process plants(metallurgy, crude oil pro-

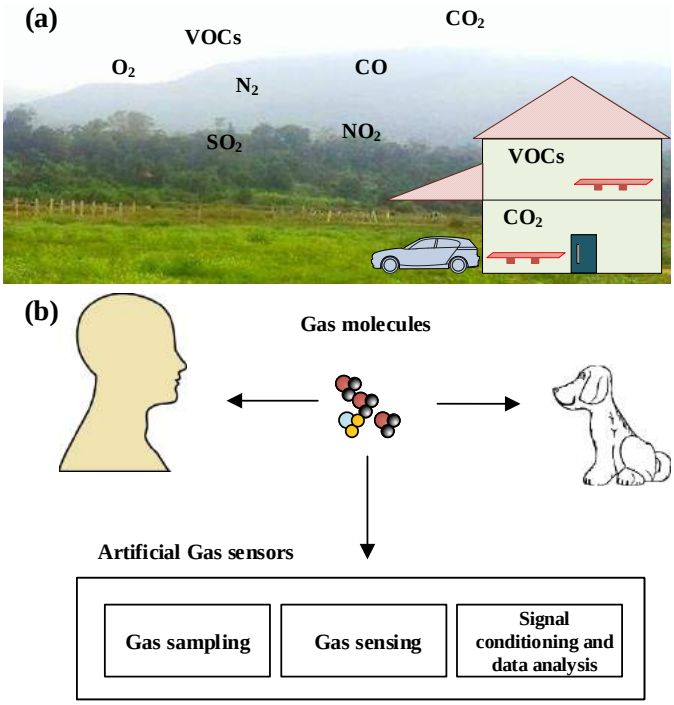

Figure 1.3: (a) Illustration of components of gases found in the atmosphere (Indoor and Outdoor). (b) Illustration to provide comparisons of gas sensing in human, canines and artificial gas sensors

cessing, production of solvents), energy production plants, combustion engines used in gasoline and diesel powered automobiles, landfills used for solid and sewage waste treatments. These activities causes emission of large amounts of gases such as carbon monoxide (CO), carbon dioxide (CO_2), nitrogen dioxide, sulphur dioxide, volatile organic compounds (VOCs) and particulate matter in the atmosphere as illustrated in Figure 1.3a. The presence of such pollutants in large quantities in the ambient air in the environment of humans for long periods can cause various health effects. Several Chronic Obstructive Pulmonary Diseases (COPD) such as coughing, asthma and other respiratory diseases are closely related to short-term exposure to pollutants in air. The long-term health effects due to air pollution include cardiovascular diseases, chronic asthma and perinatal disorders[9].

Among the different pollutants harmful to human health, VOCs are found to be significantly present in the indoor ambient air. VOCs are class of organic chemical compounds that have lower boiling point and exist mainly in the gas phase in ambient temperature and humidity ranges[10]. In indoor

environment, VOCs are known to be emitted by many sources such as building materials, furniture, paints, adhesives, carpets, rubber , vinyl, textiles and many household items. The emitted compounds are mainly hydrocarbons such as benzene, methanol, propanol, ethanol, toluene, acetone, formaldehyde, xylene[10]. Several studies have reported that on average people spend about 80% to 90% of the time indoors mainly at home, offices, transportation, shopping malls, school and other closed spaces inside buildings[10][11]. The amount of time spent indoors is even higher for elderly, children and ill people. Due to the increased time spent indoors people are constantly exposed to more than 500 identified VOCs that are found to cause problems to human health such as headaches, nausea, irritation of nose, eyes and throat[11]. These effects are even more severe for people with allergies and respiratory diseases such as asthma, shortness of breath. The deterioration of the indoor air quality are also associated with sick building syndrome (SBS) such as fatigue, loss in concentration, suffocation and headaches leading to concerns in health at workplaces and living inside buildings [12].

Table 1.1: Threshold Limit Value (TLV) for STEL and LEL of different VOCs identified in the indoor air environment[12][13][14].

Volatile Organic Compound	**STEL (15 mins period) ppm**	**LEL (8-hour period) ppm**	**Sources**
Acetone	1500	500	Textile polish removers
Ethanol	-	1000	Dish washing liquids detergents
Formaldehyde	2	2	Wood, Particle boards Thermal insulation
Methanol	250	200	Paints
Benzene	-	1	Tobacco smoke
Toluene	100	50	Adhesives
Xylene	100	50	Fuel combustion
Ammonia	35	25	Concrete, Self-leveling mortar

The amount of exposure to VOCs identified in the indoor air that are harmful to human health vary based on the nature of VOCs and exposure duration. The duration of exposure to VOCs also known as workplace exposure limit (WEL) are defined by two time periods limits, long-term exposure limit (LEL) - 8 hour period and short term exposure limit (STEL) - 15 minutes period. The thershold limit value (TLV) for the concentration of the VOCs are usually expressed in parts per million (ppm) or mmiligrams per cubi meter ($mg.m^{-3}$) for both STEL and LEL[13]. The TLV for the exposure of certain VOCs such as ketones, alcohols, aldehydes commonly found in the indoor air environment is tabulated in Table 1.1. As an example, constant long term exposure to methanol, ethanol found in house items such as paints, wallpaper, detergents deteriorate the indoor air environment. Long-term exposure to methanol above a value of 200ppm can lead to health effects for people such as nausea, vomiting, and affects the nervous system[15]. Hence, it becomes increasingly necessary to have gas sensors to monitor the indoor air quality frequently to create awareness of the exposure level VOCs. As discussed in

the earlier part of this section, human olfactory system have limitation for the detection of gases and VOCs present in the atmospheric air. Thus, there is a need for an artificial gas sensor system. A machine olfactory system or an artificial gas sensor system also corresponds to the structure of human olfactory system. The main units are a gas handling unit, sensor unit, a signal processing and data analysis unit to monitor the concentration of levels of gas analytes in the atmosphere air as illustrated in Figure1.3b. In the next section, the various technologies that are used for the development of artificial gas sensors are discussed.

1.3. Technologies for gas sensors

Gas sensing achieved by different technologies are mainly categorised based on the type of stimulus received at the input of the sensor for converting the concentration of gaseous analyte to an electrical signal. The different stimuli for gas sensing are, thermal, mechanical, optical, electrochemical or electronic as described in the schematic in Figure 1.4.

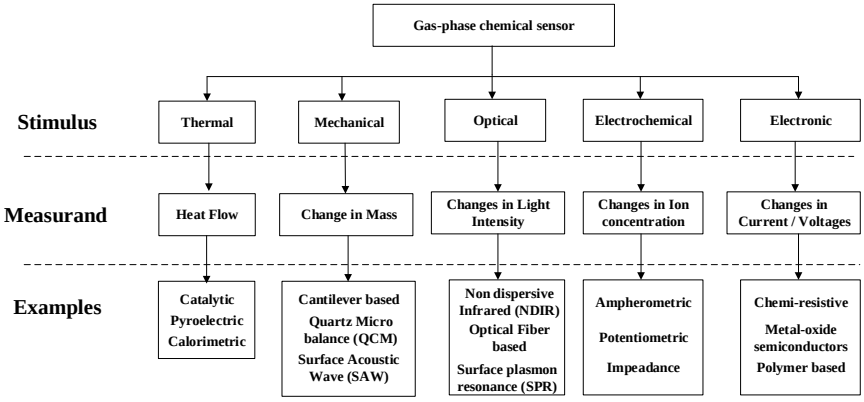

Figure 1.4: Overview of different types gas sensor technologies

The characteristics of gas sensors are defined by sensitivity, selectivity, detection limit, response time and stability. *Sensitivity* of a gas sensor is defined as the ability of the sensor to detect specific gaseous analyte within the range of concentration. *Selectivity* is defined as the ability of the gas sensor to distinguish the gaseous analyte withing the range of concentration in the presence of different gaseous analyte that can also produce sensor responses. The *detection limit* or the *limit of detection(LOD)* of a gas sensor is the minimum concentration of the gaseous analyte that can be reliably detected by the sensor. *Response time* of a gas sensor is the time taken for the sensor output signal to reach 90% of a stable value after the detection of gaseous analyte within the range of interest. Finally, *Stability* of a gas sensor refers to the period of time in which the sensor baseline and response are reliable within

specifications[16].

Based on the applications that include indoor/outdoor pollution monitoring or industrial environment monitoring, certain gas sensors technologies are preferred over others. For indoor air pollution monitoring, which is the main focus of this thesis, the important criteria for the artificial gas sensor system include, portability, real-time detection and low cost of manufacturing. In this section, the sensing principle, measurement methodologies, advantages and challenges for the different types of gas sensor that are suitable for indoor air pollution monitoring is discussed.

1.3.1. Electrochemical gas sensor

An electrochemical gas sensor consists of an electrochemical cell in a two-electrode or a three-electrode configuration housed in a cell consisting of an solid or liquid ion conductive electrolyte. In a two-electrode system, the two electrodes are namely working electrode and reference electrode. A three-electrode system consists of a working electrode, reference electrode and a counter electrode. A schematic of a three-electrode electrochemical gas sensor is shown in Figure 1.5. In this configuration, a voltage is applied between the reference electrode and the working electrode. The detection and quantification of gaseous analytes in an electrochemical gas sensor is a combination of two mechanisms namely, electrochemical recognition and electrochemical transduction. In the electrochemical recognition mechanism, an electrochemical reaction occurs at the surface of the working electrode by reduction or oxidation reaction based on the properties of the gaseous analytes. This electrochemical reaction is converted to an electrical output signal by electrochemical transduction mechanism to quantify the concentration of the gaseous analyte. The electrical output signal is obtained mainly by potentiometric and ampherometric measurements[16].

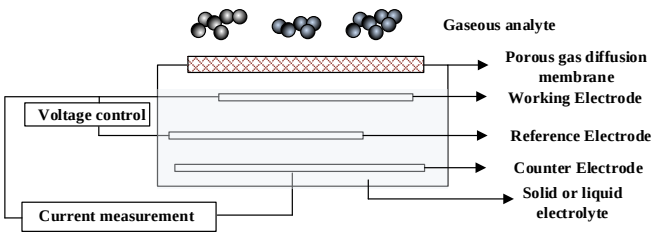

Figure 1.5: Schematic of a three electrode electrochemical gas sensor

In a potential based electrochemical sensor, an electric current is produced at the surface of the working and reference electrode due to the electrochemical reaction on exposure to gaseous analytes. The measured electrochemical potential for the sensor is defined by the Nernst equation given by[16],

$$E = E_0 - (\frac{RT}{nF})ln(\frac{C_{measured}}{C_{reference}}) \tag{1.1}$$

where, E is the electrochemical potential measured in the electrochemical cell on exposure to gas analytes, E_0 is the reference electrochemcial potential, R is the gas constant, F is the faraday constant, n is the moles of electron, T is the absolute temperature in Kelvin, $C_{measured}$ is the concentration of gas analyte measured, $C_{reference}$ is the concentration of gas analyte measured at known reference compositions. From this equation, it can be seen that there is a linear relation between the measured electrochemical potential and ln ($C_{measured}/C_{reference}$). Based on a calibrated known value of $C_{reference}$, the concentration of the analyte can be obtained by the linear relation between E and ln ($C_{measured}$) with the slope of (RT/nF).

In an amperometric based electrochemical sensor, an electrochemical potential with respect to the reference or counter electrode is applied to the working electrode. On exposure to gaseous analytes, an electrochemical reaction occurs at the surface of the working electrode to produce a limited current between the working electrode and the counter electrode. The measured current is directly proportional to the molar concentration of the gaseous analyte given by[17],

$$I_l = KC_{measured} \tag{1.2}$$

where, I_l is the limited current measured, $C_{measured}$ is the concentration of gas analyte and K is the proportionality constant.

Electrochemical gas sensors are one of the oldest developed gas sensors. Some examples of electrochemical gas sensors are Type I oxygen sensor that uses solid electrolyte yttria stabilized zirconia (YSZ), K_2CO_3 electrolyte for carbon-di-oxide and antimonic acid for hydrogen gas sensing [16][18]. The advantages of electrochemical sensors include, linear relation between concentration to the measured output, good resolution and good repeatability. The electrochemical gas sensors are usually calibrated to a known concentration of the target gas before they are used in on-field operation. However, they have limited shelf life due to aging of the electrolyte, limited selectivity and difficulty in miniaturising the electrochemical sensor for portable devices.

1.3.2. Optical gas sensors

Gas molecules can absorb radiation according to their quantized vibrating energy with the degree absorption being proportional to the gas concentration[11]. Based on this principle, the different types of gas sensor with optical spectroscopy include, Non-dispersive gas sensors (NDIR), surface plasmon resonance (SPR) gas sensor and Optical fiber based gas sensor.

NDIR sensors are the commonly available commercial sensors for the detection of CO_2 and hydrocarbons. In NDIR sensor, the detection is based on the absorption of infrared light by gaseous analytes. A schematic of a NDIR sensor is shown in Figure 1.6. The sensor consists of an infrared light source, a

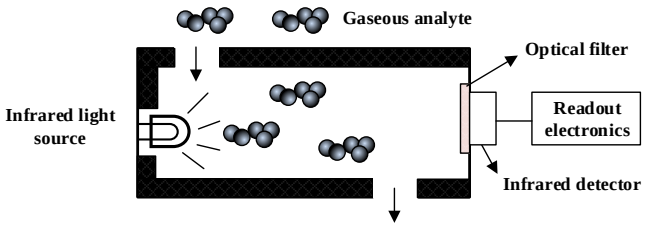

Figure 1.6: Schematic of a NDIR sensor gas sensor

gas cell having a path length of L and an infrared detector. According to Beer-Lamberts law, the measured output light intensity by the infrared detector is given by[17],

$$I(t) = I_0(t)e^{-\alpha(\Lambda)LC} \tag{1.3}$$

where, *I(t)* is the output light intensity, $I_0(t)$ is the input light intensity, α is the absorption coefficient, L is the optical path and C is the concentration of the gaseous analyte in the gas cell. The reduction in the measured output light intensity is proportional to the concentration of gas in the chamber.

Optical gas sensors have fast response time, good stability and operational in the absence of oxygen. However, they have moderate selectivity due to interference with water vapor, complex readout electronics and difficulty in miniaturization[11].

1.3.3. Mechanical gas sensors

Mechanical gas sensors are based on the principle of changes in the mass by interaction with gaseous analytes detected by transducers. Mass sensitive transducers mainly contain a resonator or surface acoustic devices with gas sensing layer deposited on the surface of the devices. In these devices, target gaseous analytes interact with the sensing film on the surface of the resonator to produce a shift in the resonant frequency or cause damping or change in the wave velocity of the devices. Gas sensing using quartz crystal microbalance(QCM), surface acoustic wave(SAW) and micro-cantilever based devices are some of the examples of mechanical gas sensors.

A schematic of the operation of a quartz crystal microbalance device for gas sensing application is shown in Figure 1.7a It consists of a quartz crystal, a piezoelectric material placed between two electrodes, with a gas sensing film deposited on the surface of the top electrode. The applied electric potential causes a tangential deformation at the top and bottom surface of the quartz crystal in a way that they oscillate. At a particular frequency, the disk will be in resonance. The device is exposed to gaseous analyte, specific gas molecules bind to the surface, increasing the mass of the device causing a shift in the resonant frequency which is calculated using Sauerbrey's equation given by[16],

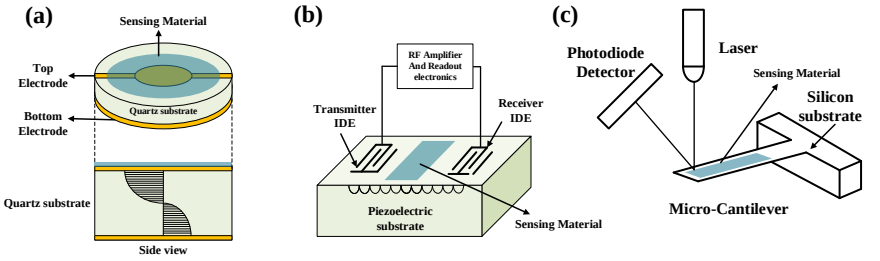

Figure 1.7: (a) Schematic of a Quartz microbalance gas sensor. (b) Schematic and measurement setup of a Surface Acoustic Wave (SAW) gas sensor. (c) Schematic and measurement setup of Micro-cantilever based gas sensor.

$$\Delta f = -\frac{2f_0^2}{A\sqrt{\rho\mu}}\Delta m \tag{1.4}$$

where, Δf is the change in frequency due to the mass change Δm by absorption of gas molecules, f_0 is the resonant frequency of the QCM, ρ is the density of the piezoelectric material, μ is the shear modulus and A is the proportionality constant based on the mechanical and electrical characteristics of the QCM. QCM devices have relatively low cost in manufacturing, faster response time and good sensitivity. They have limited selectivity that is determined by the sensing properties of the coating layers and lower sensitivity.

Surface Acoustic Wave(SAW) devices consists of an array of two sets of aluminum, gold or platinum interdigitated electrodes (IDE)s fabricated on a bulk piezoelectric substrate as shown in Figure 1.7b. The two IDEs are separated by a gap that is coated with a thin film of gas sensing material. In these devices, one set of the IDE array acts as a transmitter that generates a surface acoustic wave which propagates along the surface of the device. During sensing operation, the gaseous analyte is adsorbed onto the sensing film that can cause changes in the mass of the film. This causes changes in the propagation of the acoustic wave in the device. The receiver IDE array receives this modified acoustic wave signal and the changes in the amplitude and phase of the acoustic wave is measured. These variations measured are proportional to the amount of gas adsorbed on the film[19]. SAW devices fabricated using semiconductor photolithography tools can have lower cost of manufacturing and can be miniaturised. However, these type of gas sensors have strong dependency on the environment as the acoustic waves can be distorted due to changes in the temperature, pressure and humidity. SAW sensors also require complex readout electronics that needs to be carefully designed to have good signal to noise ratio.

A micro-cantilever is a device that consists of thin free standing beam anchored to a bulk substrate. Micro-cantilever are used as sensing platforms for chemical (gas and liquid)and biological applications[20]. A schematic of a

micro-cantilever based gas sensor device is shown in Figure 1.7c. The surface of the free standing area of the micro-cantilever is coated by sensing material for gaseous detection. Upon electrical excitation the resonant frequency of the micro-cantilever is measured using a laser and a optical detector. During exposure to gaseous analytes, the adsorbed gas molecules on the sensing layer changes the mass of the surface of the cantilever, resulting in the change in the resonant frequency of the cantilever. The change in resonant frequency is given by,

$$\Delta f = \frac{f_r}{2f_n}\Delta m \tag{1.5}$$

where, Δf is the change in frequency due to the change in mass Δm , f_r is the resonant frequency of the cantilever and m_e is the effective mass of the cantilever.

Some of the advantages of mechanical gas sensors include sensitivity to the changes in mass adsorbed by the sensing materials and ability of miniaturising the transducers. However, due to suspended elements in the transducers, difficulty in packaging the devices and complex readout electronics requirement hinder applications in portable equipments.

1.3.4. Thermal gas sensor

Pellistor based gas sensor are a type of thermal gas sensor used in the detection of flammable gases such as benzene, methane[11]. This sensor consists of two platinum coils that are coated with ceramic beads or pellets. One coil consists of an active pellet that is activated with catalyst such as platinum or palladium. The second coil consists of an inactive pellet that does not contain any catalyst but serves as a compensating element in the detection. These coils are placed on the elements of a Wheatstone bridge configuration. The function of the platinum coils is to heat the pellets and also serve as a resistance based thermal sensor.

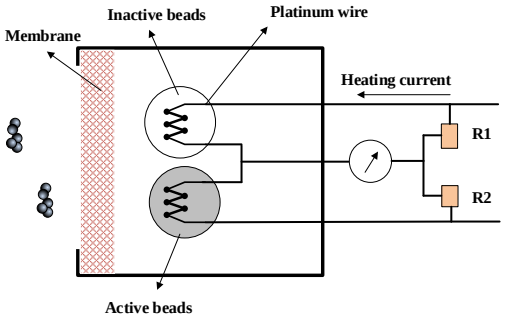

Figure 1.8: Schematic of a pellistor based thermal gas sensor.

A schematic of a pellistor gas sensor is shown in Figure 1.8. The coils are heated to about 300°C to 500°C by supplying a current. As flammable gaseous

analytes above a certain threshold diffuse into the sensor package through the membrane and come in contact with the pellistor element, the reaction at the catalytic surface of the pellet increases the temperature in the coil, which in turn increases the resistance of the coil. Due to this temperature change, the output signal obtained from the bridge is proportional to the heat of reaction caused due to the presence of the gaseous analyte[21]. The pellistor based sensors are simple to manufacture and can detect flammable gases with high sensitivity. However, presence of oxygen is a requirement for operation of pellistor sensors. The pellets can be poisoned by lead, sulphur or chlorine[21].

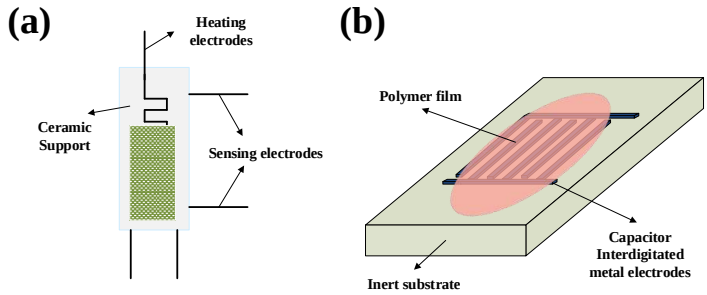

Figure 1.9: Schematic illustration of (a) Metal-oxide chemi-resistive gas sensor. (b) Polymer based chemi-capacitive gas sensor

1.3.5. Chemi-resistive and Chemi-capacitive gas sensors

Thin film materials that undergo changes in its electrical property by the adsorption or chemisorption of gaseous analytes are classified into resistive-based and capacitive-based gas sensing materials. By using suitable transducers such as resistor or capacitor transducers, the concentration of gaseous analytes can be converted into an electrical signal. These type of gas sensors are classified as chemi-resistive and chemi-capacitive gas sensors.

In a chemi-resistive gas sensor, n-type or p-type semiconducting metal-oxides(MOX) are mainly used as the sensing layer and deposited on electrodes made of platinum or gold. A schematic of a commercial chemi-resistive gas sensor is shown in Figure 1.9a. The metal-oxides are heated to a temperature of 400°C using platinum or tungsten heaters. At these temperatures, oxygen in the atmosphere are chemisorbed on the surface of the sensing layer. A depletion region is formed at the surface of the semiconducting metal oxide also known as active sites. Upon exposure to reducing or oxidising gases, adsorption and reaction between the gases with the active sites lead to an increase or decrease of the resistivity of the metal oxide layer[11]. Metal oxide gas sensors are portable, have high sensitivity and low-cost of development. However, MOX based gas sensor have low selectivity and require high power in the range of mW to W for operating the heating element.

A schematic of a basic chemi-capacitive gas sensor is shown in Figure 1.9a. The capacitive transducer platform consists of parallel comb metal electrodes having a fixed gap patterned on silicon or ceramic substrates. This configuration of electrodes are known as interdigitated electrodes(IDEs). A thin film of dielectric material that can adsorb target gas molecules are deposited or grown on the IDEs. The adsorption of target gas molecules changes the effective dielectric constant within the sensing film leading to changes in the capacitance measured as a function of vapor concentration. Chemi-capacitor gas sensors have the ability to detect gaseous analytes at room temperature, have low-power consumption and simple fabrication methodology. However, polymer films have disadvantages such as cross-sensitivity to water vapor, lower long term stability and reversibility[22].

Table 1.2: Comparison of gas sensor technologies[11][23][24].

Sensor Technology	**Advantages**	**Limitations**
Electrochemical	Short response time Detect wide range of gases Long term stability	Aging of the electrolyte Difficulty in miniaturisation Require frequent calibration
Optical	Short response time Operation under absence of oxygen Long term stability	Complex readout electronics Difficulty in miniaturisation Lower selectivity to Moisture
Mechanical	High Sensitivity Fast response time Can be miniaturised	Low selectivity Complex readout electronics Reliability issues
Thermal	High sensitivity Selective to flammable gases Simple manufacturing process	High power consumption Require oxygen environment Deterioration of the pellets
Metal-Oxide	High sensitivity Simple readout circuitry Low cost Can be miniaturised	Low selectivity High power consumption
Capacitive gas sensor	Room temperature operation Low power consumption Can be Miniaturised	Cross-sensitivity to humidity Lower long-term stability

1.3.6. Comparisons of various types of gas sensors

In the previous section, the detection of gaseous analytes using various technologies was presented. The sensing response and characteristics of the gas sensors among the different technology platforms are dependent on the ambient environment operating conditions, varying read-out electronics and cost

of development of the sensors[18]. In Table 1.2, a comparison of various type of gas sensors technologies detailing advantages and limitations is presented. Electrochemical sensors and optical sensors are used in most commercial gas sensing system for monitoring gas concentration levels in urban cities, industrial and home environment. However, the limitation of these commercial sensors are in the development of miniaturised gas sensor modules in devices such as mobile phones, wearable and IoT devices. One of the requirement of sensors in mobile and wearable devices are the form factor of the sensors combined with packaging need to have dimensions of less than 5mm-10mm in thickness. Furthermore, the power consumption need to be within ranges of μW to few mW during operation. Although, micro-cantilever based gas sensing devices can be miniaturised, the reliability of mechanical components during packaging and operation can be a limiting factor for long-term. Metal-oxide based chemi-resistive and polymer based chemi-capacitive sensors are prime candidates for the development of miniaturised sensors due to the ease of transducer fabrication, low cost and ability to integrate read-out electronics within the package in a miniaturised form factor. Moreover, resistive and capacitor transducers developed using silicon technology enable fabrication of sensor arrays and on-chip signal processing with CMOS analog circuits. In the next section, the development of silicon MEMS gas sensing devices is discussed.

1.4. Silicon MEMS gas sensor

Micro-electromechanical systems (MEMS) consists of electrical and mechanical components manufactured in the micro-scale to nano-scale dimensions. MEMS technology is used in the development of sensors and transducers. MEMS technology adopts the manufacturing process used in the CMOS semiconductor industry, such as lithography, metal deposition, metal/substrate etching, and packaging tools. The development of MEMS devices using silicon substrate enabled the production of commercial MEMS based sensors that include microphones, accelerometers, gyroscopes, pressure sensors and chemical/biosensors[25]. Some of the driving technologies for MEMS sensors include development and integration of sensors in portable, wearable and battery powered systems. Wearable sensors and on-body sensors have gained considerable interest due to their promise for real-time monitoring of the wearer's health and fitness, exposure levels of air quality or water quality in various applications, such as sports, patient care, assisted living, and others. Environment sensing and bio-sensing wearables drive the next generation of wearable technologies that allow continuous monitoring in a wide range of form factors. Such wearable devices require minimization of electronics, cost-effective packaging, and increased reliability to achieve more functionality ("More than Moore") in a single miniaturized package. A portable real-time air quality monitoring system provides valuable information on air pollution levels around us. One of the most critical requirement for mobile or wearable gas sensor systems are to operate with lower power consumption in a miniaturized form factor. In Figure 1.10, an illustration of integration of MEMS gas sensors in various portable de-

vices and wearable devices such as mobile phones, smart watches, face masks and earphones is described. Solid-state gas sensors developed using MEMS technology offer various benefits such as miniaturization, compatibility with CMOS technology, and mass manufacturing capability. In the previous sections, we have seen that there are many technologies that can be employed for gas detection for both portable and mobile system. However, miniaturisation of gas sensors to achieve integration in devices such as mobile phones, wearables and earphones can be achieved by development of sensors using MEMS technology.

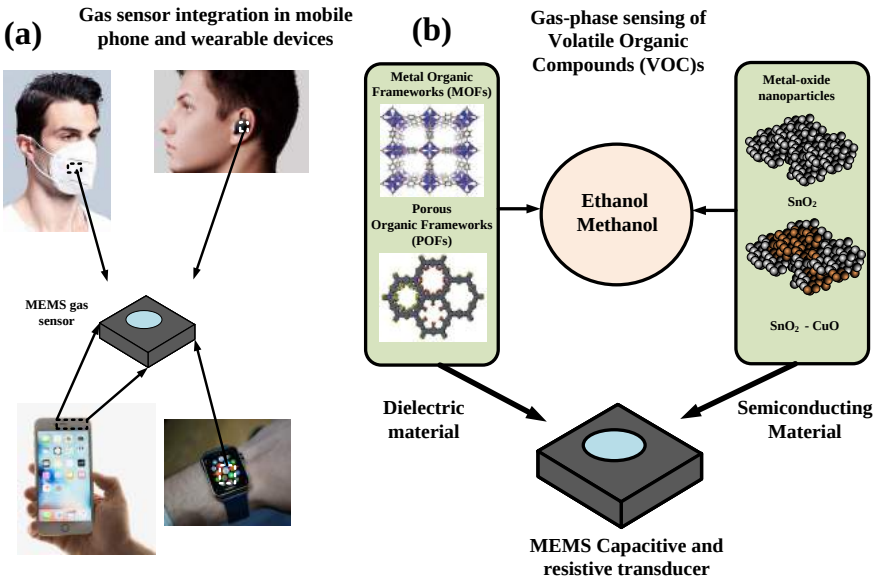

Figure 1.10: (a) Illustration of the devices for miniaturised MEMS gas sensors[26][27][28][29]. (b) Illustration of a MEMS gas sensor with different materials

In Figure 1.11, the methodology utilised in the development of a silicon MEMS gas sensor is illustrated. The three main steps include, functional material development, MEMS device development and integration of the functional material and gas sensing measurements. In the next section a brief explanation of the three steps are discussed.

1.5. Functional Material Development

In this thesis, the functional materials investigated for the detection of volatile organic compounds such as methanol and ethanol are listed below,

1. Thin film dielectric materials

   (a) Metal Organic Framework (MOF) namely, CuBTC and ZIF-8 MOF.

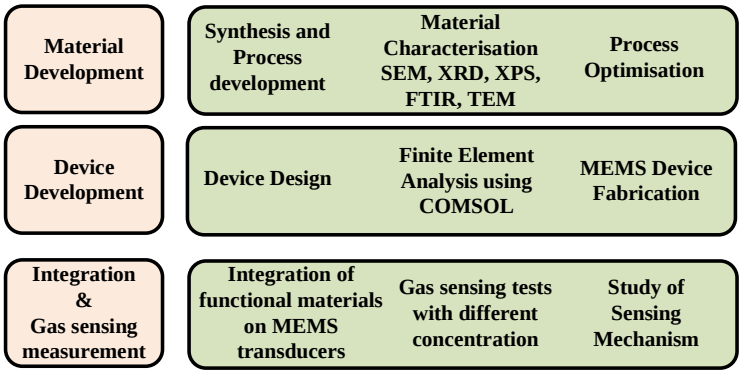

Figure 1.11: Systematic methodology in the development of silicon MEMS gas sensors.

(b) Porous Organic Framework (POF).

2. Thin film metal oxide materials

   (a) SnO_2 nanoparticle film.

1.5.1. Thin Film Metal Organic Framework and Porous Organic Framework

Metal organic frameworks (MOFs) are a new class of nanoporous materials with applications in the field of catalysis, gas sensing, gas storage and separation. MOFs have highly ordered structure, high porosity and large surface areas. MOFs are formed when metal ions or cluster of ions known as centers are linked together with organic connectors known as ligands. These ions and linkers form a highly regular structure or framework that are chemically stable. The modular process of forming diverse structures with MOFs enable forming tunable pore sizes and modification of the properties of the internal surface[30]. MOFs can be synthesised by several methods that follow conventional solution based chemical synthesis methods. The various methods for the synthesis of MOFs are solvothermal method, electrochemical synthesis, microwave assisted synthesis method, mechanochemical and sonochemical synthesis method. The different synthesis method have an impact on the structure and properties of MOFs such as crystal size, morphology, pore size and surface area[31]. In this thesis, the synthesis, characterisation and application of thin film MOFs as functional materials towards sensing methanol and ethanol vapors is discussed.

MOFs have shown superior sorption properties in comparison to zeolites and activated carbon for carbon-dioxide and hydrogen gas storage applications. The molecules of hydrogen are adsorbed within the framework of MOFs without being covalently bounded at low partial pressure, enabling release of hydrogen molecules from the framework completely[32]. The reversible adsorption and desorption of gaseous analytes behaviour in MOFs are an added

advantage for utilising MOFs as functional materials for gas sensing applications. Furthermore, the large surface area of MOFs enable adsorption of specific gaseous analytes within the porous framework of the MOFs thereby enhancing the sensitivity and reversible interaction with gaseous analytes. The modification of the physical and chemical properties of MOFs can further improve the selectivity by exclusion of gas molecules based on the pore size and affinity of the gas molecules with the MOF framework[33]. MOFs being inherently non-conductive materials, the adsorption and desorption of gas molecules within the surface of the MOF causes a change in the effective dielectric constant causing changes in the impedance of the MOF. These changes in the impedance can be measured as a function of concentration to enable detection of the amount of gaseous analytes adsorbed in MOF[32][33]. A list of metal-organic framework used for the detection of volatile organic compounds are tabulated in Table 1.3.

Table 1.3: Metal Organic Framework as sensing material for VOC gas sensing in literature.

Sensing Material and Reference	**Transducer**	**VOC detected**	**Concentration range (ppm)**
CuBTC-MOF[34]	Optical(SPR)	Acetone, Ethanol	290,230
ZIF-8[35]	Optical fiber	Ethanol	100-700
CuBTC(MOF-199)[36]	Capacitive	Ethanol,Methanol	250-2000
$Cu_3(BTC)_2$ [37]	micro-cantilever	Toulene	100-1000
HKUST-1[38]	micro-cantilever	Methanol,Acetone	13000,27000

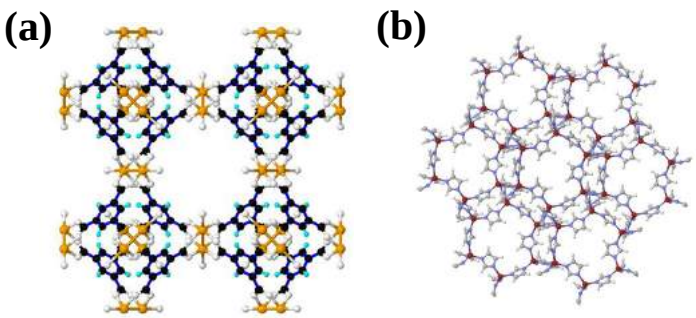

Figure 1.12: Illustration of crystal structure (a) CuBTC MOF, Cu, O, C and H are represented as orange, white, black and cyan respectively. (b) ZIF-8 MOF with Zn, N, C and H described by red, purple, grey and white spheres, respectively[39].

As seen from the tabulated results, MOF thin film coated on devices such as optical fiber, micro cantilever and capacitive transducers have shown the ability to adsorb VOC gases. In this thesis, two type of MOFs namely CuBTC and ZIF-8 MOF coated on capacitive transducers are investigated for the detection of volatile organic compounds such as methanol and ethanol. An illustration of crystal structure of CuBTC MOF material is shown in Figure

1.12a. In this MOF, the metal ion is Copper (Cu^{2+}) and the organic linker is benzene tri-carboxylate molecule. The copper ion reacts with benzene group to form paddle wheel structure in a cubic lattice with porous centres. The Cu paddle wheel framework are formed from two Cu ions coordinated with four tridentate benzene-1,3,5-tricarboxylate (BTC) ligands. CuBTC has affinity for small-size gases such as NH_3, CO, NO_2, NO, H_2S, and volatile organic compounds (VOCs) such as methanol and ethanol. Thus, CuBTC MOF is seen as a potential candidate for application as affinity layer on capacitor IDEs for the detection of volatile organic compounds[36]. Zeolitic imidazolate frameworks (ZIFs) are another class of MOFs that contain metal ions such as Zn or Co with imidazolate organic linkers. ZIF-8 MOF belong are one type of ZIFs that have high surface areas, high porosity and high thermal stability. The illustration of the crystal structure of ZIF-8 MOF is shown in Figure 1.12b.

Porous organic framework(POFs) are one type of micro-porous polymers derived from organic precursors being covalently bonded[40]. POFs have high surface areas and large porosity that are very advantageous for gas sensing applications. POFs can be synthesised with solution based method that allow a simple fabrication process and coating on transducers[41]. Melamine based POFs functionalised with platinum(Pt) nanoparticles coated on silicon-nanowires was used for the detection of methanol[40]. In this thesis, melamine based POFs as functional materials are coated on capacitor transducer devices to study the interaction with ethanol and methanol.

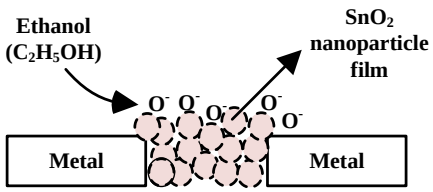

Figure 1.13: Schematic illustration of sensing mechanism of ethanol in SnO_2 nanoparticle.

1.5.2. Thin film SnO_2 nanoparticles

SnO_2 is an n-type semiconductor oxide having a wide band gap (3.6eV). At elevated temperatures above 150°C, oxygen molecules are chemisorbed in the form of O^- and O^{2-} by accepting electrons from SnO_2. A space charge region is formed at the surface of the SnO_2, also referred to as active sites. Upon exposure to reducing gases, adsorption and reaction between the gases lead to the formation of free electrons as reaction products. This results in the reduction in the thickness of the space charge region, thereby increasing the conductivity of SnO_2. The ratio of the change in conductance upon exposure

to the reducing gas and the baseline conductance in dry air determines the sensitivity of the sensor[42–45]. The reversible interactions at the surface of SnO_2 film, and high thermal stability are some of the benefits of SnO_2 utilised as a material for gas sensing applications[45]. The sensing mechanisms in SnO_2 and most metal-oxide materials are determined by the number of sites available at the surface of the material for the chemisorption of oxygen and gas molecules.

1.6. MEMS Device Development

The development cycle of the MEMS devices follow similar approach to CMOS device development cycle. The steps include modelling and simulation of MEMS device by finite element method(FEM), layout design specific to the available fabrication process, device fabrication, packaging and room temperature device characterisation to select obtain good dies for characterisation. In this thesis, the requirement is to develop the capacitive interdigitated electrode (IDE) and microhotplate devices using silicon MEMS micro-fabrication technology for chemi-resistive and chemi-capacitive gas sensors.

1.6.1. Device design and fabrication

The capacitance of a parallel plate capacitor is given by the following relation,

$$C = \epsilon_o \epsilon_r \frac{A}{d} \tag{1.6}$$

where ϵ_o is the permittivity of free space, ϵ_r is the permittivity of the material between the parallel plate, A is the area of the capacitor and d is the distance between the parallel plates. The development of a parallel plate capacitor in planar silicon MEMS technology process would need the dielectric material to be sandwiched between two metal electrodes. This would increase the complexity in device fabrication and special techniques to deposit metal over the dielectric without shorting the two metal electrodes. Capacitors made of interdigitated electrodes in alternate finger capacitor allows planar finger electrodes on silicon. A cross-sectional view of IDE capacitor coated with a thin film dielectric material is shown in Figure 1.14a. The capacitance that can be measured between the electrodes will be dependent on the dielectric material, substrate material and the parasitic capacitances.

A silicon MEMS microhotplate(MHP) based metal oxide sensors consists of a silicon substrate, a thin dielectric membrane, typically thermal oxide or silicon nitride on which a metal resistor of platinum, molybdenum, or titanium nitride are patterned to form the heater layer, a passivisation layer that serves as an insulating layer between the heater and the sensing electrodes and the sensing material. The sensing material is deposited across the sensing electrodes, typically made with platinum(Pt) or gold(Au) to establish good electrical contact between the sensing material and the electrodes. A schematic illustration of a microhotplate with sensing film deposited on the sensing electrodes is shown in Figure 1.14b.

In a microhotplate device, the electrical power supplied to the resistor is converted to thermal energy by joule heating mechanism. The heat generated in the microhotplate is dissipated to the surroundings by three heat transfer process that includes, conduction from the microhotplate device area to the substrate, convection from the microhotplate device area to the air and radiation to the environment. The heat loss due to conduction and convection mechanism are the dominant losses in the microhotplate devices[46]. The heat loss due to conduction from the microhotplate area to the substrate can be minimised by fabricating the microhotplate on a closed membrane or suspended membrane type structures. In a closed membrane structure, the bulk silicon at the backside of the microhotplate device area is etched by anisotropic etching. In a suspended membrane structure, the microhotplate active area is suspended with the support of beams to the substrate by etching the bulk silicon at the front and backside of the device. Although a closed membrane structure can offer better mechanical stability for high-temperature operation, microhotplates fabricated on a suspended membrane structure have lower thermal mass, thereby reducing the device power consumption. The mechanical stability of the suspended membrane structure can be improved by fabricating microhotplates on a low-stress dielectric membrane material. Along with reducing the device power consumption, the temperature uniformity across the microhotplate active area needs to be considered. The temperature uniformity can be improved by optimising various designs of the heater geometry such as, meander, double spiral, or drive wheel using the finite element method (FEM) multiphysics software modules from COMSOL, ANSYS. Another method to improve the temperature uniformity is by having a layer of high thermal conductivity material like silicon as a heat-spreader layer below the microhotplate active area[46][47]. Thus, consideration of material, process parameters and geometry of the microhotplate enable efficient design and fabrication of microhotplate based devices for gas sensing applications.

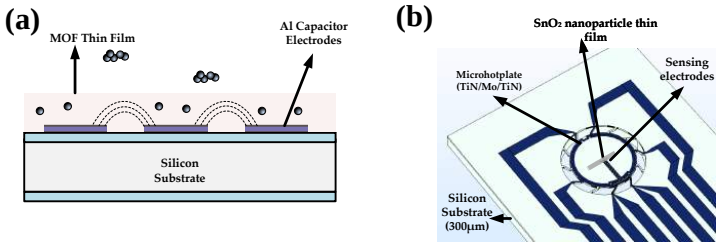

Figure 1.14: Schematic illustration of (a) MOF based chemi-capacitive gas sensor. (b) MEMS chemi-resistive gas sensor

1.7. Integration and testing

1.7.1. Integration of functional materials

The integration of MOFs on optical transducers were done by using the material as a bulk powder and monitoring the change of luminescence properties upon analyte binding[48][49]. MOFs deposited on resistive or capacitive transducer to investigate the interactions with analytes and measure the changes of conductivity or dielectric properties have been reported in several studies[32, 50, 51]. The layer-by-layer deposition method has also been used to make thin films of MOFs on the transducer surface[52–54]. In this thesis, two approaches for synthesis and deposition of MOF/POF is investigated. The direct growth of CuBTC MOF are done by electrochemical synthesis method on interdigitated Cu electrodes and the interaction with analytes such as methanol and water vapors at room temperature are studied. The synthesis of ZIF-8 MOF and melamine based POF is done by solution based methodology and coated by drop-casting on the transducers.

SnO_2 nanoparticles can be synthesized by different methods by several methods such as sol-gel process, hydro thermal, mechanical grinding, flame spray pyrolysis, laser ablation and spark discharge[55]. Among these methods, vapor-phase based synthesis of SnO_2 nanoparticles has advantages such as reduced contamination of the nanoparticles due to impurities, utilising non-toxic organic solvents, reduced waste generation, continuous and flexible processing of nanoparticles than batch-wise process[55][56]. In this thesis, SnO_2 nanoparticles synthesised by spark discharge method deposited on MEMS microhotplate devices are used to study the sensing response towards ethanol.

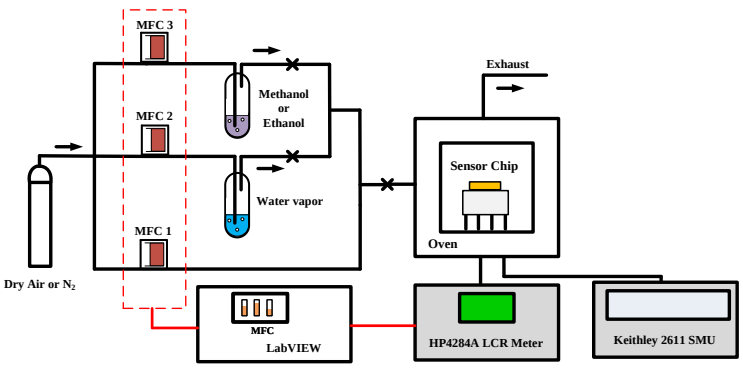

Figure 1.15: Schematic illustration of the gas sensing setup.

1.7.2. Gas sensing measurements

The sensing experiments of the device coated with functional materials for vapors of ethanol, methanol and water are done in a custom-built gas setup schematically illustrated in Figure 1.15. In this system, dry nitrogen or dry air was passed through two bubblers containing ethanol, methanol or water vapor

(MFC 2, MFC 3) to generate saturated stream of the vapors. The saturated concentration of the analyte was calculated using the Antoine equation[57][58],

$$LogP = A - \frac{B}{T + C} \tag{1.7}$$

Where, P is the saturated vapor pressure of the analyte and T is the temperature of the bubbler. A, B and C are the analyte-dependent constants. The vapors were diluted with a parallel stream of dry nitrogen and passed to the gas chamber. A LabVIEW software application was used for controlling the mass flow controllers (MFCs). The capacitance of the sensor devices are measured using a HP4284A LCR meter. The resistance of the devices are measured using a DC source measurement unit (SMU) such as Keithley 2611B.

1.8. Thesis Outline

The thesis is focused on an interdisciplinary study that involves the development of resistive and capacitive transducers by micro fabrication technology and process development of functional materials for gas sensing applications. The chapters of the thesis is summarised pictorially in Figure 1.16 and the details are mentioned in the following paragraphs,

- In Chapter 2, the electrochemical growth of Cu-MOFs on interdigitated Cu electrodes and its ability to detect methanol and water vapors at room temperature is studied. Methanol is mainly used as the analyte to study the feasibility of this MOF-transducer integration technique due to their known affinity toward CuBTC. The interdigitated electrode (IDE) structure allows capacitive detection of the affinity process.
- In Chapter 3, a low-power MEMS microhotplate with IDE capacitor coated with thin film ZIF-8 MOF for the detection of methanol is studied. The device design, fabrication and experimental set up is first discussed. The thermal characterization of bare devices and devices coated with ZIF-8 MOF is presented. The temperature-dependent sensing response of ZIF-8 MOF-coated devices towards methanol, and water vapor is presented. The modeling of temperature-dependent adsorption and desorption kinetic coefficients of methanol in ZIF-8 MOF is discussed.
- In Chapter 4, we have synthesized melamine based porous organic framework(POF) by schiff based chemistry. Thin film of POFs are coated on capacitor transducers and its sensing response to methanol and ethanol is investigated. The design and fabrication of the IDE capacitor device used in this study and the synthesis of POF and the procedure for coating the surface of the IDE devices are discussed. The morphology of the deposited POF film and thickness are measured by SEM. Furthermore, the analysis of the N_2 adsorption isotherm and surface area calculation with BET method are discussed. Finally, the sensing response of the POF coated IDE device towards ethanol and methanol vapors are discussed.

- In Chapter 5, SnO_2 nanoparticles synthesized by spark discharge method are deposited on a MEMS microhotplate device integrated with sensing electrodes to study the sensing response towards ethanol. The design and fabrication of the device developed, methodology for the synthesis of tin oxide particles, and preparation of devices for sensing experiments are discussed. The particle size, crystal structure, and morphology of the films characterized by transmission electron microscopy(TEM), X-ray Diffraction(XRD), and scanning electron microscopy(SEM) are presented. Finally, the characterisation of the fabricated device and the sensing response of the synthesized SnO_2 nanoparticle film towards ethanol is discussed.

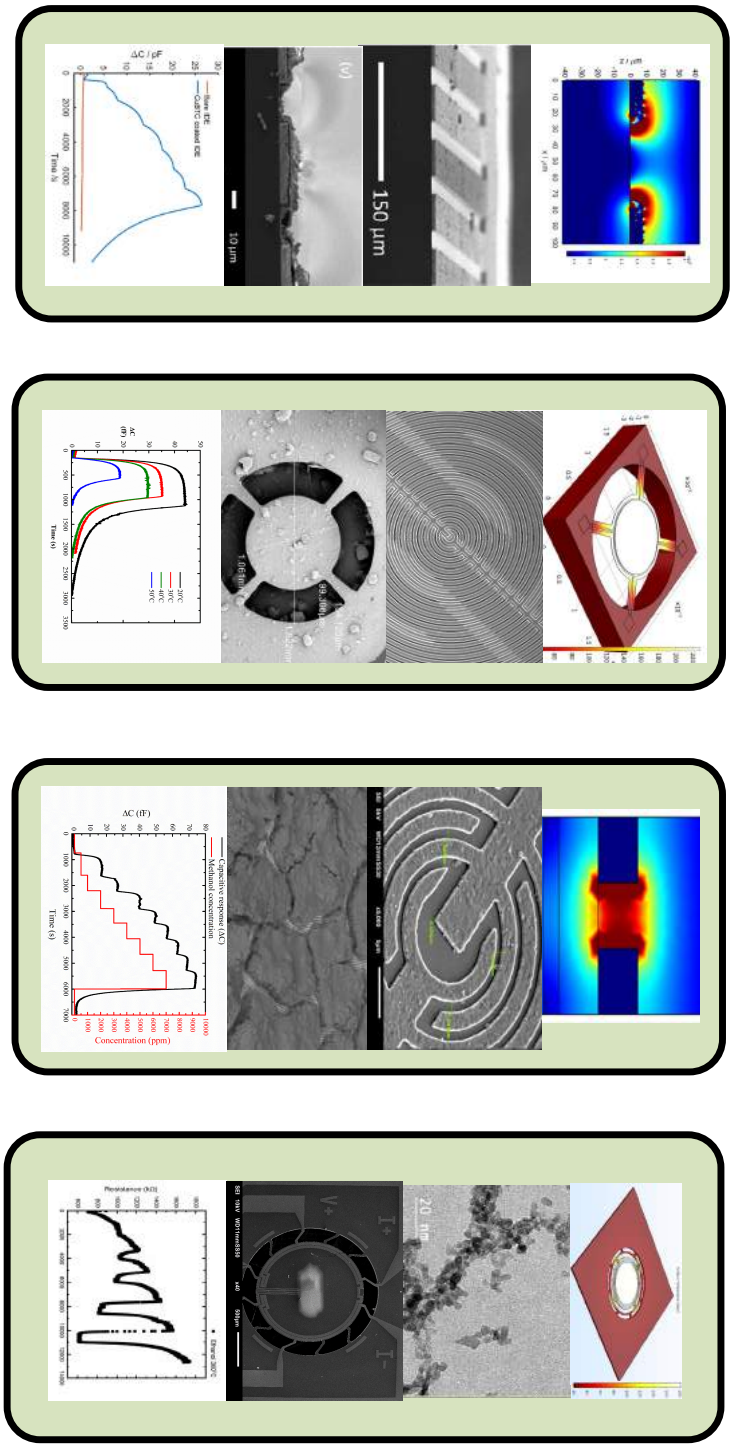

Figure 1.16: Thesis Outline

1

References

[1] G. Q. Zhang and A. van Roosmalen, *More than Moore: creating high value micro/nanoelectronics systems* (Springer Science & Business Media, 2010).

[2] W. Arden, M. Brillouët, P. Cogez, M. Graef, B. Huizing, and R. Mahnkopf, *More-than-moore white paper,* .

[3] E. N. Marieb and S. M. Keller, *Essentials of human anatomy & physiology.* (2017).

[4] J. Fraden, *Handbook of modern sensors*, 5th ed. (Springer, New York, 2016).

[5] B. Pejcic, R. De Marco, and G. Parkinson, *The role of biosensors in the detection of emerging infectious diseases,* Analyst **131**, 1079 (2006).

[6] J. S. Gaffney and N. A. Marley, *Atmospheric chemistry and air pollution,* TheScientificWorldJournal **3**, 199 (2003).

[7] T. C. Pearce, S. S. Schiffman, H. T. Nagle, and J. W. Gardner, *Handbook of machine olfaction,* Willy-VCH, Weinheim (2003).

[8] E. K. Jenkins, M. T. DeChant, and E. B. Perry, *When the nose doesn't know: Canine olfactory function associated with health, management, and potential links to microbiota,* Frontiers in veterinary science **5**, 56 (2018).

[9] I. Manisalidis, E. Stavropoulou, A. Stavropoulos, and E. Bezirtzoglou, *Environmental and health impacts of air pollution: a review,* Frontiers in public health **8** (2020).

[10] R. Montero-Montoya, R. López-Vargas, and O. Arellano-Aguilar, *Volatile organic compounds in air: sources, distribution, exposure and associated illnesses in children,* Annals of global health **84**, 225 (2018).

[11] B. Szulczyński and J. Gębicki, *Currently commercially available chemical sensors employed for detection of volatile organic compounds in outdoor and indoor air,* Environments **4**, 21 (2017).

[12] P. WOLKOFF, *Volatile organic compounds sources, measurements, emission, and the impact on indoor air quality,* Indoor Air, 1995 (1995).

[13] H. Books, *Eh40/2005 workplace exposure limits,* (2011).

[14] S. Vardoulakis, E. Giagloglou, S. Steinle, A. Davis, A. Sleeuwenhoek, K. S. Galea, K. Dixon, and J. O. Crawford, *Indoor exposure to selected air pollutants in the home environment: A systematic review,* International journal of environmental research and public health **17**, 8972 (2020).

[15] A. A. of Clinical Toxicology Ad Hoc Committee on the Treatment Guidelines for Methanol Poisoning, D. G. Barceloux, G. Randall Bond, E. P. Krenzelok, H. Cooper, J. Allister Vale, *et al.*, *American academy of clinical toxicology practice guidelines on the treatment of methanol poisoning,* Journal of toxicology: Clinical toxicology **40**, 415 (2002).

[16] G. W. Hunter, S. Akbar, S. Bhansali, M. Daniele, P. D. Erb, K. Johnson, C.-C. Liu, D. Miller, O. Oralkan, P. J. Hesketh, *et al.*, *Editors' choice—critical review—a critical review of solid state gas sensors,* Journal of The Electrochemical Society **167**, 037570 (2020).

[17] R. Baron and J. Saffell, *Amperometric gas sensors as a low cost emerging technology platform for air quality monitoring applications: A review,* ACS sensors **2**, 1553 (2017).

[18] A. Azad, S. Akbar, S. Mhaisalkar, L. Birkefeld, and K. Goto, *Solid-state gas sensors: A review,* Journal of the Electrochemical Society **139**, 3690 (1992).

[19] S. Lakkis, R. Younes, Y. Alayli, and M. Sawan, *Review of recent trends in gas sensing technologies and their miniaturization potential,* Sensor Review (2014).

[20] Q. Zhu, *Microcantilever sensors in biological and chemical detections,* Sensors & transducers **125**, 1 (2011).

[21] Z. Yunusa, M. N. Hamidon, A. Kaiser, and Z. Awang, *Gas sensors: a review,* Sensors and transducers **168**, 61 (2014).

[22] R. Blue and D. Uttamchandani, *Chemicapacitors as a versatile platform for miniature gas and vapor sensors,* Measurement Science and Technology **28**, 022001 (2016).

[23] S. Feng, F. Farha, Q. Li, Y. Wan, Y. Xu, T. Zhang, and H. Ning, *Review on smart gas sensing technology,* Sensors **19**, 3760 (2019).

[24] X. Liu, S. Cheng, H. Liu, S. Hu, D. Zhang, and H. Ning, *A survey on gas sensing technology,* Sensors **12**, 9635 (2012).

[25] J. Zhu, X. Liu, Q. Shi, T. He, Z. Sun, X. Guo, W. Liu, O. B. Sulaiman, B. Dong, and C. Lee, *Development trends and perspectives of future sensors and mems/nems,* Micromachines **11**, 7 (2020).

[26] *Skive non woven fabric disposal face,* `https://www.amazon.in/SKIVE-Fabric-Disposal-Surgical-Pollution/dp/B095M9TQLN?th=1`.

[27] *iphone,* `https://www.wired.com/2015/09/hands-on-with-the-apple-iphone-6s-and-6s-plus-3d-touch/` ().

[28] *earbuds,* https://www.theverge.com/2020/4/1/21202667/sony-wf-xb700-wh-ch710n-earbuds-headphones-announced-price.

[29] *iwatch,* https://www.iphonehacks.com/2014/09/apple-watch-first-impressions-hands-on-videos-roundup.html ().

[30] H.-C. Zhou, J. R. Long, and O. M. Yaghi, *Introduction to metal–organic frameworks,* Chemical reviews **112**, 673 (2012).

[31] N. Stock and S. Biswas, *Synthesis of metal-organic frameworks (mofs): routes to various mof topologies, morphologies, and composites,* Chemical reviews **112**, 933 (2012).

[32] S. Achmann, G. Hagen, J. Kita, I. M. Malkowsky, C. Kiener, and R. Moos, *Metal-organic frameworks for sensing applications in the gas phase,* Sensors **9**, 1574 (2009).

[33] Y. Li, A.-S. Xiao, B. Zou, H.-X. Zhang, K.-L. Yan, and Y. Lin, *Advances of metal–organic frameworks for gas sensing,* Polyhedron **154**, 83 (2018).

[34] Y. Zhao, M. Zaghloul, Y. Lilach, K. Benkstein, and S. Semancik, *Metal organic framework-coated optical voc gas sensor,* in *2018 IEEE Photonics Conference (IPC)* (IEEE, 2018) pp. 1–2.

[35] J. Hromadka, B. Tokay, R. Correia, S. P. Morgan, and S. Korposh, *Highly sensitive ethanol vapour measurements using a fibre optic sensor coated with metal organic framework zif-8,* in *2017 IEEE SENSORS* (IEEE, 2017) pp. 1–3.

[36] M. Hosseini, S. Zeinali, and M. Sheikhi, *Fabrication of capacitive sensor based on cu-btc (mof-199) nanoporous film for detection of ethanol and methanol vapors,* Sensors and Actuators B: Chemical **230**, 9 (2016).

[37] H. Yamagiwa, S. Sato, T. Fukawa, T. Ikehara, R. Maeda, T. Mihara, and M. Kimura, *Detection of volatile organic compounds by weight-detectable sensors coated with metal-organic frameworks,* Scientific reports **4**, 1 (2014).

[38] I. Ellern, A. Venkatasubramanian, J. H. Lee, P. Hesketh, V. Stavilla, M. D. Allendorf, and A. L. Robinson, *Characterization of piezoresistive microcantilever sensors with metal organic frameworks for the detection of volatile organic compounds,* ECS Transactions **50**, 469 (2013).

[39] A. Demessence, C. Boissiere, D. Grosso, P. Horcajada, C. Serre, G. Férey, G. J. Soler-Illia, and C. Sanchez, *Adsorption properties in high optical quality nanozif-8 thin films with tunable thickness,* Journal of Materials Chemistry **20**, 7676 (2010).

[40] A. Cao, M. Shan, L. Paltrinieri, W. H. Evers, L. Chu, L. Poltorak, J. H. Klootwijk, B. Seoane, J. Gascon, E. J. Sudhölter, *et al.*, *Enhanced vapour sensing using silicon nanowire devices coated with pt nanoparticle functionalized porous organic frameworks,* Nanoscale **10**, 6884 (2018).

[41] M. G. Schwab, B. Fassbender, H. W. Spiess, A. Thomas, X. Feng, and K. Mullen, *Catalyst-free preparation of melamine-based microporous polymer networks through schiff base chemistry,* Journal of the American Chemical Society **131**, 7216 (2009).

[42] S.-C. Chang, *Oxygen chemisorption on tin oxide: correlation between electrical conductivity and epr measurements,* Journal of Vacuum Science and Technology **17**, 366 (1980).

[43] J. Watson, *The tin oxide gas sensor and its applications,* Sensors and Actuators **5**, 29 (1984).

[44] M. Batzill and U. Diebold, *The surface and materials science of tin oxide,* Progress in surface science **79**, 47 (2005).

[45] S. Das and V. Jayaraman, *Sno2: A comprehensive review on structures and gas sensors,* Progress in Materials Science **66**, 112 (2014).

[46] H. Liu, L. Zhang, K. H. H. Li, and O. K. Tan, *Microhotplates for metal oxide semiconductor gas sensor applications—towards the cmos-mems monolithic approach,* Micromachines **9**, 557 (2018).

[47] P. Bhattacharyya, *Technological journey towards reliable microheater development for mems gas sensors: a review,* IEEE Transactions on Device and Materials Reliability **14**, 589 (2014).

[48] F.-Y. Yi, D. Chen, M.-K. Wu, L. Han, and H.-L. Jiang, *Chemical sensors based on metal–organic frameworks,* ChemPlusChem **81**, 675 (2016).

[49] Z. Hu, B. J. Deibert, and J. Li, *Luminescent metal–organic frameworks for chemical sensing and explosive detection,* Chemical Society Reviews **43**, 5815 (2014).

[50] M. G. Campbell, D. Sheberla, S. F. Liu, T. M. Swager, and M. Dincă, *Cu3 (hexaiminotriphenylene) 2: an electrically conductive 2d metal–organic framework for chemiresistive sensing,* Angewandte Chemie International Edition **54**, 4349 (2015).

[51] S. Sachdeva, D. Soccol, D. J. Gravesteijn, F. Kapteijn, E. J. Sudholter, J. Gascon, and L. C. de Smet, *Polymer–metal organic framework composite films as affinity layer for capacitive sensor devices,* ACS sensors **1**, 1188 (2016).

[52] H. Gliemann and C. Wöll, *Epitaxially grown metal-organic frameworks,* Materials today **15**, 110 (2012).

[53] L. Heinke, M. Tu, S. Wannapaiboon, R. A. Fischer, and C. Wöll, *Surface-mounted metal-organic frameworks for applications in sensing and separation,* Microporous and Mesoporous Materials **216**, 200 (2015).

[54] C. Sapsanis, H. Omran, V. Chernikova, O. Shekhah, Y. Belmabkhout, U. Buttner, M. Eddaoudi, and K. Salama, *Insights on capacitive interdigitated electrodes coated with mof thin films: Humidity and vocs sensing as a case study,* Sensors **15**, 18153 (2015).

[55] D. Mohanta and M. Ahmaruzzaman, *Tin oxide nanostructured materials: an overview of recent developments in synthesis, modifications and potential applications,* RSC advances **6**, 110996 (2016).

[56] G. Biskos, V. Vons, C. U. Yurteri, and A. Schmidt-Ott, *Generation and sizing of particles for aerosol-based nanotechnology,* KONA Powder and Particle Journal **26**, 13 (2008).

[57] C. L. Yaws, *The Yaws handbook of vapor pressure: Antoine coefficients* (Gulf Professional Publishing, 2015).

[58] G. W. Thomson, *The antoine equation for vapor-pressure data.* Chemical reviews **38**, 1 (1946).

2

CuBTC MOF

Parts of this chapter have been published as **co-First Author** - "Sensitive and reversible detection of methanol and water vapor by in situ electrochemically grown CuBTC MOFs on interdigitated electrodes". Sachdeva, S.; **Venkatesh, M.R.**; Mansouri, B.E.; Wei, J.; Bossche, A.; Kapteijn, F.; Zhang, G.Q.; Gascon, J.; de Smet, L.; J.R. Sudhölter, E. [1]. *Small* **2017**, *13*, 1604150 **Front Cover Article**.

2.1. Introduction

Recent advances in the microelectronics industry have resulted in the development of miniaturized transduction devices for accurate, real-time detection of various analytes. Such systems require, in addition, affinity layers for the introduction of sensitive, selective and reversible interactions with the analytes to be detected[2][3]. While most of the commercially available sensors utilize metal-oxides as the affinity layer, there is interest for extending the range of affinity materials to reduce cross-sensitivity and to lower energy consumption[4][5]. Recent studies have focused on utilizing Metal-Organic Frameworks (MOFs) for making the affinity layer, because of their high porosity, selective gas adsorption properties and tunability of their well-defined structure[6][7]. These MOFs belong to the class of hybrid materials composed of coordinatively linked metal ions via organic ligands to form the porous crystalline frameworks[8][9]. Hitherto, most of the sensing studies with MOFs were carried out using the material as a bulk powder, while monitoring the change of luminescence properties upon analyte binding[6][10]. Only a few studies have appeared on post-synthetic deposited MOFs on a transducer surface, able to transform the interactions with the analyte into changes of conductivity or dielectric properties[11–13]. The layer-by-layer deposition method has also been used to make thin films of MOFs on the transducer surface[14–16]. While all these multiple-step approaches illustrate well the attractiveness of using MOFs to make selective affinity layers for sensor devices, their further applicability will benefit from developments that shorten the fabrication process of the MOF coatings[17][18].

An interesting approach to grow MOF films directly on metal (transducer) surfaces in a fast and controllable way makes use of the anodic dissolution of the metal ions in the presence of the organic linkers[19–22]. Such an electrochemical deposition procedure can be easily integrated with semiconductor processing techniques[23][24]. The possibility to grow Cu-MOFs as uniform films on flat Cu electrodes making use of cyclic current pulses have been discussed in previous works[25][26]. In this study, we have investigated the electrochemical growth of Cu-MOFs on interdigitated Cu electrodes and its ability to detect methanol and water vapors at room temperature. These analytes were chosen as the model candidates to study the feasibility of this MOF-transducer integration technique due to their known affinity toward CuBTC[27] The interdigitated electrode (IDE) structure allows capacitive detection of the affinity process[28][29]. IDEs can easily be fabricated, are compatible with CMOS technology and are able to operate at room temperature allowing for a low power consumption[28][30].

2.2. Device Design and Fabrication

The capacitor IDEs were fabricated on p-type silicon substrates by optical lithography to pattern the IDE structures (Figure S2.1, Supporting informa-

tion Section 2.6.2). Next, Cu was electroplated utilizing a pre-sputtered 300 nm Cu seed layer as cathode to obtain the planar electrodes with varying widths (W) and gaps (G) ranging from 5 to 50 μm (Figure 2.1(i),(ii),(iii)). For our study, we have used the IDEs with W=G=50μm and a number of electrodes (N) of 100, to ensure a good coverage of the MOF and to prevent electrical shortcuts which might arise at smaller G. Since the total capacitance is a linear function of N, it was set at the indicated value to enhance the overall sensitivity. The height of the Cu electrodes was 6-8μm, as determined by cross-sectional Scanning Electron Microscopy (SEM, Figure 2.1(iv)) and by Dektak profilometry (Figure S2.2, Supporting Information). The spatial wavelength(λ) of the IDE device is defined by[31][32],

$$\lambda = 2(W + G) \tag{2.1}$$

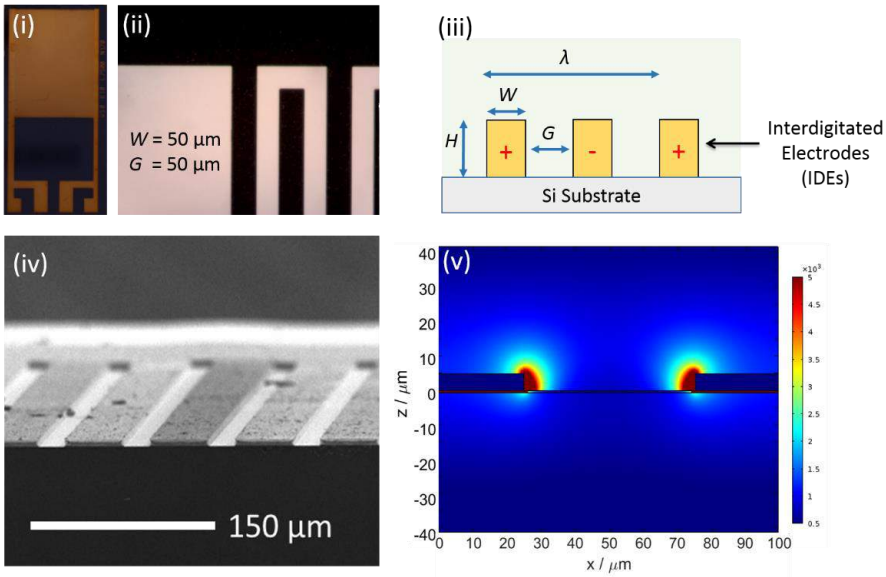

Figure 2.1: Fabricated devices with Interdigitated Electrodes (IDEs). (i) optical image of the fabricated IDE with 4 bond pads in the end for external connections and (ii) optical image of a region of the IDEs with electrodes (black region) with width (W) and gap (G) of each 50μm. (iii) schematic of the device illustrating the dimensions (width (W), gap (G) and height (H) of the electrodes) and spatial wavelength (λ) of the device. (iv) SEM image of the IDEs width of 50μm and gap of 20μm captured at 6° angle view and (v) Figure indicating the distribution and electrical field strength (V/m) calculated across x and z dimensions. Color map indicates a distribution from the weakest (in blue) to the strongest (in red) field strength (V/m).

The sensitivity of the IDE transducer to detect changes in the capacitance

of the affinity layer increases with a smaller value of λ. We have performed theoretical calculations of the electric field properties and the capacitance of our IDE structures making use of COMSOL Multiphysics for a configuration of two electrodes (half spatial wavelength (λ) [31]. The total capacitance was estimated by multiplying the resulting modeled capacitance with (N-1) = 99, to yield a (N-1)*$C_{electrode}$. The width (W) and gap (G) of the IDE structure were both set to 50μm in COMSOL[33], and the height of the electrodes was set to 6μm and 3μm, to simulate the situation before and after the MOF growth process, respectively. From Figure 2.1(v), it can be seen that the field strength remains strongest near the surface of the electrodes. About 75 % of the field lines are found at a distance z, as measured perpendicular to the electrode surface. Near the edges of the electrodes (i.e. region between x=0-25μm and x=75-100μm in Figure 2.1(v)(red colored) the maximal electrical field strength was found. A capacitance of 132pF was calculated for IDE with W=G=50μm and N = 100. Experimentally, the capacitance of the IDE was 3940 ± 0.017pF at 20 kHz (Figure S2.3, Supporting Information). The observed larger capacitance compared to the calculated capacitance is due to the parasitic contributions from the substrate and the wire bonding (≈3000 pF; see Supporting Information, Section 2.6.3).

2.3. Direct growth of CuBTC MOF on Cu-IDE electrodes

The Cu IDEs were used to electrochemically grow thin films of CuBTC MOFs. CuBTC is one of the well characterized and studied MOFs[34][35]. It consists of a Cu paddlewheel framework formed from three Cu ions coordinated with two benzene-1,3,5-tricarboxylate (BTC) ligands[34]. CuBTC has affinity for small-size gases and volatile organic components (VOCs), making it a promising candidate for application as affinity layer on our IDEs[36–39]. CuBTC are grown electrochemically on the Cu IDE structures with a Cu counter-electrode (cathode) in a 10 mL electrochemical cell containing a H_3BTC solution in 96 vol.% ethanol (Supporting Information, Section 2.6.4). Cyclic pulses of the current (6 mA for 5 s followed by no current for 5 s) were applied for 5 min[25]. This resulted in the deposition of crystalline materials on the IDE structure. From X-Ray diffraction (XRD) studies, the formation of CuBTC was proven (Figure 2.2(i))[34][40]. The crystalline layer was uniformly grown and showed a thickness of 5-7 μm as deduced from SEM micrographs (Figure 2.2(iii) and Figure S2.4). Cracks in the CuBTC layers were observed and also some crystallite detachment if the pulses were applied during a longer time period (7.5 min). This is most likely due to induced mechanical stress by the partial dissolution of the copper finger-electrodes and the concomitant formation of CuBTC[20] (Figure S2.5, Supporting Information). The thickness of the IDE electrodes was reduced from 6-8 μm to 3-5μm (Figure 2.2(vi)).

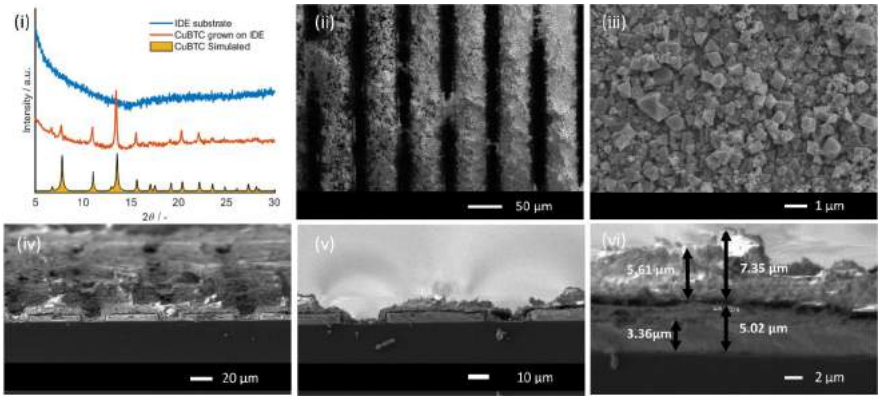

Figure 2.2: (i) Comparison of the XRD pattern for the IDEs with and without CuBTC layer with the simulated pattern of CuBTC. (ii), (iii) SEM images of CuBTC grown over the electrodes. (iv), (v) and (vi) cross-sectional SEM of a coated IDE.

2.4. Sensing study

Sensing measurements of the coated and non-coated devices were carried out at a frequency of 20 kHz and a voltage of 0.1 V using a HP 4284A precision LCR meter. The frequency was chosen as 20 kHz to reduce the noise and parasitic in the measurement. The devices were kept in a custom-built gas mixing and sensing equipment at 30 ± 0.05°C[13]. During the measurements, a continuous stream of dry N_2 was passed over the devices at a flow rate of 200 mL/min using Mass Flow Controllers (MFCs) and perturbations in the form of different analytes (methanol or water) were introduced after a stable base-line was established. The vapors of methanol or water were introduced by first passing dry N_2 through a series of two bubblers containing the analyte to generate a saturated stream of vapors and then diluting it with a parallel stream of dry N_2. The saturated concentration of the analyte was calculated using the Antoine equation[41][42],

$$LogP = A - \frac{B}{T + C} \tag{2.2}$$

Where, P is the saturated vapor pressure of the analyte and T is the temperature of the bubbler. A, B and C are the analyte-dependent constants. After the stabilization and equilibration of the capacitive signal during the measurements, the devices were recovered to the baseline by replacing the stream of N_2 and methanol (or water) with dry N_2.

The obtained CuBTC-modified IDEs were exposed to different concentrations of methanol and water vapor present in a nitrogen carrier gas at 30°C in a custom-built gas mixing and sensing equipment system described

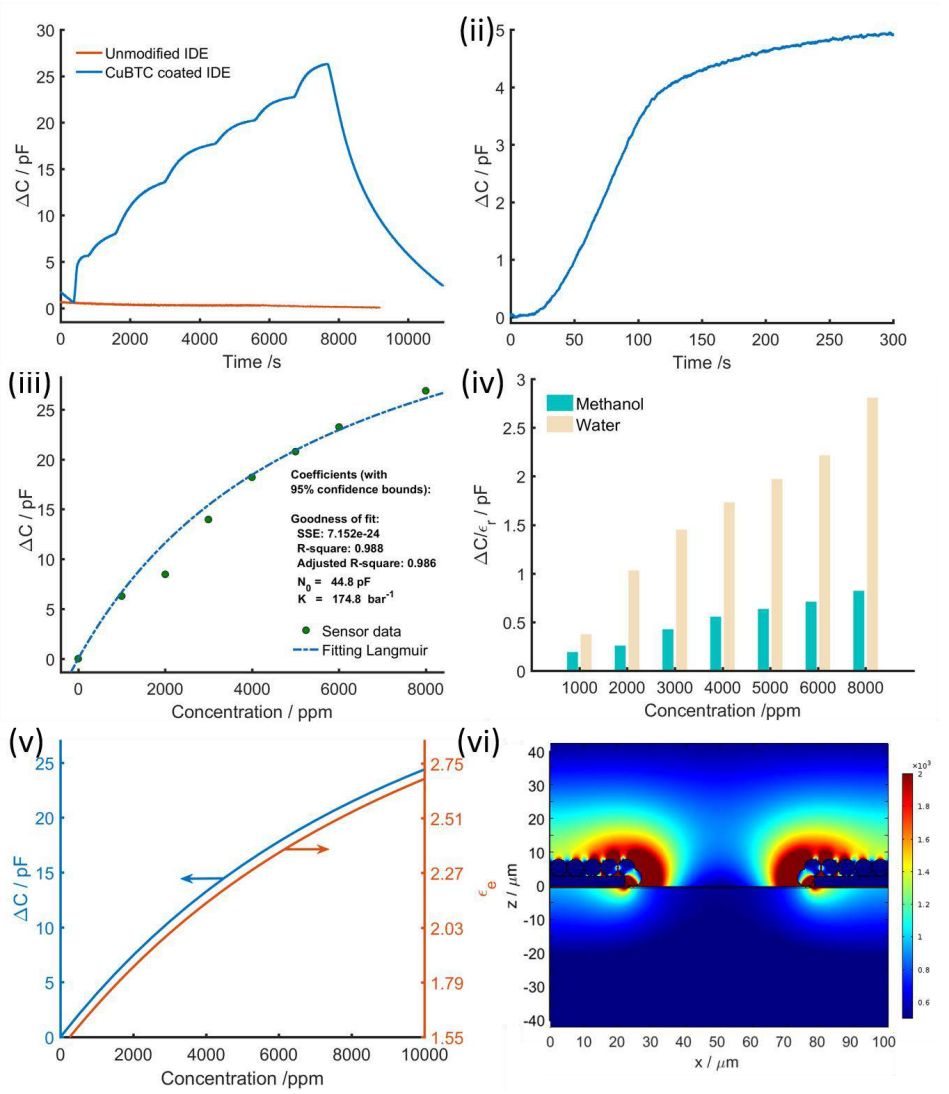

Figure 2.3: (i) Capacitive response of unmodified IDE (red) and CuBTC-coated IDE (blue) towards methanol. (ii) Capacitive response vs time of CuBTC-coated IDE towards 1000 ppm of methanol vapour. (iii) Quantitative behavior of the sensor device towards methanol vapour and its fitting with the Langmuir model. (iv) Comparison between the response towards methanol and water vapour normalized with respect to the dielectric constants of analyte. (v) Estimated dielectric constant(red) and capacitive change(blue) of these devices with methanol concentration as deduced by finite element analysis. (vi) Simulated distribution of the electric field strength, |E| over the IDE geometry. Color map indicates a distribution from the weakest (in blue) to the strongest (in red) field strength (V/m).

previously[13]. The capacitance changes were determined by using impedance spectroscopy at a constant frequency of 20 kHz. In Figure 2.3(i), the capacitive response of 5-25 pF is shown upon the exposure to 1000-8000 ppm of methanol at a constant flow rate of 200 mL/min and compared with the unmodified IDE, which showed no response. The response of the modified device to methanol vapor was completely reversible. The desorption time is longer than the adsorption time, reflecting the favorable methanol affinity.

The capacitive response started a few seconds after applying the methanol and reached a stable value in 120-150 s (Figure 2.3(ii)). Such fast response clearly reflects the presence of the thin CuBTC layer with its high porosity (having a BET surface area of 1300 m^2/g and a pore volume of 0.73 cm^3/g)[27]. In contrast, Amino-MIL-53(Al) MOF blended in a Matrimid polymeric matrix, show a 12 times slower response[13]. This slower response is the result of the presence of the polymer, which acts as a diffusion barrier[13].

The capacitance response, (ΔC) in the measured methanol concentration range was further related to the concentration of methanol in the CuBTC affinity layer near the transducer by applying a Langmuir isotherm model as indicated in Figure 2.3(iii) and described by Equation 5:

$$\frac{\triangle C}{\triangle C_s} = \frac{K_e\ c_m}{1 + K_e\ c_m} \tag{2.3}$$

where C_s, K_e, c_m indicate the saturation capacitance, affinity constant, concentration of methanol in the measurement chamber and saturated amount of methanol adsorbed, respectively. K_e and C_s were determined to be 174.8 bar^{-1} and $\approx$44.8 pF by non-linear least square fitting of Equation 2.3 to the experimental sensor response. Even though C_s indicates that the adsorption capacity is still far from saturation, extrapolation to higher concentration has to be done carefully as multiple-site adsorption and pore filling in CuBTC can result in deviations from Langmuir behavior[27].

With an accuracy of our equipment (HP 4284A LCR meter) in the fF range, the sensitivity of the devices is clearly indicated by changes of 5 pF/1000 ppm of methanol. The CuBTC-modified IDEs were also exposed to different concentrations of water vapor and the results were compared with the responses observed to methanol (Figure 2.3(iv)). The responses were therefore corrected for the differences of dielectric constants of methanol and water by dividing the observed capacitance change by the respective dielectric constants ($\epsilon_{r,methanol}$ = 32.7, $\epsilon_{r,water}$ = 78). The affinity of the CuBTC towards water vapor shows to be much stronger than the observed affinity to methanol. This observation confirms earlier studies[36].

The methanol adsorption by the CuBTC framework also changes the effective local dielectric constant (ϵ_e). This (ϵ_e) was approximated utilizing the Bruggeman effective medium approximation[43] which is based on changes in the volumetric fraction(f) (Supporting information, Section 2.6.5). The relative static dielectric constant of CuBTC[44] (in vacuum) was assumed to be

ϵ_r = 1.7. It can be seen in Figure 2.3(v) that the calculated (ϵ_e) roughly increases from ≈1.5 to ≈2.7 on exposure from 0 to 8000 ppm of methanol (ϵ_r =32.7). The calculated capacitance (by finite element modeling) for these dielectric constant changes indicated correspondence with the measured capacitance changes confirming the role of changes in local polarity on the adsorption of polar molecules like methanol. Finally, the simulated electric field strength of these MOF-modified electrodes indicated a slight decrease with this increase of ϵ_r to 2.7 as shown in Figure 2.3(vi) and Figure S 2.8(Supporting information).

2.5. Conclusions

In this study, the methodology and development of electrochemical grown CuBTC MOFs on Cu IDEs was discussed. These devices show a fast response (120-150s to saturation), are sensitive and have reversible sensing properties useful for the quantitative detection of methanol and water vapor in the 1000-8000 ppm range. Equilibrium capacitive responses also followed the Langmuir adsorption model with an affinity constant of 174 bar^{-1} for methanol concentrations up to 8000 ppm. Comparative sensing studies with methanol and water indicated higher sensitivity towards water due to its stronger affinity to the CuBTC. Theoretical estimations of the local dielectric constants by application of the Bruggeman approximation, indicated that on the exposure to different methanol vapor concentrations (0-8000 ppm), the relative dielectric constant of partially filled CuBTC layer increases from ≈1.5 to ≈2.7 as a result of the uptake of methanol. The calculated capacitance changes correlate very well with the experimentally observed data, supporting our applied methods. In conclusion, we have shown that CuBTC MOFs can be formed in situ electrochemically on micro-structured copper IDEs in a fast and easy way. These devices act as fast, reversible and sensitive sensors for the quantitative detection of methanol and water vapor in the range of 1000 to 8000 ppm.

2.6. Supplementary Information

2.6.1. Experimental section

All chemicals were purchased from Sigma Aldrich and used as received. The device fabrication was carried out in a clean-room environment. Scanning Electron Microscopy (SEM) micrographs were acquired at different magnifications using a JEOL JSM 6360 microscope and a Nova NanoSEM^{TM} (for cross-sectional images). The powder X-Ray Diffraction (pXRD) patterns of IDEs with and without MOF deposition were recorded using the Bruker D8 Advance diffractometer with Co-Kα radiation (λ = 1.788897 Å).

2.6.2. Device Fabrication

The copper (Cu) interdigitated electrode (IDE) devices were fabricated on a p-type Silicon substrate (100) with a thickness of 300μm. The fabrication process is summarized schematically in Figure S2.1. First, a 500 nm thick Si_3N_4 layer was deposited by low pressure chemical vapour deposition (LPCVD) at 850°C followed by the deposition of 300 nm adhesion layer of Titanium Nitride (TiN) using a TRIKON SIGMA sputter coater. A Cu-seed layer of a 300 nm thick was deposited on top of the TiN layer in a similar fashion. IDEs were patterned using an AZ960 positive photo-resist by photo-lithography for 60 s using a contact aligner. After the IDE patterning, the wafers were developed using AZ400K for ≈120 s. The Cu electrodes were then electroplated in the non-patterned region containing Cu seed layer by applying a current of 1 A for 900 s using the MECO electroplating equipment. After electroplating, the photo-resist was stripped by using acetone and iso-propanol. The exposed Cu seed layer and TiN layer (below the photo-resist patterns) were removed by first immersing the wafer to a solution of 5 g of $Na_2S_2O_8$ in a mixture of 1.25 mL H_2SO_4 (96%) and 500 mL distilled water for 20 minutes to remove the Cu seed layer followed by dipping the wafer to a solution containing 25 mL NH_4OH (25%), 100 mL H_2O_2 (30%) and 100 mL distilled water for removing the TiN layer. After the fabrication, the wafer was diced and wire-bonded for external electrical connections. These devices are then used for electrochemical growth of MOFs.

2.6.3. Calculation of the parasitic contribution of the devices

Parasitic contribution in the IDE structure is mainly introduced by the substrate and can be approximated using the following standard capacitance equation:

$$C = \frac{\varepsilon_0 \varepsilon_r A}{t} \tag{2.4}$$

where ε_r is the dielectric constant of Si_3N_4 layer ((ε_r) = 9.7) and A is

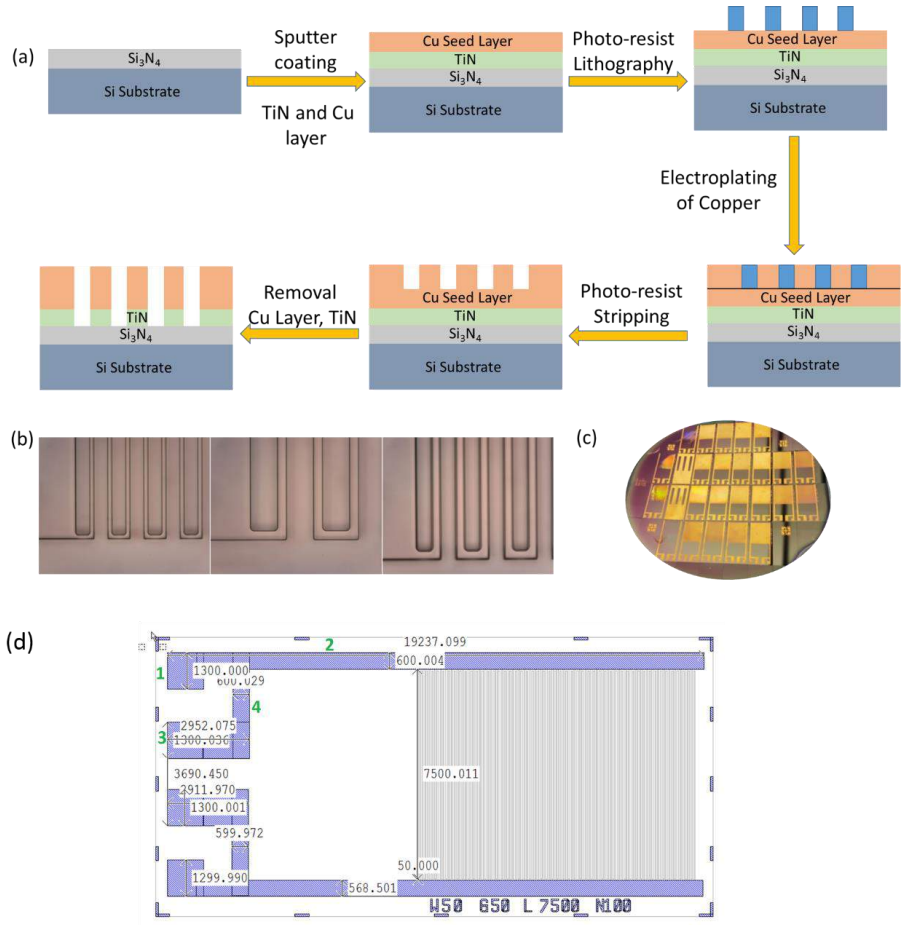

Figure S 2.1: (a) Schematic of the fabrication process for the Cu-interdigitated electrode devices. (b) Lithographic pattern of the Cu-IDE structure. (c) Optical image of the fabricated devices (d) Cu IDE layout with dimensions in μm indicating width (W) and gap (G) of 50μm each and number of electrodes (N) of 100.

the area and the t (= 500 nm) is the thickness of Si_3N_4 layer. There are 4 components in the IDE structure which contribute for the capacitance in parallel to the capacitance of the IDE structure (labeled 1-4 in Figure S2.6.2d). These components are classified as (1) Square bond pads (0.2932 nF), (2) Side electrode lines (1.8677 nF), (3) 2nd Bond Pad (0.666 nF) and (4) Connecting electrode line (0.2083 nF). The total parasitic contribution from both finger electrodes was calculated to be 3.06 nF. The difference between the calculated capacitance with the measured capacitance can be attributed to the parasitic

from the soldered wiring.

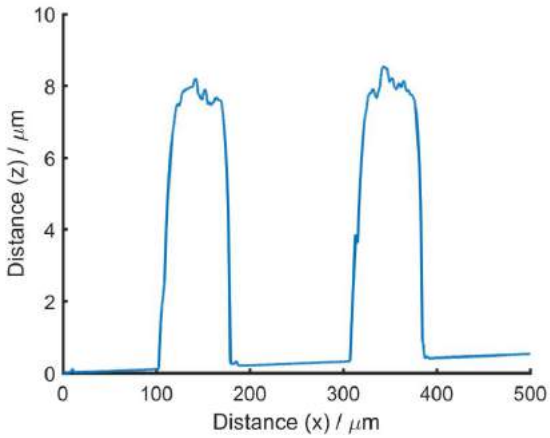

Figure S 2.2: DEKTAK 8 profilometer data of the bare IDE with a width = 50μm, a gap = 20μm and a height of 7-8μm. The measurement was done over the reference points (not over the electrodes) in IDE structure to avoid damage to the device.

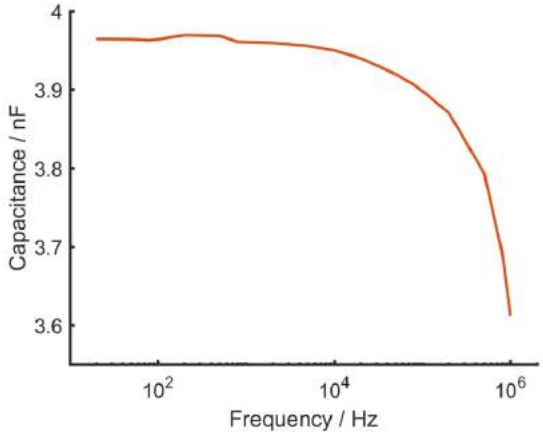

Figure S 2.3: Measured capacitance of the non-coated IDE with width and gap of 50μm each at different frequencies

2.6.4. Electrochemical Synthesis of MOFs

100 mg of the organic linker (H_3BTC or H_3TATB) and 25 mg of the electrolyte Methyl-TriButylammonium methyl Sulfate (MTBS) were dissolved in 8 mL of 96 vol.% ethanol solution. The solution was mixed in the 10 mL electrochemical cell at room temperature[25]. The MOF synthesis over the IDEs was carried out in a two-electrode system by using both electrodes of IDEs as anode (by electrically shorting) with a copper plate as the cathode. Cyclic pulses of current with 6 mA/5 s and 0 mA /5 s were applied for 5 min using an Autolab potentiostat PGSTAT302N. After the MOF growth, the devices were washed in the ethanol solution overnight at room temperature and dried at 100°C for 2 h.

The SEM images of the electrochemical synthesis of CuBTC MOF is shown in Figure S2.4 and Figure S2.5.

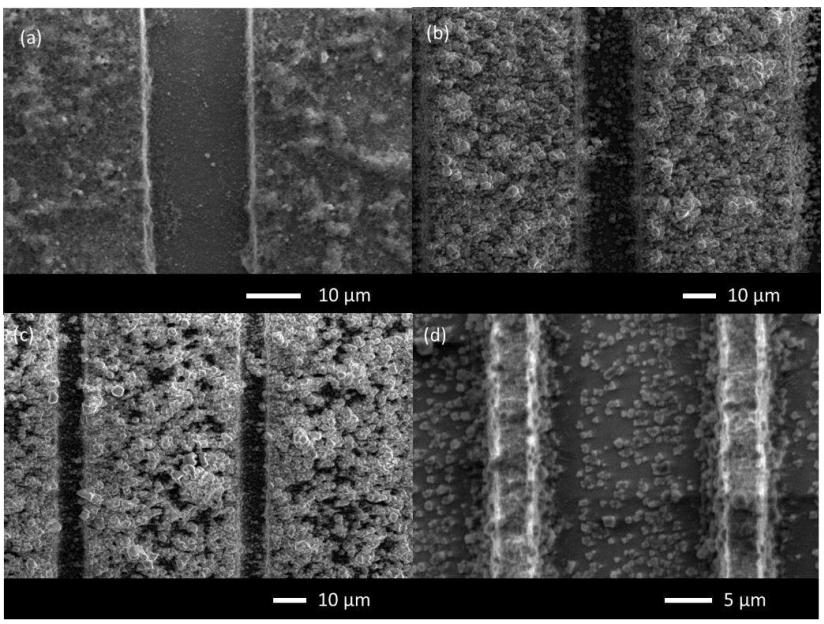

Figure S 2.4: Electrochemical synthesis of CuBTC over IDEs prepared with negative photoresist and different dimensions. SEM micrograph of (a) a bare IDE, (b) CuBTC coated device with width and gap of 50μm and 20μm, respectively, (c) the coated IDEs with width and gap of 50μm and 10μm, respectively and (d) the coated IDEs the width and gap of 5μm and 20μm, respectively.

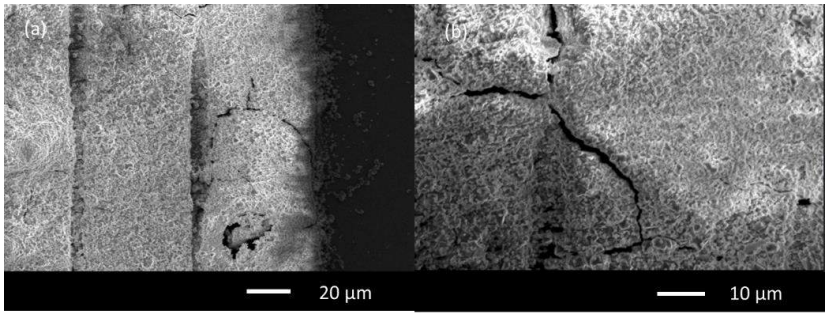

Figure S 2.5: SEM micrographs indicating crack formation in the CuBTC layer over synthesis for longer duration (7.5 min). (a) and (b) show the regions of a CuBTC-coated IDE at different magnifications.

2.6.5. Theoretical estimation of changes in the dielectric constant

For a porous structure like present in CuBTC, the effective dielectric constant (ϵ_e) can be approximated utilizing the Bruggeman effective medium approximation based on the changes in the volumetric fraction(f)[43],

$$f_{CuBTC}\frac{\epsilon_{CuBTC}-\epsilon_e}{\epsilon_{CuBTC}+2\epsilon_e}+f_{N_2}\frac{\epsilon_{N_2}-\epsilon_e}{\epsilon_{N_2}+2\epsilon_e}+f_{MeOH}\frac{\epsilon_{MeOH}-\epsilon_e}{\epsilon_{MeOH}+2\epsilon_e}=0 \tag{2.5}$$

$$f_{CuBTC}+f_{N_2}+f_{MeOH}=1 \tag{2.6}$$

Where ϵ_{CuBTC}, ϵ_{N_2} and ϵ_{MeOH} are the dielectric constant of CuBTC, nitrogen and Methanol respectively. f_{CuBTC}, f_{N_2} and f_{MeOH} are the volume fraction of CuBTC, nitrogen and Methanol in the total volume of the film. All the parameters used for the calculations are listed in Table 2.1. The static dielectric constant of CuBTC (without air) was assumed to be 1.7[44].

In order to estimate the changes in the dielectric constant of the layer, first the amount of the MOF deposited on the IDEs was estimated based on the measured thickness across the dimensions of the electrode.

$$m_{CuBTC}=(V_{CuBTC+IDE}-V_{IDE})\times\rho \tag{2.7}$$

Where m_{CuBTC} is the mass of the CuBTC deposited on top of the electrodes, $V_{CuBTC+IDE}$ is the total volume of the coated IDEs and V_{IDE} represents the volume of the electrodes. Assuming the Langmuir behaviour in the measured concentration range, the total number of moles of methanol adsorbed inside the pores of MOF was estimated utilizing the parameters listed

Table 2.1: Parameters used for calculation of the effective dielectric constant.

Parameters	Value
P_{atm}	101325 Pa
R	8.3145 m^3Pa/K mol
Temperature	303 K
Number of electrodes (N)	100
Length of the electrode	7.5mm
Width of the electrode	46μm
Thickness of the electrode	3μm
Length of the electrode with MOF	7μm
Width of the electrode with MOF	56μm
Thickness of the electrode with MOF	8μm
Saturation amount of MeOH	0.64 g/g
K, equilibrium constant	174.8 bar^{-1}
Bulk Density of CuBTC	0.35 g/cm^3
Pore Volume of CuBTC[27]	0.731 cm^3/g
Dielectric Constant of CuBTC[44]	1.7
Dielectric Constant of Methanol	32.7
Dielectric Constant of Air	1

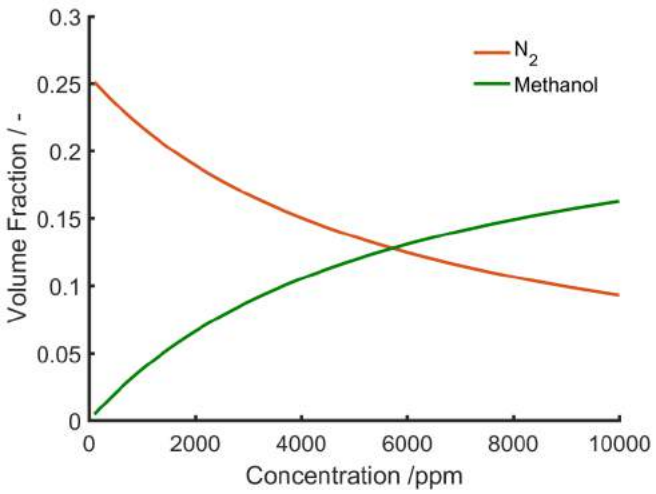

Figure S 2.6: Changes in the volume fraction of methanol and N_2 in the pores of MOF over the exposure to different concentrations of methanol.

in Table 2.1. This amount of methanol was then converted into volume fraction with the assumption of rigid MOF structure and replacement of nitrogen by

methanol. The changes in the volume fraction (f) of methanol inside the pores of CuBTC calculated on exposure to different concentrations of methanol vapor with the assumption of a Langmuir behavior of adsorption is shown in Figure S2.6. For 1000 ppm of methanol in N_2, f_{MeOH} was calculated to be 0.038.

2.6.6. Theoretical calculations of changes in electric field strength

The electric field distribution of MOF coated IDEs is shown in Figure S2.7. The changes in the dielectric constant over changes in the methanol concentration also result in changes in the electric field. A higher dielectric constant lead to a slight reduction in the electric field strength due to increase in the charge storage (Figure S2.8).

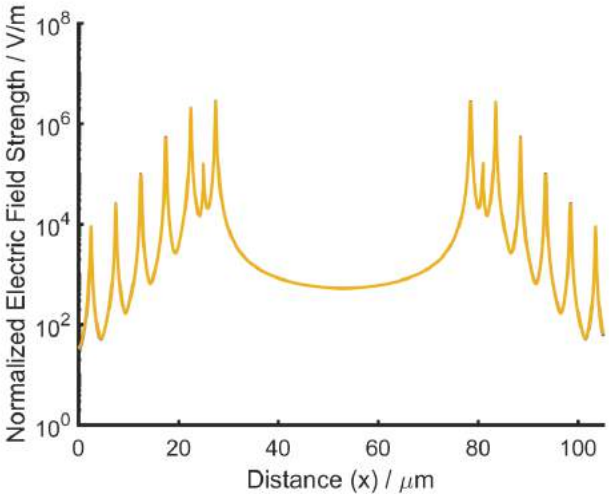

Figure S 2.7: Distribution of the electrical field strength across the x-axis over the MOF modified IDEs in a geometry of half-spatial wavelength. ($\lambda/2$).

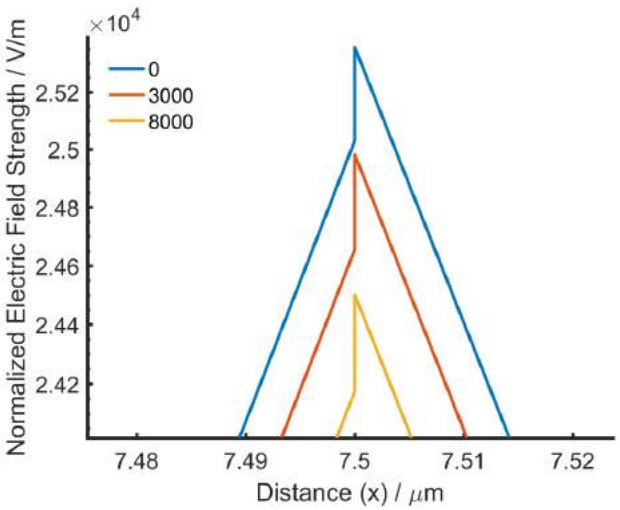

Figure S 2.8: Distribution of the electrical field strength at a localized position over the increase in concentration of methanol (0-8000 ppm)

References

[1] S. Sachdeva, M. R. Venkatesh, B. E. Mansouri, J. Wei, A. Bossche, F. Kapteijn, G. Q. Zhang, J. Gascon, L. C.P.M. de Smet, and E. J.R. Sudhölter, *Sensitive and reversible detection of methanol and water vapor by in situ electrochemically grown cubtc mofs on interdigitated electrodes,* Small **13** (2017).

[2] C. Hagleitner, A. Hierlemann, D. Lange, A. Kummer, N. Kerness, O. Brand, and H. Baltes, *Smart single-chip gas sensor microsystem,* Nature **414**, 293 (2001).

[3] X.-J. Huang and Y.-K. Choi, *Chemical sensors based on nanostructured materials,* Sensors and Actuators B: Chemical **122**, 659 (2007).

[4] D. R. Miller, S. A. Akbar, and P. A. Morris, *Nanoscale metal oxide-based heterojunctions for gas sensing: a review,* Sensors and Actuators B: Chemical **204**, 250 (2014).

[5] Y.-F. Sun, S.-B. Liu, F.-L. Meng, J.-Y. Liu, Z. Jin, L.-T. Kong, and J.-H. Liu, *Metal oxide nanostructures and their gas sensing properties: a review,* Sensors **12**, 2610 (2012).

[6] F.-Y. Yi, D. Chen, M.-K. Wu, L. Han, and H.-L. Jiang, *Chemical sensors based on metal–organic frameworks,* ChemPlusChem **81**, 675 (2016).

[7] I. Stassen, B. Bueken, H. Reinsch, J. Oudenhoven, D. Wouters, J. Hajek, V. Van Speybroeck, N. Stock, P. Vereecken, R. Van Schaijk, *et al.*, *Towards metal–organic framework based field effect chemical sensors: Uio-66-nh 2 for nerve agent detection,* Chemical science **7**, 5827 (2016).

[8] D. J. Wales, J. Grand, V. P. Ting, R. D. Burke, K. J. Edler, C. R. Bowen, S. Mintova, and A. D. Burrows, *Gas sensing using porous materials for automotive applications,* Chemical Society Reviews **44**, 4290 (2015).

[9] A. U. Czaja, N. Trukhan, and U. Müller, *Industrial applications of metal–organic frameworks,* Chemical Society Reviews **38**, 1284 (2009).

[10] Z. Hu, B. J. Deibert, and J. Li, *Luminescent metal–organic frameworks for chemical sensing and explosive detection,* Chemical Society Reviews **43**, 5815 (2014).

[11] M. G. Campbell, D. Sheberla, S. F. Liu, T. M. Swager, and M. Dincă, *Cu3 (hexaiminotriphenylene) 2: an electrically conductive 2d metal–organic framework for chemiresistive sensing,* Angewandte Chemie International Edition **54**, 4349 (2015).

[12] S. Achmann, G. Hagen, J. Kita, I. M. Malkowsky, C. Kiener, and R. Moos, *Metal-organic frameworks for sensing applications in the gas phase,* Sensors **9**, 1574 (2009).

[13] S. Sachdeva, D. Soccol, D. J. Gravesteijn, F. Kapteijn, E. J. Sudholter, J. Gascon, and L. C. de Smet, *Polymer–metal organic framework composite films as affinity layer for capacitive sensor devices,* ACS sensors **1**, 1188 (2016).

[14] H. Gliemann and C. Wöll, *Epitaxially grown metal-organic frameworks,* Materials today **15**, 110 (2012).

[15] L. Heinke, M. Tu, S. Wannapaiboon, R. A. Fischer, and C. Wöll, *Surface-mounted metal-organic frameworks for applications in sensing and separation,* Microporous and Mesoporous Materials **216**, 200 (2015).

[16] C. Sapsanis, H. Omran, V. Chernikova, O. Shekhah, Y. Belmabkhout, U. Buttner, M. Eddaoudi, and K. Salama, *Insights on capacitive interdigitated electrodes coated with mof thin films: Humidity and vocs sensing as a case study,* Sensors **15**, 18153 (2015).

[17] H. K. Arslan, O. Shekhah, J. Wohlgemuth, M. Franzreb, R. A. Fischer, and C. Wöll, *High-throughput fabrication of uniform and homogenous mof coatings,* Advanced functional materials **21**, 4228 (2011).

[18] I. Stassen, M. Styles, G. Grenci, H. Van Gorp, W. Vanderlinden, S. De Feyter, P. Falcaro, D. De Vos, P. Vereecken, and R. Ameloot, *Chemical vapour deposition of zeolitic imidazolate framework thin films,* Nature materials **15**, 304 (2016).

[19] W.-J. Li, M. Tu, R. Cao, and R. A. Fischer, *Metal–organic framework thin films: electrochemical fabrication techniques and corresponding applications & perspectives,* Journal of Materials Chemistry A **4**, 12356 (2016).

[20] N. Campagnol, T. R. Van Assche, M. Li, L. Stappers, M. Dincă, J. F. Denayer, K. Binnemans, D. E. De Vos, and J. Fransaer, *On the electrochemical deposition of metal–organic frameworks,* Journal of Materials Chemistry A **4**, 3914 (2016).

[21] I. Stassen, M. Styles, T. Van Assche, N. Campagnol, J. Fransaer, J. Denayer, J.-C. Tan, P. Falcaro, D. De Vos, and R. Ameloot, *Electrochemical film deposition of the zirconium metal–organic framework uio-66 and application in a miniaturized sorbent trap,* Chemistry of materials **27**, 1801 (2015).

[22] B. Van de Voorde, R. Ameloot, I. Stassen, M. Everaert, D. De Vos, and J.-C. Tan, *Mechanical properties of electrochemically synthesised metal–organic framework thin films,* Journal of Materials Chemistry C **1**, 7716 (2013).

[23] M. Beidaghi and Y. Gogotsi, *Capacitive energy storage in micro-scale devices: recent advances in design and fabrication of micro-supercapacitors,* Energy & Environmental Science **7**, 867 (2014).

[24] G. Oskam, J. Long, A. Natarajan, and P. Searson, *Electrochemical deposition of metals onto silicon,* Journal of Physics D: Applied Physics **31**, 1927 (1998).

[25] S. Sachdeva, A. Pustovarenko, E. J. Sudhölter, F. Kapteijn, L. C. de Smet, and J. Gascon, *Control of interpenetration of copper-based mofs on supported surfaces by electrochemical synthesis,* CrystEngComm **18**, 4018 (2016).

[26] A. Martinez Joaristi, J. Juan-Alcañiz, P. Serra-Crespo, F. Kapteijn, and J. Gascon, *Electrochemical synthesis of some archetypical zn2+, cu2+, and al3+ metal organic frameworks,* Crystal Growth & Design **12**, 3489 (2012).

[27] T. R. Van Assche, T. Duerinck, J. J. Gutierrez Sevillano, S. Calero, G. V. Baron, and J. F. Denayer, *High adsorption capacities and two-step adsorption of polar adsorbates on copper–benzene-1, 3, 5-tricarboxylate metal–organic framework,* The Journal of Physical Chemistry C **117**, 18100 (2013).

[28] N. F. Sheppard, R. C. Tucker, and C. Wu, *Electrical conductivity measurements using microfabricated interdigitated electrodes,* Analytical Chemistry **65**, 1199 (1993).

[29] U. Altenberend, F. Molina-Lopez, A. Oprea, D. Briand, N. Bârsan, N. F. De Rooij, and U. Weimar, *Towards fully printed capacitive gas sensors on flexible pet substrates based on ag interdigitated transducers with increased stability,* Sensors and Actuators B: Chemical **187**, 280 (2013).

[30] Y. Lu, J. Li, J. Han, H.-T. Ng, C. Binder, C. Partridge, and M. Meyyappan, *Room temperature methane detection using palladium loaded single-walled carbon nanotube sensors,* Chemical Physics Letters **391**, 344 (2004).

[31] R. Igreja and C. Dias, *Analytical evaluation of the interdigital electrodes capacitance for a multi-layered structure,* Sensors and Actuators A: Physical **112**, 291 (2004).

[32] R. Igreja and C. Dias, *Dielectric response of interdigital chemocapacitors: The role of the sensitive layer thickness,* Sensors and Actuators B: Chemical **115**, 69 (2006).

[33] P. Oikonomou, A. Salapatas, K. Manoli, K. Misiakos, D. Goustouridis, E. Valamontes, M. Sanopoulou, I. Raptis, and G. Patsis, *Chemocapacitance response simulation through polymer swelling and capacitor modeling,* Procedia Engineering **25**, 423 (2011).

[34] S. S.-Y. Chui, S. M.-F. Lo, J. P. Charmant, A. G. Orpen, and I. D. Williams, *A chemically functionalizable nanoporous material [cu3 (tma) 2 (h2o) 3] n,* Science **283**, 1148 (1999).

[35] T. R. Van Assche, G. Desmet, R. Ameloot, D. E. De Vos, H. Terryn, and J. F. Denayer, *Electrochemical synthesis of thin hkust-1 layers on copper mesh,* Microporous and Mesoporous Materials **158**, 209 (2012).

[36] S. Calero and P. Gomez-Alvarez, *Insights into the adsorption of water and small alcohols on the open-metal sites of cu–btc via molecular simulation,* The Journal of Physical Chemistry C **119**, 467 (2014).

[37] P. Davydovskaya, A. Ranft, B. V. Lotsch, and R. Pohle, *Analyte detection with cu-btc metal–organic framework thin films by means of mass-sensitive and work-function-based readout,* Analytical chemistry **86**, 6948 (2014).

[38] M. Hosseini, S. Zeinali, and M. Sheikhi, *Fabrication of capacitive sensor based on cu-btc (mof-199) nanoporous film for detection of ethanol and methanol vapors,* Sensors and Actuators B: Chemical **230**, 9 (2016).

[39] J. B. DeCoste and G. W. Peterson, *Metal–organic frameworks for air purification of toxic chemicals,* Chemical reviews **114**, 5695 (2014).

[40] A. Vishnyakov, P. I. Ravikovitch, A. V. Neimark, M. Bülow, and Q. M. Wang, *Nanopore structure and sorption properties of cu- btc metal- organic framework,* Nano Letters **3**, 713 (2003).

[41] C. L. Yaws, *The Yaws handbook of vapor pressure: Antoine coefficients* (Gulf Professional Publishing, 2015).

[42] G. W. Thomson, *The antoine equation for vapor-pressure data.* Chemical reviews **38**, 1 (1946).

[43] K. Lazarova, B. Georgieva, M. Spasova, and T. Babeva, *Preparation and characterization of mesoporous nb2o5 films for sensing applications,* in *Journal of Physics: Conference Series*, Vol. 558 (IOP Publishing, 2014) p. 012042.

[44] K. Zagorodniy, G. Seifert, and H. Hermann, *Metal-organic frameworks as promising candidates for future ultralow-k dielectrics,* Applied Physics Letters **97**, 251905 (2010).

3

ZIF-8 MOF

Parts of this chapter is part of the publication - "A Low-Power MEMS IDE Capacitor with Integrated Microhotplate: Application as Methanol Sensor using a Metal-Organic Framework Coating as Affinity Layer". **Venkatesh, M.R.**;Sachdeva, S.; Mansouri, B.E.; Wei, J.; Bossche, A.; Zhang, G.Q.; de Smet, L.C.P.M; J.R. Sudhölter, E. *MDPI Sensors* **2019**, **Special Issue - Metal-Organic Frameworks for Various Sensing Applications**.

3.1. Introduction

Methanol is an organic solvent found in dyes, paints, perfumes and automotive fuel. Methanol is a colorless liquid, with a mild odor and flammable volatile organic compound (VOC). The threshold limit value (TLV) of exposure to methanol without causing adverse health effect is 200 ppm [1]. Monitoring of exposure to VOCs is important for health and well-being in an indoor air environment. Prolonged exposure to methanol for concentrations higher than TLV can cause headaches, drowsiness, and eye irritation. Methanol sensors developed using various metal-oxide semiconductors, such as SnO_2, In_2O_3, α-Fe_2O_3 and ZnO operating at temperatures of 250 °C–350 °C require high-power transducers [1]. The development of a low-power sensor for the detection of methanol is not only interesting from a research point of view, but also useful for portable and wearable air quality systems.

In recent years, there has been much interest in the synthesis and development of porous materials such as zeolites and metal-organic frameworks (MOFs) for gas adsorption and sensing applications [2]. Metal-organic frameworks are crystalline materials formed of metal ions connected by organic linkers. The availability of various metal ions, organic linkers, and structure motif enables infinite topology combinations with unique chemical and physical properties [2]. MOFs as affinity layers is particularly interesting for various chemical vapors and gases due their high surface area, porous structure, tunability in material processing and development of thin film on electronic sensor devices [3]. Most MOFs inherently have low conductivity and the detection of gases has been mainly investigated using electronic devices such as chemi-resistive, chemi-capacitive cantilevers, quartz microbalance (QCM), and Field-effect transistors (FETs) [3, 4]. Recent progress has been done in the development of conductive MOFs as affinity layers for chemi-resistive sensors [5–7].

Among the several MOF structures, Zeolitic imidazolate frameworks (ZIFs) are a class of MOF with metal ions (Zn, Co) with imidazolate linkers. They possess high porosity, ultra-high surface areas, and good thermal stability [8]. The adsorption and desorption of methanol have been investigated in the microporous structure of ZIF-8 MOF films deposited on silicon substrate [9]. ZIF-8 MOF consists of cages with an effective diameter of 12.5Å and a hexagonal aperture of 3.3 Å. Methanol, with a kinetic diameter of 3.8 Å, can enter the microporous cage of ZIF-8 MOF and interact with the Zn atoms. On average, 2.7 molecules can adsorb per Zn atom [10]. ZIF-8 MOF have large surface area (1030 m^2g^{-1}) and high adsorption capacity of methanol, making it a suitable affinity layer for its investigation as a methanol sensor [10]. The detection of adsorbed alcohols using ZIF-8 MOF has been studied using several optical-based techniques [11, 12]. ZIF-8 films grown on Fabry-Perot device enables detection of ethanol vapor by measuring the shifts in the interference of transmission spectrum [13]. Thin film ZIF-8 MOF-coated on optical fiber long period grating (LPG) has been shown to detect ethanol, methanol and acetone

vapors in ranges up to 10,000 ppm [12]. However, ZIF-8 films as affinity layer for sensing of alcohols using techniques apart from optical-based techniques, such as capacitive sensing studies, have not been investigated. Detection of alcohols with thin film MOFs has been studied by measuring the changes in permittivity of the material using capacitive interdigitated electrode (IDE) transducers [14]. Cu paddlewheel MOFs using benzene-1,3,5-tricarboxylic acid as organic linkers (CuBTC) grown on IDE capacitor and NH_2-MIL-53(Al) MOFs in Matrimid polymer matrix coated on IDEs show capacitive responses towards the detection of methanol at room temperature [14, 15]. Owing to its simplicity of fabrication, compatibility with the complementary metal-oxide semiconductor (CMOS) process and availability of sensitive capacitance measurement systems, IDE capacitor transducers provide a reliable platform for sensing studies. Most studies with IDEs are done by measuring changes in capacitance at ambient temperature. A transducer with an IDE capacitor integrated with a micro-electromechanical system (MEMS) such as a microhotplate could enable the study of sensing performance as a function of temperature. The modeling of adsorption and desorption kinetics of gas analytes with temperature also enables development of temperature-modulated sensing operation. Using such a platform, the temperature-dependent capacitive sensing towards detection of methanol with ZIF-8 MOF as the sensing layer is studied in this paper. A MEMS microhotplate integrated with parallel plate electrode has been used for on-chip curing of polyimide films at 350 °C [16]. In this device, polyimide films were placed in between chromium electrodes forming a parallel plate and integrated with a microhotplate underneath the electrodes. The device was used for temperature-dependent capacitance and dielectric measurements. However, materials placed within parallel plate electrodes do not allow reliable measurements of changes in capacitance with exposure to air and various gaseous analytes. Interdigitated electrode capacitor with polysilicon heaters were used for the analysis of recovery and thermal reset of polyimide sensing film during humidity measurements [17, 18]. A chemi-capacitive sensor with integrated molybdenum heater has been used for the study as CO_2 sensor [19]. The power consumption of this heater was in the range of 237 mW at 75 °C, which is high for continuous operation of portable battery powered electronic devices [19, 20]. Thus, the development of IDE capacitor transducers with a low-power, integrated microhotplate would be a suitable device for in situ, temperature-dependent gas sensing measurements. In comparison with conductometric MEMS microhotplate platforms, the development of IDE capacitor with integrated microhotplate have challenges since capacitance measurements are sensitive to temperature, frequency, and parasitic capacitances variations. The changes in the isolation layer capacitance due to temperature also influences the overall measured capacitance. Hence, it is essential to consider the calibration factors due to isolation layer capacitance during temperature-dependent capacitance measurements.

3.2. Experimental
3.2.1. Device design

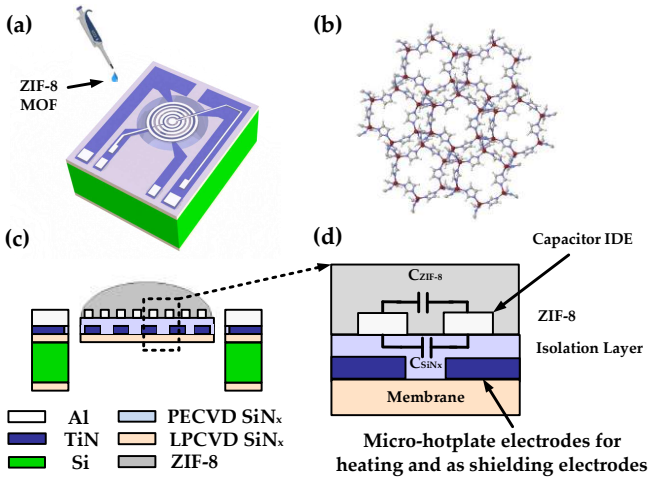

Figure 3.1: Device concept of ZIF-8 MOF coated MEMS IDE capacitor with integrated microhotplate: (**a**) Illustration of ZIF-8 MOF drop-casted on the final device. (**b**) 3D view of the crystal structure of ZIF-8 MOF with Zn, N, C and H described by red, purple, grey and white spheres respectively[21]. (**c**) Cross section of the device with deposited ZIF-8 MOF. (**d**) Description of equivalent electrical circuit of the IDE capacitor with microhotplate electrodes.

In this paper, a multilayered vertical stacked device structure is developed. The device concept and the cross-sectional view of the device is illustrated in Figure 3.1a,c, respectively. A circular microhotplate is fabricated on a thin dielectric membrane and forms the first metal layer. The IDE capacitor is fabricated above the circular microhotplate with an isolation layer between the two metal layers. The synthesized ZIF-8 MOF is deposited on the device by drop-casting as illustrated in Figure 3.1a. The capacitances obtained due to the thin film coating of ZIF-8 MOF on the device are, the isolation layer capacitance (C_{SiNx}) and the capacitance of ZIF-8 MOF layer (C_{ZIF-8}) (Figure 3.1d). The isolation layer is used to electrically insulate the two metal layers. However, the dielectric property of the isolation layer depends on both temperature and frequency of capacitance measurement. Thus, it is important to investigate the effects of the isolation layer capacitance (C_{SiNx}) at different temperatures on the total measured capacitance of the bare device. This would serve as a capacitance calibration factor during temperature-dependent capacitance measurements of ZIF-8 MOF-coated devices. In addition to the calibration factor, a good shielding mechanism needs to be designed close to the IDEs to negate the parasitic effects of the substrate capacitance, interconnects, and bond pads capacitance. One possible approach followed in this study is by using the underlying microhotplate electrodes as a shielding elec-

Table 3.1: Design parameters for fabrication of the devices.

Design Parameter	Value	Unit
Thickness of silicon nitride membrane	500	nm
Diameter of membrane	1	mm
Thickness of silicon nitride isolation layer	1	μm
Thickness of TiN electrodes	400	nm
Thickness of Al electrodes	1	μm
Width of IDE (W)	2	μm
Gap between IDE (G)	1	μm
Number of IDE pairs (N)	164	-

trode during capacitance measurement [22].

A microhotplate fabricated on a thin dielectric membrane with a temperature range up to 250 °C is desirable since the organic linker imidazole present in ZIF-8 MOF has a thermal stability up to 257 °C [23]. The key parameters considered in the design and fabrication of microhotplate are mainly temperature uniformity, power consumption and mechanical stability of the device [24]. Low-pressure chemical vapor deposited (LPCVD) silicon nitride (SiN_x) exhibits tensile stress preventing buckling of the membrane at higher temperatures, thus making it a suitable choice as a membrane material in comparison to compressive stress exhibited by silicon dioxide [25]. The temperature uniformity of the device is greatly improved by efficient design of the microhotplate geometry. Many studies have investigated temperature uniformity of various microhotplate geometry that includes meander, spiral, double spiral, drive wheel, and honeycomb [24]. However, design guidelines for improving the temperature uniformity has been mainly investigated by variation of the ratio of the widths of the metal lines of a circular microhotplate [26]. By modifying this design guideline to enable four-probe IV measurements, a circular microhotplate is designed. In comparison with metals such as platinum and molybdenum as heating metal, titanium nitride (TiN) is a CMOS compatible material and capability of dry etching of TiN electrodes allows a simpler fabrication processing steps. The resistivity of TiN shows a linear dependence on temperature in the range up to 600 °C [27]. Plasma enhanced chemical vapor deposited (PECVD) silicon dioxide and silicon nitride are considered for the isolation layer material. Silicon dioxide has compressive stress whereas silicon nitride used as membrane material exhibits tensile stress. To reduce the stress mismatch between the membrane and isolation layer, PECVD silicon nitride is used as the isolation layer material.

The design parameters used for the fabrication of the device are described in Table 3.5. Membranes with smaller diameter allow a reduction in power consumption but also decrease the area and the number of IDEs for capacitance measurement. To increase the measured base capacitance of the device with less influence from parasitic capacitances, a larger area for the circular IDE is required. Along with these considerations, the geometry parameters that

determine the capacitance of circular IDEs are the width of the electrodes (W), the gap between the electrodes (G) and the number of electrode pairs (N) [28]. The device dimensions were thus optimized to enable lower power consumption of the device and larger area for the capacitor electrodes. A circular LPCVD (SiN_x) membrane with a diameter of 1mm and thickness of 500nm supported by four beams is designed. A circular TiN microhotplate with a thickness of 400nm is deposited and patterned on the (SiN_x) membrane. Within the membrane dimensions, the number of circular IDE capacitor pairs (N) designed is 164. The optimized dimensions for the width of the capacitor IDEs within the process limitations are $W = 2$ μm and gap between the electrodes $G = 1$ μm.

3.2.2. Device fabrication

A double-sided polished 300μm thick 4 inch p-type <100> silicon wafer is used as the starting material (Figure 3.2a). A layer of low-stress LPCVD SiN_x of thickness 500nm is deposited both sides of the wafer using a Tempress LPCVD furnace. A 4μm thick PECVD silicon dioxide (SiO_2) is deposited and patterned on the back side of the wafer. This is used as a hard mask during back side deep reactive ion etching (DRIE). A 350nm thick Titanium nitride (TiN) metal layer with Titanium(Ti) of thickness 50nm as the adhesion layer is deposited by sputtering on the front-side of the wafer. The TiN heater design is etched by a plasma etching process using a Trikon Omega 201 plasma etcher (Figure 3.2c). In the next step, an isolation layer of 1μm of PECVD SiN_x is deposited on top of the TiN electrodes (Figure 3.2d). Next, a layer of aluminum (Al 1% Si) with a thickness of 1μm is sputtered on PECVD SiN_x. The electrodes are etched by plasma etching to form the IDEs (Figure 3.2e). This isolation layer electrically isolates the TiN heater electrodes and the aluminum (Al) IDE capacitor. Finally, DRIE of silicon is performed on the backside of the wafer to release the suspended membrane (Figure 3.2f).

3.2.3. Synthesis of ZIF-8 MOF

All chemicals were purchased from Sigma Aldrich and used as received. Typically, 734.4mg (2.469mmol) of $Zn(NO_3)_2$*$6H_2O$ and 810.6mg (9.874mmol) of 2-methylimidazole (Hmim) are each dissolved in 50mL of methanol (MeOH). The latter clear solution is poured into the former clear solution under stirring with a magnetic bar. Stirring is stopped after combining the component solutions. After 24 h, the solid is separated from the milky colloidal dispersion by centrifugation. Washing with fresh MeOH and centrifugation is repeated three times[29]. The product is dried at room temperature under reduced pressure. The synthesized ZIF-8 MOF is dispersed in ethanol and drop-casted on the devices using a 1μL pipette. The synthesized ZIF-8 MOF is dispersed in ethanol and ultrasonicated to obtain a uniform suspension of 4.5wt% ZIF-8 MOF in ethanol solution. The prepared solution is drop-casted on the devices using a 1μL pipette.

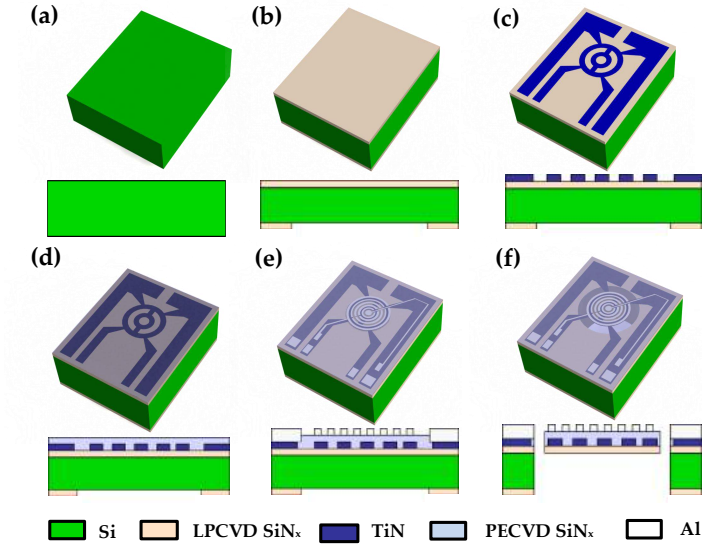

Figure 3.2: Fabrication process flowchart of the device (**a**) Silicon substrate. (**b**) 500nm low stress LPCVD silicon nitride. (**c**) Patterned 400nm Ti/TiN microhotplate on the front side of the wafer. (**d**) 1μm PECVD silicon nitride isolation layer on top of the microhotplate. (**e**) Patterned 1μm Al/1% Si IDEs. (**f**) DRIE etching of Si to obtain a suspended membrane.

3.2.4. Structural characterization

Scanning Electron Microscopy (SEM) were acquired at different magnification using JEOL JSM 6010LA and Philips XL50. SEM chapter-3 were acquired after sputtering with gold layer for a device coated with ZIF-8 MOF using JEOL JFC-1300 auto fine coater with current setting at 20mA for 120s. X-Ray Diffraction (XRD) of as-synthesized ZIF-8 MOF were recorded using Bruker D8 Advance diffractometer with Co-K radiation ($\lambda = 1.788897$ Å). A step size of 0.02° with a scan speed of 0.2s per step was used to acquire the diffraction pattern. The measurement of the thickness of the deposited ZIF-8 MOF on the devices was done using Keyance laser profilometer. Optical images were acquired with SENTECH STC-6255C-CM camera connected to a Cascade microtech probe station.

3.2.5. Experimental setup and measurement procedure

A thermochuck temperature controller, connected to a Cascade Microtech wafer probe station and Agilent 4156C parameter analyzer, was used for the electrical characterization of the TiN microhotplates at different temperatures (Figure 3.3a). In this experiment, the temperature of the chuck was increased to eight temperatures steps in the range from 20°C to 200°C. A small current of 50μA was supplied through the TiN microhotplate (to avoid self-heating of

the microhotplate), and the voltage drop across the microhotplate was measured using an Agilent 4156C parameter analyzer at each temperature steps. The temperature coefficient of resistance (TCR) of the devices were extracted by this measurement. This calibration data allows monitoring of the average temperature of the devices during device operation.

The steady-state power consumption of the devices before and after deposition of ZIF-8 MOF was measured in vacuum and nitrogen. This was done to understand the thermal performance of the devices under different conditions. The device was wire-bonded and packaged in a 40 pin dual-inline package. The packaged device was sealed in a closed metal chamber with an electrical feedthrough and placed in an oven. A schematic of the experimental setup for the measurement of the devices is conceptually illustrated in Figure 3.3b. A Keithley 2611B source measurement unit (SMU) was used for controlling the current flow through the microhotplate. The voltage across the microhotplate was measured, and thereby the resistance and corresponding operating temperature were determined. The chamber was connected to a vacuum pump, enabling a low-pressure control down to 1 mbar. A current sweep from 0.2mA up to 5mA was used to characterize the heater performance in vacuum (1 mbar), while a current sweep from 0.2mA up to 8mA was used for nitrogen (1 bar) environment.

The capacitance measurement of the device is very sensitive to parasitic capacitances due to the connections. Thus, a good shielding between the devices, HP4284A LCR meter, and Keithley SMU must be made. The connections to the LCR meter and Keithley uses SMA connectors which were shielded to the system ground. The outer conductors of the coaxial cables are shielded to the system ground to avoid measurement errors due to interference. The TiN microhotplate device below the IDE capacitor provides a shielding mechanism during measurement of the capacitance. The DC ground of the microhotplate was coupled to the ground shielding of the LCR meter for shielding the IDE capacitor (Figure 3.3b). The capacitance characterization of the bare device was done in vacuum at different operating temperatures using the microhotplate. The current flow through the microhotplate was controlled using the Keithley 2611B for operating the microhotplate at the desired temperature. The capacitance was simultaneously measured using an HP4284A LCR meter at a constant frequency of 10kHz and voltage of 1V.

Sensing experiments of the packaged ZIF-8 MOF coated device with vapors of methanol and water was done in a chamber as described in Figure 3.3b. Before the measurements, dry nitrogen at a flow rate of 200mL/min was introduced until a stable baseline was obtained. The vapors of water and methanol were generated through a series of two bubblers to attain a saturated stream of the analyte as described in our previous works[14]. The vapors were then diluted with a parallel stream of dry nitrogen and passed over the packaged device in the chamber at a constant flow rate of 200mL/min. The corresponding changes in the capacitance for exposure to different concentration was measured with the HP4284A LCR meter at a frequency of 10kHz and oscillation

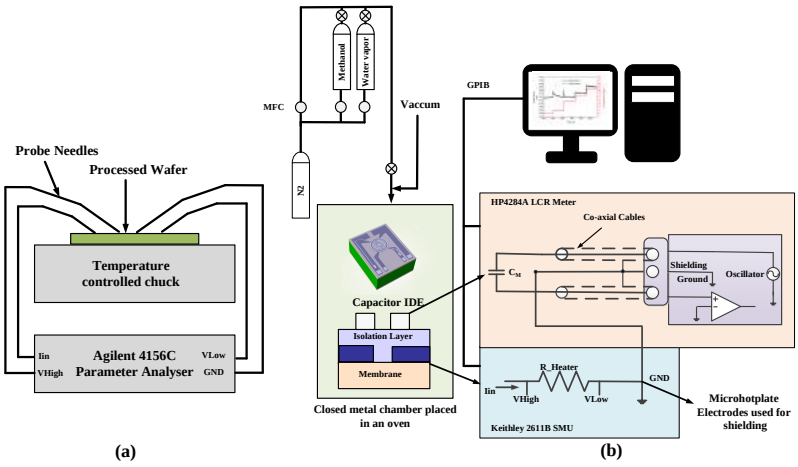

Figure 3.3: (**a**) Electrical characterization of the microhotplate. (**b**) Schematic representation of the gas sensing measurement setup.

voltage of 1V. Using the integrated microhotplate enabling *in-situ* heating, the temperature-dependent sensing response of ZIF-8 MOF was obtained for methanol and water vapor.

3.3. Results and Discussion

3.3.1. Device and material characterization

The synthesized MOF was examined for morphology and crystallinity by SEM and XRD. The rhombic dodecahedral crystals and the diffraction pattern of the obtained MOF showed similarity with ZIF-8 as indicated by the theoretically simulated pattern of ZIF-8 (Supplementary Information, Figure S3.1a and S3.1b), and as reported by literature[30][31]. It clearly demonstrated that the synthesis of ZIF-8 was successful, and was then further used for deposition over the active area of the devices. The device having a dimension of 10mmx2.5mm with the active area at the top and contact pads at the bottom is shown in Figure 3.4a. The bare device with patterned circular aluminum IDEs having a width(W) of 2μm and gap(G) of 1μm above the TiN microhotplate (darker electrodes) is shown in Figure 3.4c. The as-synthesized ZIF-8 MOF is deposited on the device area. Figure 3.4d and 3.4e shows that the IDEs is completely covered with ZIF-8 MOF. The thickness of ZIF-8 drop-casted on the devices was measured along the diagonal profile of the device as shown in Supplementary Information, Figure S3.2. The thickness obtained was larger than 3 μm and the average thickness is 20μm. It is seen that due to drying effects, there is slightly less coating at the centre of the device. In the current design of the IDE capacitor, the width(W)= 2μm and gap(G) = 1μm, so the spatial wavelength (λ) = 6μm. The thickness of the affinity layer should be

greater than half the spatial wavelength (>0.5 * λ)[32]. The obtained thickness of the coating was about 6-10 times the half spatial wavelength (0.5 * λ), verifying that the thickness of the affinity layer is large enough to completely enclose the electrical field lines. In such case, no performance change in the equilibrium/static response will be observed [14][32]. The response will only be affected with respect to diffusion of molecules to sensitive region of the device. However, the density of the film might change with thickness, because drop casting does not control the density/void spaces of the deposited layer. The stability of density/void spaces of the deposited film on the device was further verified by characterizing the sensor to the analyte for several days.

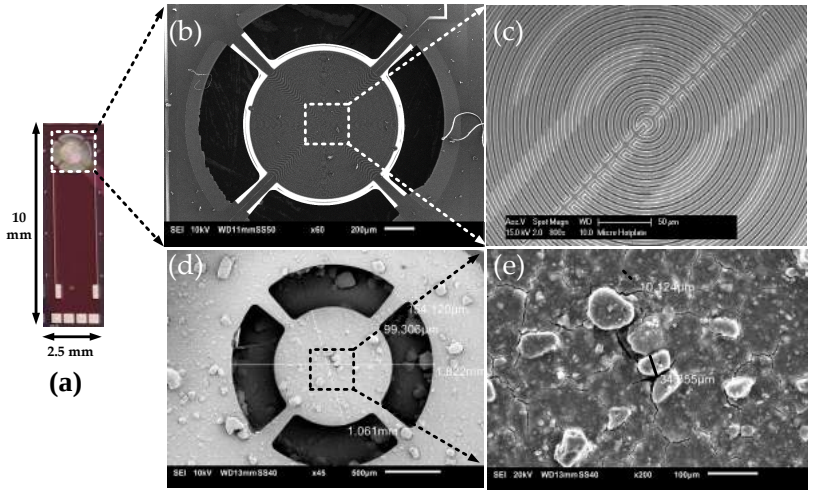

Figure 3.4: (**a**) Fabricated device. (**b**) SEM image of the suspended microhotplate with capacitor IDE. (**c**) A close-up image showing the active area of the device. (**d**) ZIF-8 MOF coated device (**e**) A close-up image of ZIF-8 MOF on top of the electrodes.

The device having a dimension of 10mmx2.5mm with the active area at the top and contact pads at the bottom is shown in Figure 3.4a. The bare device with patterned circular aluminum IDEs having a width of 2mm and gap of 1mm above TiN microhotplate (darker electrodes) is shown in Figure 3.4c. The as-synthesized ZIF-8 MOF is deposited on the device area. Figure 3.4d and 3.4e shows that the IDEs is completely covered with ZIF-8 MOF.

3.3.2. Thermal Characterization

In this section, the temperature coefficient of resistance (TCR) of the fabricated TiN microhotplate device is extracted. The steady-state power consumption of the bare device and the device coated with ZIF-8 MOF in nitrogen and vacuum is measured and compared. Next, thermal modeling using Finite Element Method (FEM) is done to analyze the temperature distribution across the ZIF-8 coated device.

The measured resistance of the TiN microhotplate as a function of temperature for five devices is shown in Figure 3.5a. The average resistance at 20°C is 500Ω. The TCR (α) of the heater is extracted by the below equation,

$$R(T) = R_0 \cdot (1 + \alpha \cdot (T - T_0)) \tag{3.1}$$

where R_0 is the resistance at room temperature and $R(T)$ is the resistance at temperature T. From the Figure 3.5a, it is seen that due to process variation, there is a slight difference in the values of R_0 of the samples. However the slope, and thus the TCR, of the microhotplate is nearly constant. The average TCR of five devices is 0.000717/°C. The thermal characterization of bare device in vaccum and nitrogen, and heat losses in the device is analyzed in Section 3.5.3, Supplementary Information.

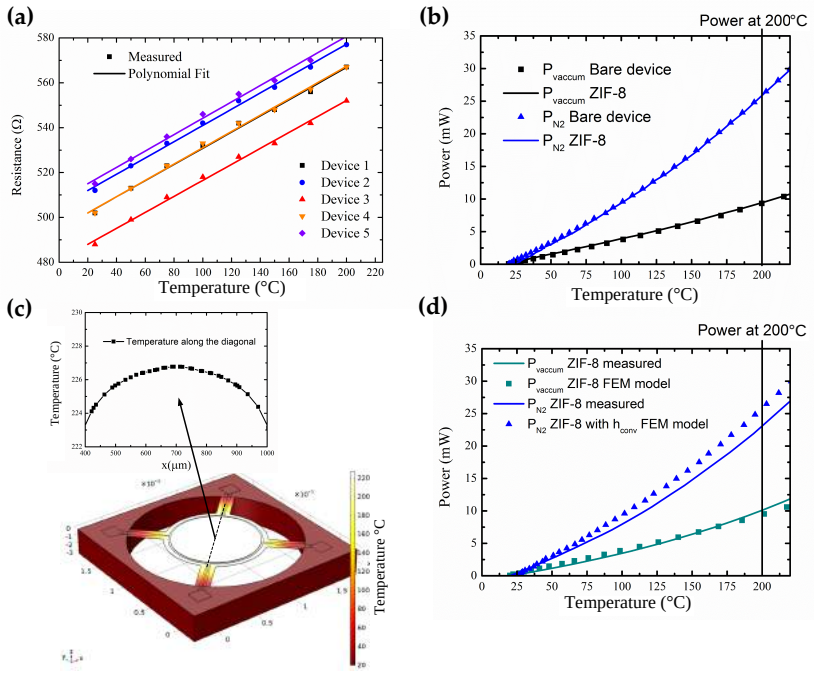

Figure 3.5: (**a**) Power consumption in bare device. (**b**) Comparison between power consumption in bare device and ZIF-8 coated device in vacuum and nitrogen.(**c**) FEM thermal analysis of ZIF-8 coated device. (**d**) Comparison between power consumption of ZIF-8 coated device and FEM results.

The steady-state power consumption of the device coated with ZIF-8 MOF and the bare device is shown in Figure 3.5b. The input power required to attain an operating temperature of 200°C with ZIF-8 coated device is 26mW in comparison to the bare device which is 25.8mW (Supplementary Information, Figure S3.4). The small increase in input power for ZIF-8 MOF coated device

could be due to the extra MOF coated on the suspension, which decreases the thermal resistance slightly for heat loss due to conduction. The achieved power consumption for the device coated with ZIF-8 MOF at 200°C is much lower than the reported IDE capacitor transducer with integrated microhotplate as shown in Table 3.6.

To further analyze the temperature uniformity across the device, a FEM model of the device with joule heating module is developed in COMSOL Multiphysics® 5.3 (Section 3.5.3, Supplementary Information). The extracted convection coefficient for the device in nitrogen (h_{conv}), TCR of the TiN microhotplate (α) obtained from the above measurements are used in the joule heating module of the multiphysics model. The temperature uniformity obtained from FEM analysis across the active region of the membrane coated with ZIF-8 MOF is +/- 4 °C (Figure 3.5c). The comparison between the steady-state power consumption of the FEM model and measured results with ZIF-8 MOF is shown in Figure 3.5d. The observed difference between power consumption versus temperature of simulated and measured results at a temperature of 200°C is found to be 7% in vacuum, and in nitrogen it is 11%. This shows that the FEM thermal modeling follows closely to expected measurement results. The observed difference can be attributed to the deviations in the reference thermal conductivity values of the materials and non-ideal extraction of the convection coefficient[33].

Table 3.2: Comparison of power consumption and operating temperature of MEMS capacitor sensors with integrated microhotplate.

Device Temperature (°C)	Power (mW)	Material	Reference
75	237	3-AMO[1]and 30% PTMS[2]	[19]
60	300	Similar as [19]	[34]
50	37	Polyimide	[17]
46	155	Polyimide	[35]
200	26	ZIF-8	This Work

[1] aminopropyltrimethoxysiloxane(AMO)
[2] propyltrimethoxysilane(PTMS)

With the capability of *in-situ* heating, thermal stability tests of ZIF-8 MOF were done at various temperatures to observe the physical changes in ZIF-8 MOF. The surface morphology of ZIF-8 MOF at 50°C and 100°C is shown in Supplementary Information, Figure S5b and S5c respectively. The degradation of ZIF-8 MOF film is not observed optically at these low temperatures. The changes in the morphology and distribution of the ZIF-8 thin film are clearly visible on heating from 20°C to 300°C as shown in Supplementary Information, Figure S3.5. This shows the thermal limitation of ZIF-8 MOF which coincides with the reported TGA experiments[36].

3.3.3. Sensing measurements

The impedance characterization of both the bare device and ZIF-8 coated device were done in the frequency range from 1kHz to 100kHz. It is seen

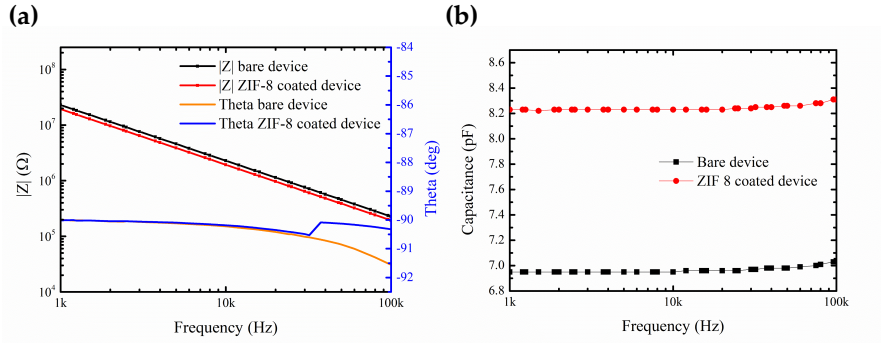

Figure 3.6: (**a**) Impedance and Theta versus frequency. **b**) Comparison between capacitance of bare and ZIF-8 coated device versus frequency.

that the deposition of ZIF-8 MOF on the devices causes a decrease in the overall impedance measured and increase in the capacitance as shown in Figure 3.6a and Figure 3.6b. The values of theta of the devices lie within a small range around -90° for frequencies of 1kHz-100Khz (Figure 3.6a), indicating the capacitive nature of the devices. In more detail, this indicates that the addition of ZIF-8 thin film MOF on top of the IDE still shows capacitive behaviour similar to previous studies of ZIF-8 MOF grown on top of silicon substrate[9]. A stable capacitance response is seen in the frequency range from 1kHz to 100kHz (Figure 3.6b).

The device coated with ZIF-8 MOF was exposed to increasing concentration of methanol from 500ppm to 7000ppm in dry nitrogen. The resulting changes in capacitance was measured at an oscillation voltage of 1V and a frequency of 10kHz. Methanol, having a kinetic diameter of 3.4 Å, and a dielectric constant of ($\epsilon_r = 32.7$) is able to enter and condense within the flexible porous structure of ZIF-8 MOF having a pore diameter of 3.8 Å[9]. The adsorption of methanol in ZIF-8 MOF increases the effective dielectric constant resulting in the increase in the measured capacitance. The observed changes in the measured capacitance are in low fF ranges(60fF). A baseline drift was observed during the sensing study (Supplementary Information, Figure 3.6). The baseline drift was calibrated, and the resulting change in capacitance (ΔC) for increasing concentration of methanol is shown in Figure 3.7a. The capacitance of the device (ΔC) changes from 9-60fF for methanol concentration in the range from 500-7000 ppm (Figure 3.7b). The changes in the measured capacitance (ΔC) in ZIF-8 MOF for increasing methanol concentration is fitted with Langmuir adsorption isotherm model given by[14],

$$\frac{\Delta C}{C_s} = \frac{K_e C_m}{1 + K_e C_m} \tag{3.2}$$

where, C_s is the saturation value of the capacitance, K_e is the affinity constant and C_m is the concentration of methanol. The obtained values for K_e

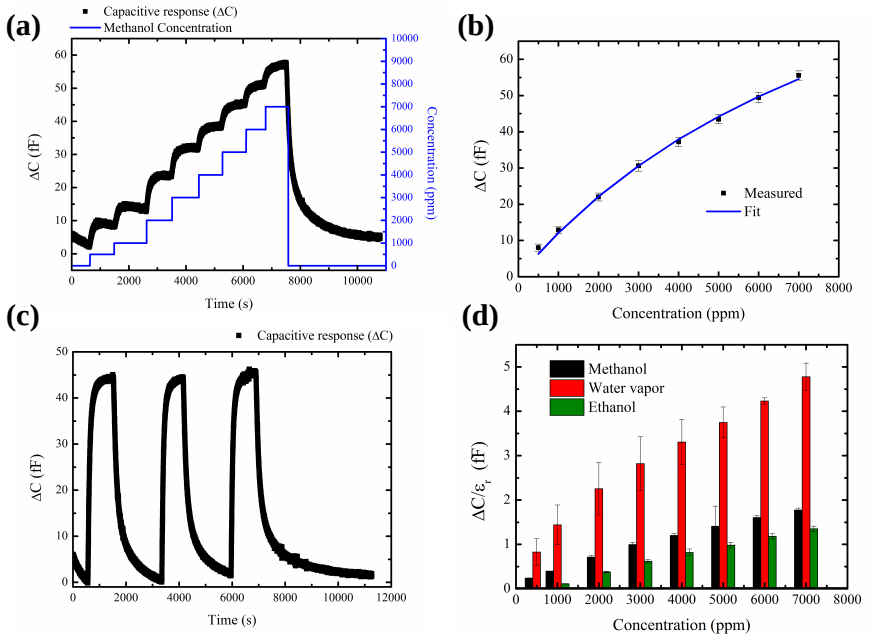

Figure 3.7: (**a**) Sensing response for methanol concentration from 500ppm to 7000ppm. (**b**)Langmuir isotherm fit.(**c**) Response to 5000ppm of methanol. (**d**) Comparison between methanol, ethanol and water vapor normalized with the dielectric constant.

and C_s are 101 bar^{-1} and 131.7fF, respectively. The saturation value of the capacitance (C_s) is obtained at much higher methanol concentration indicating a higher capability of adsorption of methanol in the porous framework of ZIF-8 MOF[37]. The calculation of the minimum detection of the capacitance using the current system is done by considering the baseline variation of capacitance in nitrogen as shown in Figure S3.7, Supplementary information. The standard deviation σ is 0.3fF. Considering 3σ value, the minimum detectable capacitance change on exposure to methanol for this device is about 1fF. The detection limit of the sensor for methanol with a capacitance change of 1fF is 100ppm. The obtained sensing performance can be further improved by 1000 fold using sensitive capacitive read-out system with lock-in principle for aF-level capacitance detection[38]. However, development of sensitive capacitance read out system was not the focus of our study. A comparison of various methanol sensor in literature over a wide concentration range with sensing materials such as, metal-oxide/metal-oxide composites, MOFs and epoxy acrylate polymer film is shown in Table 3.7. In metal-oxide/metal-oxide composites sensing materials, methanol vapor mainly reacts with the chemisorbed oxygen on the surface of the film at high temperature (150°C - 350°C), thus requiring higher power during sensor operation. However, sensing materials such as CuBTC MOF, NH_2-MIL-53(Al) MOF in Matrimid polymer

and Epoxy acrylate film show methanol sensing response at near room temperature. In comparison with these sensing materials, the sensitive detection of methanol obtained at 20°C with ZIF-8 MOF as affinity layer further enables the development of miniaturized low-power sensors.

The reversibility behaviour of methanol at a concentration of 5000ppm after baseline drift correction (Supplementary Information, Figure S3.8a and S3.8b) is shown in Figure 3.7c. It can be seen that methanol adsorbed by ZIF-8 is completely reversible in dry nitrogen. Next, a comparative study for increasing concentration of methanol, ethanol and water vapor from 500ppm to 7000ppm is performed. The obtained capacitance response (ΔC) is corrected with the dielectric constant ($\Delta C/\epsilon_r$) for water ($\epsilon_r = 78$), methanol ($\epsilon_r = 32.7$) and ethanol ($\epsilon_r = 24.2$) as shown in Figure 3.7d. The response to ethanol is found to be less than methanol. This is due to both concentration taken up in the ZIF-8 film, and the contribution to the change of dielectric constant. Ethanol having a lower dielectric constant than methanol thus contributing to lower signal strength. The measured response ($\Delta C/\epsilon_r$) to water vapor is found to be higher than the response towards methanol in the concentration range from 500ppm to 7000ppm. Water molecules with a higher dielectric constant ($\epsilon_r = 78$) and kinetic diameter of 2.8 Å, can enter and condense in the porous framework of ZIF-8 MOF[9], resulting in higher changes in the measured capacitance.

Table 3.3: Comparison of the developed ZIF-8 MOF methanol sensor and methanol sensors in literature.

Sensing Material and Reference	Operating Temperature (°C)	Concentration range (ppm)	Detection limit (ppm)
CuBTC-MOF[39]	25	250-1500	62
NH_2-MIL-53(Al) MOF in Matrimid[14]	28	1000-8000	-
ZnO hexagonal nanorods[40]	150- 250°C	190-3040	-
CdS-doped tin oxide[41]	200	70-5000	-
Copper (II) oxide[42]	350	100-2500	-
MoS_2 nanoflakes[43]	200	200-400	-
Epoxy acrylate film[44]	room temperature	200-16000	-
ZIF-8 MOF(This work)	20	500-7000	100

3.3.4. Temperature-dependent adsorption and desorption kinetics

The device coated with ZIF-8 MOF was operated at a constant temperature by the TiN microhotplate at 20°C, 30 °C, 40°C and 50°C. The resulting change in capacitance (ΔC) for a constant concentration of 5000ppm of methanol and water vapor was measured.

The data analysis procedure for the measured response is described in Figure 3.8a and the below equation,

$$\Delta C(t) = C_{measured}(t) - \Delta C_{SiN_x} - C_{baseline}(t) \tag{3.3}$$

The measured capacitance response ($C_{measured}(t)$) is first calibrated with temperature-dependent isolation layer. The calibration curve obtained for ΔC_{SiN_x} versus temperature is explained in detail in Section 3.5.6, Supplementary Information. Next, a baseline drift calibration $C_{baseline}(t)$ is done for both

methanol (Section 3.5.7, Supplementary Information, Figure S3.18a - S3.18i) and water vapor (Section 3.5.7, Supplementary Information, Figure S3.19a - S3.19i). The final response $\Delta C(t)$ for different operating temperatures from 20°C to 50°C for methanol and water vapor is shown in Figure 3.8b and 3.8c respectively.

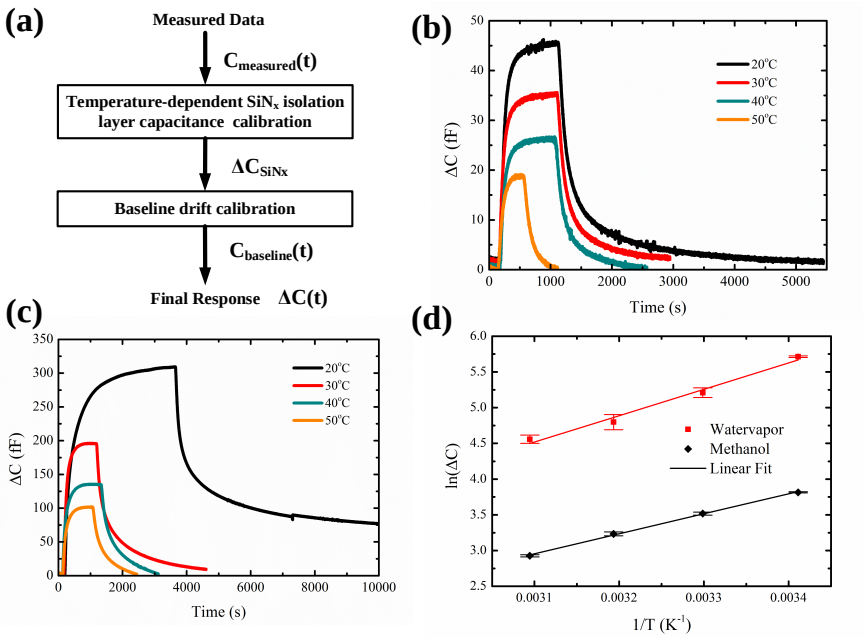

Figure 3.8: (**a**) Data analysis procedure. Capacitance response at different temperatures for 5000ppm of (**b**) Methanol (**c**) Water vapor **d**) Arrhenius relation between capacitance and temperature.

The change in capacitance (ΔC) for both methanol (Figure 3.8b) and water vapor (Figure 3.8c) decreases with the increase in temperature. At a temperature of 20°C the saturation value of the change in capacitance ΔC is 45fF, whereas at 50°C the saturation value of ΔC decreases to 18fF. In the case of water vapor, a similar decrease in the saturation value of capacitance is observed at increased temperatures. The saturation value of ΔC obtained at 20°C is 300fF and it reduces to 100fF at 50°C. These results indicate that the amount of analyte adsorbed by ZIF-8 MOF decreases with increasing temperatures. The adsorption process is further studied by determining the enthalpy of adsorption. An Arrhenius plot of the change in capacitance versus temperature is shown in Figure 3.8d. This behavior is described by the following equation[14],

$$\Delta C = C_{max} e^{\frac{-\Delta H}{RT}} \tag{3.4}$$

where, C_{max} represents the equilibrium capacitance, *(*ΔH*)* is the difference in the activation energy of the adsorption and desorption process.

The calculated values of enthalpy of adsorption *(*ΔH*)* is -23kJ/mol for methanol and for water vapor is -30kJ/mol. The negative value obtained for ΔH indicates the exothermic nature of the adsorption process. The slight higher enthalpy of adsorption for water vapor observed at low water uptake is due to the structural defects present in the ZIF-8 MOF that increases the interaction energy with water vapor molecules[45]. The sensing measurements were performed for several weeks for testing the long term stability of ZIF-8 MOF. The response to 5000ppm of methanol at 20°C in a three week period is shown in Figure S3.20, Supplementary information. The observed changes in delta C is less than 3fF. The measured response to methanol concentration of 5000ppm at different temperature done once every week for three weeks, (Supplementary information, Figure S3.21) show good stability of the ZIF-8 MOF with temperature upto 50°C. These measurement also indicate that the density of the deposited film by drop-casting process on the device does not change over a period of time.

Based on the capacitance response and recovery curves at different temperatures, the time-dependent adsorption and desorption kinetics can be derived. The measured capacitance at 20°C and 50°C normalized to the equilibrium capacitance ($(\Delta C)/C_{max}$) for adsorption and desorption of methanol is given in Figure 3.9a and 3.9b respectively. The Langmuir adsorption and desorption kinetics of gases in MOFs and porous materials are described using Double Exponential Models (DEP) in various studies[46][47][48]. In this model, adsorption is based on a two-stage process due to the energetic barriers during diffusion of vapor molecules in MOFs. The first energetic barrier is due to the diffusion through the windows of the porous framework and the second barrier is diffusion along the pore cavities. With increasing temperature, the rate of adsorption of methanol to attain equilibrium capacitance increases (Figure 3.9a).

The DEP curve fitting model is given by the following equation,

$$\frac{M_t}{M_s} = A_{1a}(1 - e^{-k_1}) + A_{2a}(1 - e^{-k_2}) \tag{3.5}$$

where, M_t represents the mass uptake at time t, M_s is the mass uptake at equilibrium, k_1 and k_2 represents the kinetic rate constants and A_{1a} and A_{2a} are the relative contribution of the two energetic barriers during the adsorption process.

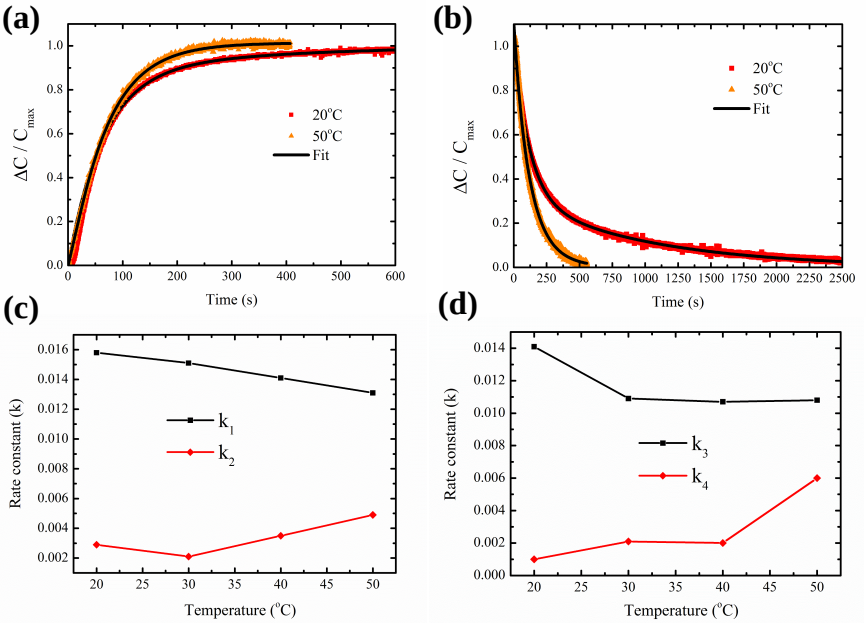

Figure 3.9: Time-dependent capacitance response at 20°C (red) and 50°C (orange) with Langmuir-based double exponential fitting (black) for (**a**) adsorption of methanol and (**b**) desorption of methanol. Kinetic parameters versus temperature (**c**) adsorption of methanol. (**d**) desorption of methanol.

In Figure 3.9b, a higher rate of desorption of methanol is observed at higher temperatures. The desorption process can also be modelled as a two-stage process with a fast exponential decay in the first stage followed by slow decay in the second stage. The modelling equation is given by,

$$\frac{M_d}{M_o} = A_{1d}(e^{-k_3}) + A_{2d}(e^{-k_4}) \tag{3.6}$$

where, M_d represents the mass desorbed at time t, M_o is the initial mass adsorbed at equilibrium, k_3 and k_4 are the kinetic desorption rate constants and A_{1d} and A_{2d} are the relative contribution of the rate constants during the desorption process.

In ZIF-8 MOF, the capacitive sensing response towards methanol follows Langmuir adsorption isotherm behaviour. Thus, the time-dependent adsorption and desorption process described in Equation 3.5 and Equation 3.6 can be further related to the time-dependent capacitance changes during sensing and recovery measurement. The capacitance response kinetics for the adsorption (Equation 3.7) and desorption process (Equation 3.8) are described below,

$$\frac{\Delta C}{C_{max}} = A_{1a}(1 - e^{-k_1}) + A_{2a}(1 - e^{-k_2}) \tag{3.7}$$

$$\frac{\Delta C}{C_{max}} = A_{1d}(e^{-k_3}) + A_{2d}(e^{-k_4}) \tag{3.8}$$

The regression coefficients for the curve fitting of DEP models for sensing and recovery curves at different temperatures are $R^2 > 99\%$ (Section 3.5.9, Supplementary Information). The time-dependent adsorption and desorption kinetic parameters for different temperatures are tabulated in Table 3.8. Based on the sensing and recovery curves, the response time and recovery time is calculated for different temperatures. The response time (t^+) is defined as the time taken to reach 90% of the equilibrium capacitance value (C_{max}) and the recovery time (t^-) is defined as the time taken to reach 10% of the equilibrium capacitance value. The values for the response time and recovery time for different temperatures is given in Table 3.8. It can be seen that during the adsorption process the obtained kinetic rate constants k_1 is greater k_2. Upon increasing temperatures, the rate constant k_1 decreases whereas k_2 slightly increases. The overall response time decreases with the increase in temperatures. At a temperature of 20°C the response time is 207s, whereas at 50°C the response time decreases to 147s. During the desorption process, it is seen that the kinetic parameter k_3 shows a decrease with increasing temperatures whereas k_4 increases with temperature. The recovery time decreased at higher temperatures, at 20°C the recovery time is 981s, at 50°C the recovery time obtained is 298s. With the increase in temperature, changes in the pore structure of the ZIF-8 MOF can occur influencing the diffusivity of gases within the porous structure of ZIF-8 MOF[49]. These structural changes could lead to the observed overall decrease in both response and recovery time as the temperature increases.

Table 3.4: Table of kinetic parameters and response/recovery time for Methanol.

Temperature	**Kinetic parameters**					
	Adsorption		**Desorption**		**Response Time**	**Recovery Time**
(°C)	$\mathbf{k_1}$	$\mathbf{k_2}$	$\mathbf{k_3}$	$\mathbf{k_4}$	$\mathbf{t^+}$(s)	$\mathbf{t^-}$(s)
20	0.0158	0.0029	0.0141	0.0010	207	981
30	0.0151	0.0021	0.0109	0.0021	198	633
40	0.0141	0.0035	0.0107	0.0020	181	585
50	0.0131	0.0049	0.0108	0.0060	147	298

Next, a comparison between the time-dependent methanol and water vapor adsorption and desorption at 20°C for a constant concentration of 5000ppm of the analyte is shown in Figure 3.10. It can be seen that methanol has a higher rate of adsorption and desorption in ZIF-8 MOF in comparison to water vapor. The response time obtained for methanol and water vapor at 20°C is 207s and 913s respectively. The recovery time obtained for methanol is 981s at 20°C and for water vapor the recovery time is more than 3000s. This shows that ZIF-8 MOF is kinetically selective for the adsorption of methanol than water vapor.

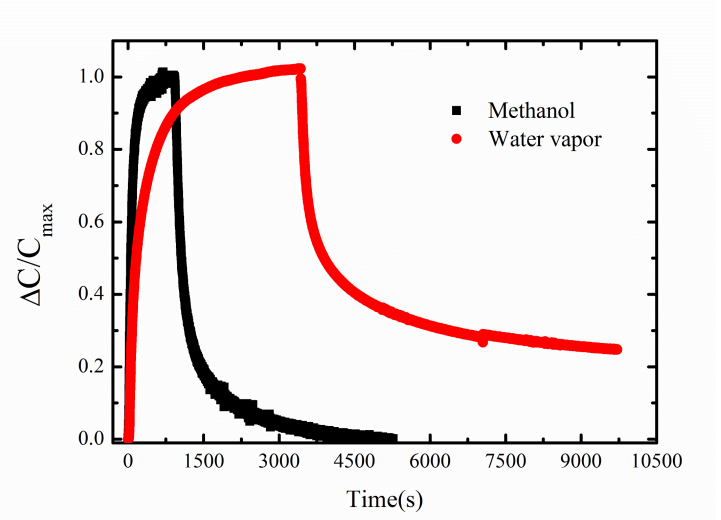

Figure 3.10: Methanol and water vapor sensing and recovery curves at 5000ppm at 20°C.

3.4. Conclusions

In this paper, we report a successful demonstration of ZIF-8 MOF capacitive sensor with integrated TiN microhotplate. The sensor shows changes in capacitance on exposure to methanol from 500ppm-7000ppm, having a capability for the detection of 100ppm of methanol vapor at temperature of 20°C. Cross-sensitivity study with exposure to water vapor in the concentration from 500ppm-7000ppm shows that water vapor has a higher capacitance response. However, at a temperature of 20°C it is seen that the adsorption of methanol is faster than water vapor for a constant concentration of 5000ppm. The changes in the morphology of ZIF-8 MOF was investigated by *in-situ* heating from 20°C to 300°C using the TiN microhotplate. A systematic experiment methodology was followed in this paper with careful consideration of the capacitance changes with temperature due to the PECVD silicon nitride isolation layer on the overall measured capacitance. The change in the capacitance of the bare device was found to be linear with temperature, and it is used as a calibration factor during sensing study with temperature. *In-situ* heating using integrated microhotplate enabled to study the kinetics of adsorption and desorption of methanol with temperatures from 20°C to 50°C . The temperature-dependent kinetic rate constants for both adsorption and desorption of methanol were derived. With increasing temperature from 20°C to 50°C, the response time decreased from 207s to 147s. A similar decrease in the recovery time was obtained from 981s to 298s at 20°C and 50°C, respectively. The ability for fast temperature cycle times using the microhotplate allows for the determination of the optimized temperature and reset time of the ZIF-8 MOF coated devices

during capacitive vapor sensing measurements. An array of such developed devices also allows the possible solution to combine different type of MOFs as affinity layer with different selectivity. This is an essential step towards a multi-sensing platform.

3.5. Supplementary Information

3.5.1. Structural characterization of ZIF-8 MOF

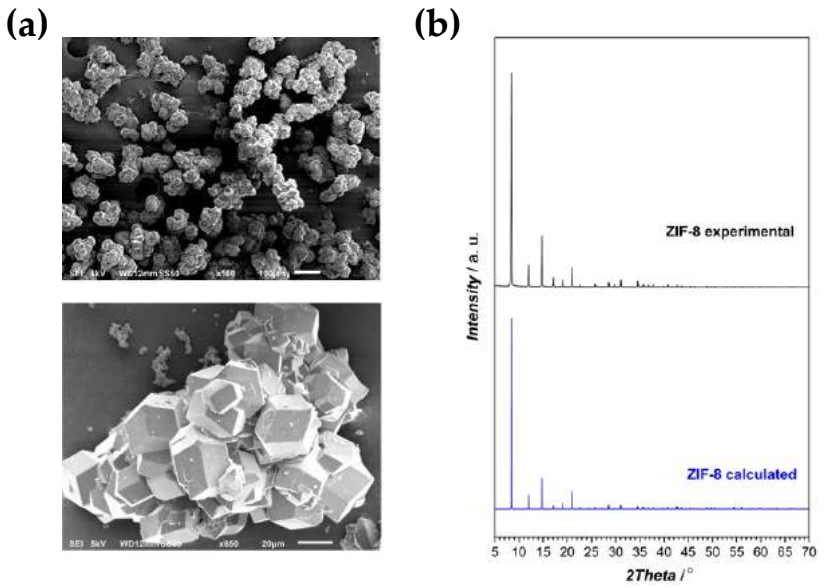

Figure S 3.1: (**a**) SEM image of as-synthesized ZIF-8 at different magnifications. (**b**) Measured and simulated XRD plots.

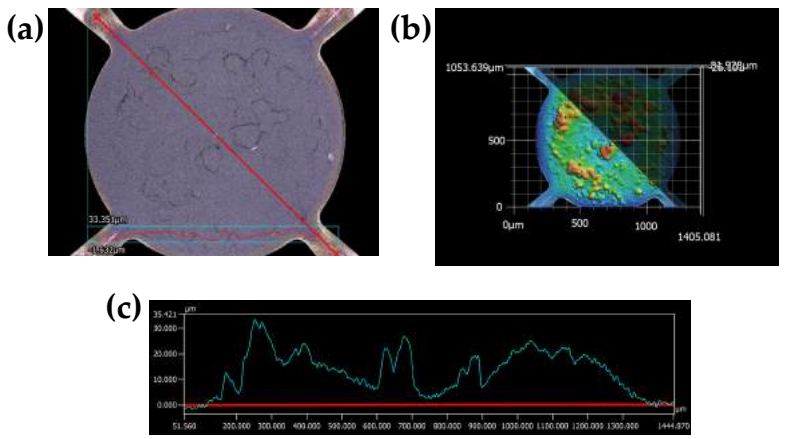

Figure S 3.2: Laser profilometer data plot of ZIF-8 MOF coated device. (**a**) Measured region. (**a**) 3D map of the ZIF-8 MOF coating. (**c**) Layer thickness profile.

3.5.2. Thickness measurements of ZIF-8 MOF coated device

Keyance Laser profilometer was used and the resulting thickness measurements along the diagonal of the device is shown in Figure S 3.2.

3.5.3. Thermal characterization of the micro-hotplate and analysis using FEM

The steady-state power consumption of the bare device in nitrogen (P_{N_2}) and in vacuum (P_{vacuum}) is shown in Figure S 3.3. The heat loss by different means of heat transfer of the bare device is estimated as following[50][51],

- The radiative power loss is theoretically calculated for the top and bottom area of the device using Stefan-Boltzmann law given by,

$$P_{rad}(T_h) = 2 * \epsilon\sigma A_h((T_h^4 - T_0^4)) \tag{3.9}$$

  where ϵ is the effective emissivity of the microhotplate taken as 1[50], σ is the Stefan-Boltzmann constant given as $56.7 \cdot 10^{-9}$ $Wm^{-2}K^{-2}$, A_h is the area of the microhotplate calculated to be $5.25 \cdot 10^{-7}$ m^2 , T_h is the average temperature of the heater at a given input power and T_0 is the ambient temperature. The calculated radiative heat loss $P_{rad}(T_h)$ is shown in Figure S 3.3. At a temperature of 200°C, $P_{rad}(T_h)$ is 2.5mW.

- The conductive power loss through the membrane and beams of the microhotplate is determined by subtracting the radiative power loss from the power consumption of the bare device in vacuum given by,

$$P_{cond}(T_h) = P_{vacuum}(T_h) - P_{rad}(T_h) \tag{3.10}$$

  At a temperature of 200°C the obtained conductive power loss $P_{cond}(T)$ is 6.8mW.

- The convective power loss $P_{conv}(T_h)$ (Figure S 3.3) due to nitrogen flow is obtained by subtracting the power consumption of the device in nitrogen with power consumption in vacuum given by ,

$$P_{conv}(T_h) = P_{N_2}(T_h) - P_{vacuum}(T_h) \tag{3.11}$$

  The obtained convective power loss $P_{conv}(T_h)$ at 200°C is 16.5mW. Considering the convective power $P_{conv}(T_h)$, the convection coefficient $h_{conv}(T_h)$ is extracted using the following equation[50],

$$h_{conv}(T_h) = \frac{P_{conv}(T_h)}{A_h(T_h - T_0)} \tag{3.12}$$

For the bare device an input power of 3.5mW and 25.8mW is required to obtain a temperature of 50°C and 200°C in nitrogen respectively. The obtained power loss due to convection is 64%, 26% due to conduction and 10% is due to radiation. Hence, heat loss due to convection is the significant component that inhibits low power operation for a long duration.

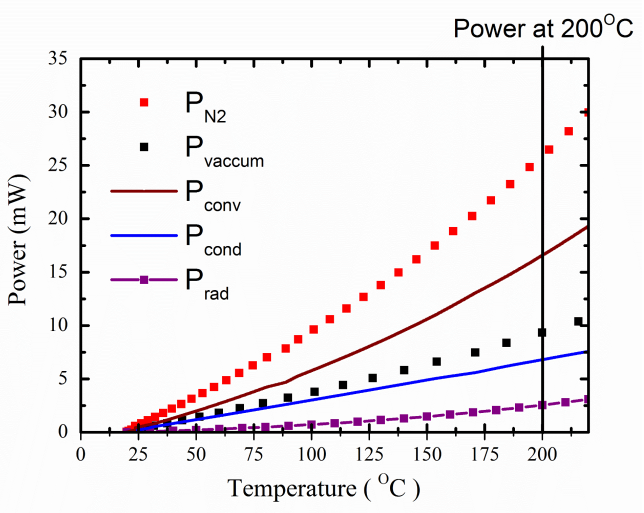

Figure S 3.3: Power consumption in bare device.

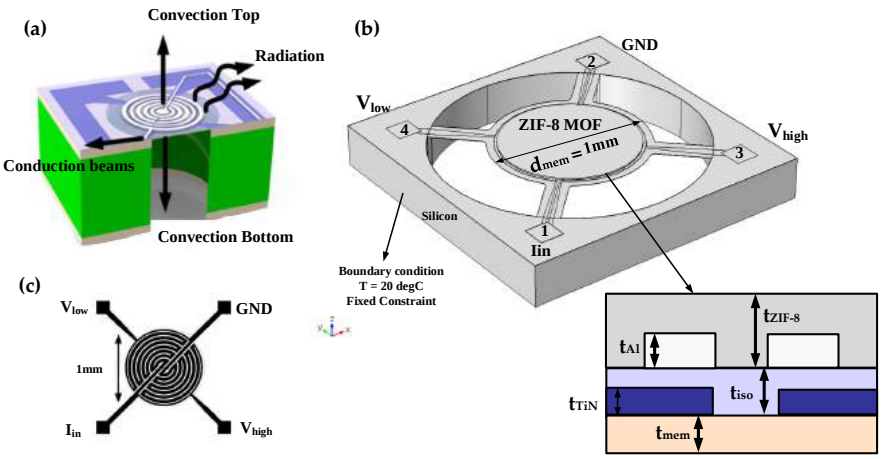

Figure S 3.4: Thermal analysis (**a**) Heat transfer mechanisms in the device. (**b**) 3D geometry for the FEM model with thickness of the materials. (**c**) Micro-hotplate device design.

Thermal Analysis using FEM

The heat generated in the micro-hotplate is transferred by three methods namely: 1) conduction through the beams of the device, 2) convection through the top and bottom of the device and 3) radiation as shown in Figure S 3.4a.

A 3D geometry of the device is developed in COMSOL Multiphysics® 5.3

(Figure S 3.4b). In this 3D model, the electro-thermal analysis is performed by coupling the electrical domain to the thermal domain. The conjugate heat transfer physics is selected for the entire domain, whereas the electric current physics module is only selected for the TiN micro-hotplate with boundary conditions for current input at terminal 1(I_{in}) and ground terminal 2 (GND). The voltage output is measured at terminal 3 (V_{high}) and terminal 4 (V_{low}) enabling a four-probe IV measurement configuration.

The heat generated due to joule heating is proportional to the current density given by [52][53],

$$Q \propto |J|^2 \tag{3.13}$$

$$Q = \frac{|J|^2}{\sigma(T)} \tag{3.14}$$

where σ(T) is the electrical conductivity, T is the temperature and J is the current density. The electrical conductivity is a function of temperature given by,

$$\sigma(T) = \frac{1}{\rho_0(1 + \alpha(T - T_0))} \tag{3.15}$$

where ρ_0 is the electrical conductivity at room temperature (T_0) and α is the temperature co-efficient of resistance (TCR). The value of TCR of the device used for measurement is $\alpha = 0.000725°\mathrm{C}^{-1}$.

The current density is proportional to the electric field E, which is the negative gradient of potential V. Using this in Equation 3.14, we get,

$$Q = \frac{|J|^2}{\sigma(T)} = \frac{|\sigma(T)E|^2}{\sigma(T)} = \sigma(T)|\nabla V|^2 \tag{3.16}$$

The governing equations for the steady-state heat conduction for joule heating process are described below[33],

$$\nabla \cdot (k(T)\nabla T) + \frac{(J^2)}{\sigma(T)} = 0 \tag{3.17}$$

where *k(T)* is the respective thermal conductivity of silicon-nitride membrane, isolation layer, TiN and aluminum electrodes. The material parameters for the FEM model is described in Table 3.5.

Table 3.5: Summary of material parameters for FEM analysis.

Material	**Thermal Conductivity (k) W/mK**	**Density Kg/m3**	**Heat Capacity (Cp) J/kgK**
LPCVD silicon nitride[54]	10-13	3200	700
PECVD silicon nitride[54]	2-4.5	2800	700
Silicon[54]	157	2320	700
TiN[54]	19.2	5220	600
Al[54]	236	2700	900
ZIF-8[29]	0.326	950	700

Table 3.6: Summary of design parameters for FEM analysis.

Design Parameter	Value	Unit
Thickness of silicon nitride (t_{mem})	500	nm
Diameter of membrane (d_{mem})	1	mm
Thickness of silicon nitride isolation layer (t_{SiNx})	1000	nm
Thickness of TiN electrodes (t_{TiN})	400	nm
Thickness of Al electrodes (t_{Al})	1000	nm
Thickness of ZIF-8 MOF (t_{ZIF-8})	10	μm

3.5.4. Optical imaging

The surface morphology of ZIF-8 MOF at different magnification at 20°C, 50°C, 100°C and 300°C is shown in Figure S 3.5a, S 3.5b, S 3.5c and S 3.5d respectively.

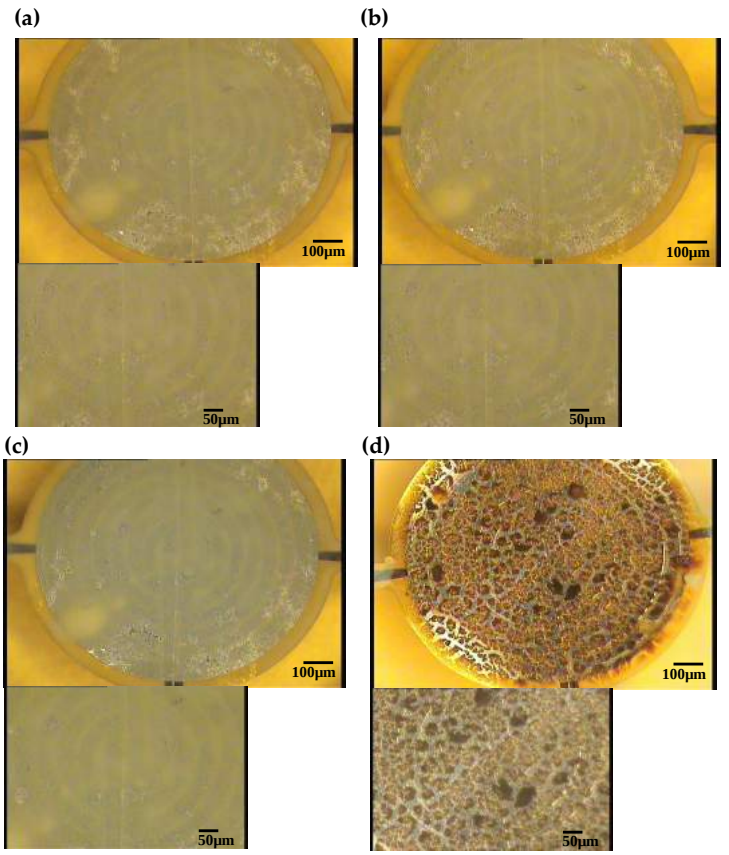

Figure S 3.5: Optical chapter-3 Optical chapter-3 of ZIF-8 coated device (a) 20°C (b) 50°C (c) 100°C (d) 300°C.

3.5.5. Methanol sensing study

The sensing measurements for increasing methanol concentration from 500ppm to 7000ppm with baseline drift calibration line is shown in Figure S 3.6a. After the baseline drift calibration is done, the data for sensing response towards methanol is shown in Figure S 3.6b.

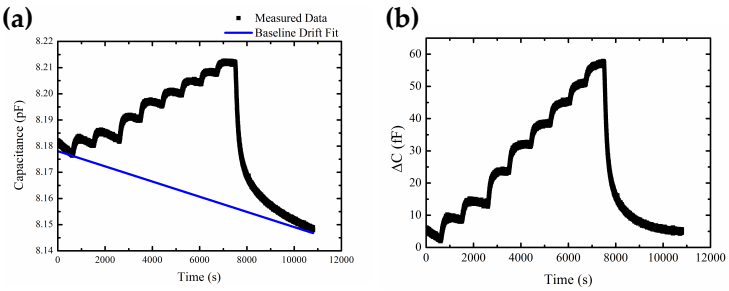

Figure S 3.6: (**a**) Capacitive response for increasing methanol concentration. (**b**) Capacitive response after baseline drift calibration.

The baseline capacitance measurement for ZIF-8 coated device in nitrogen is shown in Figure S 3.7.

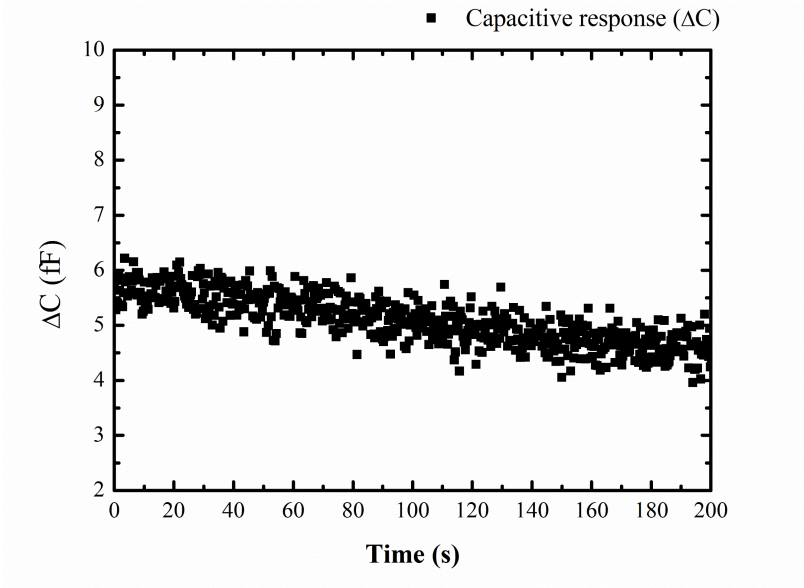

Figure S 3.7: Measured baseline capacitance of ZIF-8 coated device in nitrogen at 20°C.

The reversibility study for exposure to methanol concentration of 5000ppm

with baseline drift calibration line is shown in Figure S 3.8a. The response after the baseline drift calibration is shown in Figure S 3.8b.

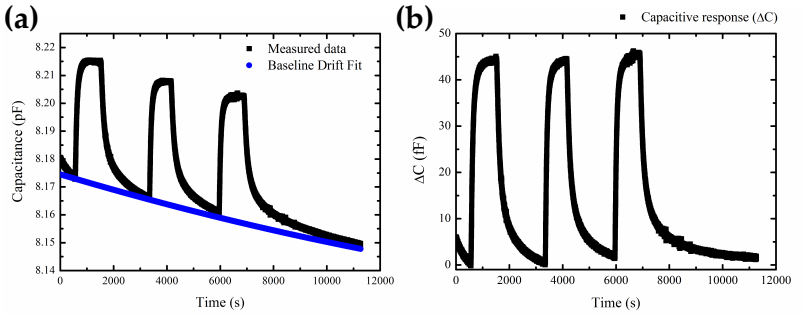

Figure S 3.8: (**a**) Capacitive response for 5000ppm of methanol with baseline drift fitting. (**b**) Capacitive response after baseline drift calibration.

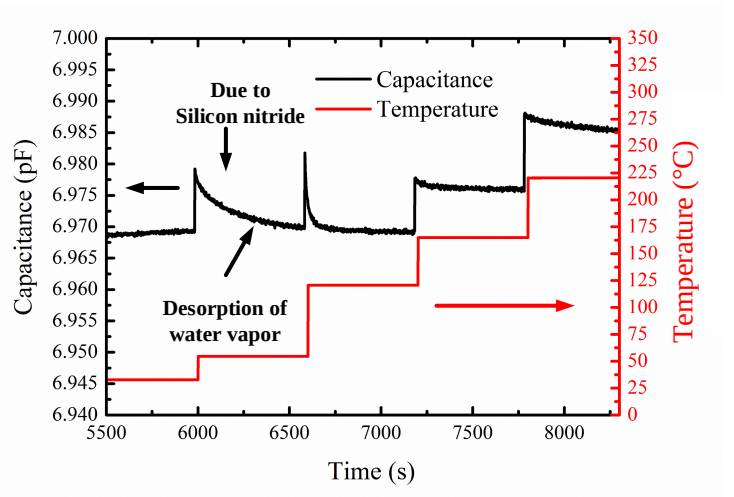

Figure S 3.9: Capacitance of bare device with temperature steps in vacuum.

3.5.6. Temperature-dependent capacitance characterization of the bare device

In this section, the changes in the capacitance of the bare device with temperature due to the SiN_x isolation layer is characterized.

Before the measurement of the capacitance of the bare device, two preconditioning steps in vacuum were performed. In the first step, the entire gas

chamber with the MEMS device was heated in an oven at 100°C for 1hr and cooled to room temperature. In the second step, the operating temperature of the device was increased to 200°C for 30 minutes using the microhotplate and cooled to ambient temperature of 20°C for one hour. These steps were done to remove moisture content that could be present on top of the IDEs while placing the device in the chamber. The capacitance was measured at a constant oscillation voltage of 1V, and at a frequency of 10kHz. The measured capacitance of the bare device after the preconditioning steps was 6.969 pF.

Next, a sequence of temperature steps was programmed using the Keithley 2611B by changing the current through the microhotplate, and the capacitance measured simultaneously as shown in Figure S 3.9. From the measurement data, it is evident that during the temperature steps, there is a change in the capacitance of the bare device. The changes in the capacitance for the temperature steps to 55°C and 120°C is a combination of two behaviors, (i) a sharp increase in ΔC could be due to the change in dielectric constant (ϵ_r) of the PECVD SiN_x isolation layer with increasing temperature, (ii) a slow decay in the capacitance of the device caused by the desorption of residual moisture adsorbed on the top of the IDEs from the chamber surrounding. This can be due to the fact that the vacuum could not be high enough to remove the moisture present in the chamber. For the next temperature steps to 165°C and 220°C, the measured change in capacitance (ΔC) increases and remains almost constant during the temperature cycle. At these high temperatures, the water molecules are not adsorbed on the IDEs, and thus the slow decay is not observed.

In order to accurately determine the observed changes in the bare device capacitance with temperature (behavior (i) and (ii)), the following two experiments were performed,

1. The sharp increase in capacitance (behavior (i)) and the slow decay (behavior (ii)) can be decoupled by changing the temperature of the microhotplate between two temperature points rapidly. In this experiment, the current through the microhotplate is changed per second to obtain two temperature points (fast temperature steps). The capacitance is measured simultaneously at a frequency of 10kHz and oscillation voltage of 1V. The measured capacitance for the fast temperature steps is described in Figure S 3.10a. The temperature of the microhotplate is changed between 30°C to 55°C, 55°C to 115°C, 115°C to 160°C and 160°C to 215°C. Figure 3.10c shows the temperature steps between 55°C to 115°C with the capacitance of the bare device changing from 6.956pF to 6.968pF. The difference in capacitance ΔC of the bare device for the corresponding temperature steps is shown in Figure S 3.10b. The resulting average changes in capacitance ΔC for the fast temperature steps is shown in Figure S 3.10d. It is seen that upon increasing the temperature from 30°C to 220°C, the ΔC of the bare device increases linearly. This change in capacitance is due to the change in the dielectric constant of PECVD SiN_x layer, which needs to be considered as a calibration factor

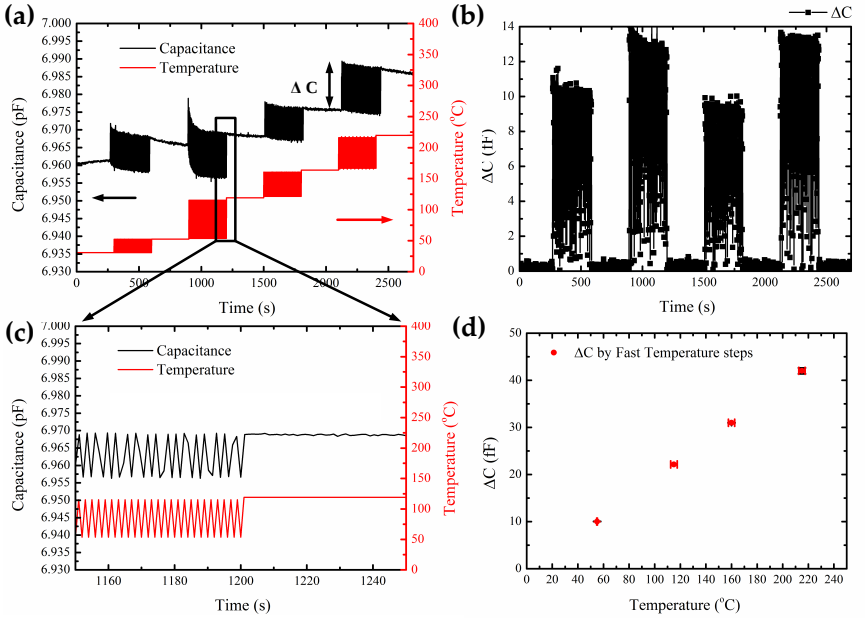

Figure S 3.10: (**a**) Capacitance of the bare device with fast temperature steps in vacuum. (**b**) Capacitance change ΔC in vacuum of the bare device by fast temperature steps. (**c**) Capacitance change ΔC during temperature steps from 55°C to 115°C. (**d**) ΔC versus temperature of the bare device in vacuum during fast temperature steps.

during temperature cycle measurements. It is seen that even during the fast temperature steps, there is an inherent change in the capacitance of the bare device. The resulting change in the bare device capacitance (ΔC) obtained from the single temperature step and fast temperature steps is shown in Figure S 3.11. The change in capacitance ΔC is found to be linear with increasing temperatures. The ΔC obtained from the linear fit at a temperature of 50°C is 7.5fF, and at 200°C it is 38 fF.

2. The change in capacitance purely due to the dielectric constant variation (behavior (i)) can be determined by characterizing a metal-insulator-metal (MIM) capacitor structure. In this experiment, a MIM capacitor with 200nm PECVD SiN_x as the dielectric layer is fabricated and characterized. The fabrication flowchart of the MIM capacitor with PECVD silicon nitride as the dielectric layer is shown in Figure 3.12. A standard 4-inch p-type silicon wafer was used as the substrate for the device. A metal layer of 1μm aluminum was deposited using a Trikon Sigma sputter coater. A layer of 200nm thick PECVD silicon nitride was deposited using Novellus PECVD equipment. The contact opening mask layer was exposed to etch silicon nitride to obtain the contact to the bottom alu-

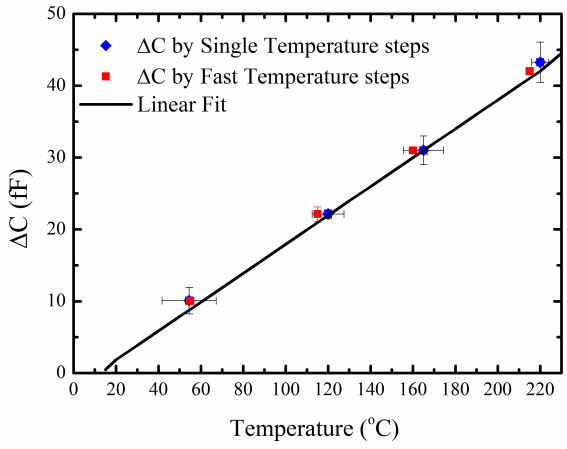

Figure S 3.11: Comparison ΔC versus temperature of the bare device in vaccum for single and fast temperature steps.

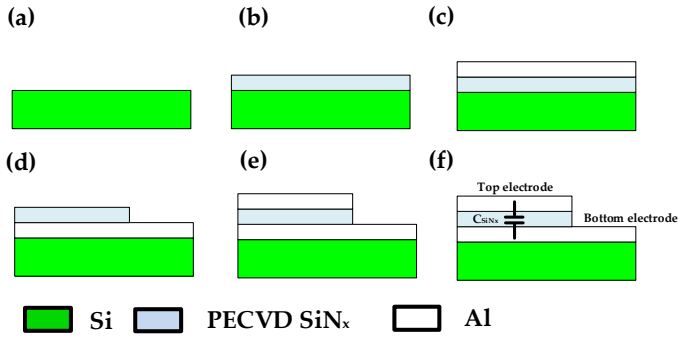

Figure S 3.12: Fabrication process flowchart MIM capacitor (**a**) Silicon substrate. (**b**) 1μm Al 1%Si for bottom metal. (**c**) 200nm PECVD Silicon nitride. (**d**) Bottom electrode contact opening and silicon nitride etching. (**e**) 1μm Al/1%Si for top metal. (**f**) Schematic representation of MIM capacitor C_{SiN_x}.

minum layer. For the top electrode, an aluminum metal layer of 1.4μm was deposited on top of the PECVD silicon nitride.

The capacitance of the MIM capacitor with PECVD SiN_x is given by,

$$C_{SiN_x} = \epsilon_0 \cdot \epsilon_r \cdot \frac{A_{cap}}{d_{cap}} \tag{3.18}$$

where, ϵ_0 is the permittivity of free space, ϵ_r is the dielectric constant of PECVD SiN_x, A_{cap} is the area of the MIM capacitor and d_{cap} is the

thickness of the SiN_x layer. The temperature steps were done using the thermochuck temperature controller from 20°C to 200°C. The capacitance was measured as a function of frequency from 1kHz to 100kHz for different temperatures as shown in Figure 3.13. The measured capacitance and the extracted dielectric constant for different temperatures at a frequency of 10kHz and oscillation voltage of 1V is shown in Figure 3.14. The capacitance of the MIM capacitor increases with increasing temperatures due to the increase in the dielectric constant of the PECVD SiN_x layer. The measured capacitance C_{SiN_x} is 227.78 pF at 20°C and C_{SiN_x} = 230.12 pF at 200°C. The extracted dielectric constant (ϵ_r) increases from 6.554 at 20°C to 6.621 at 200°C.

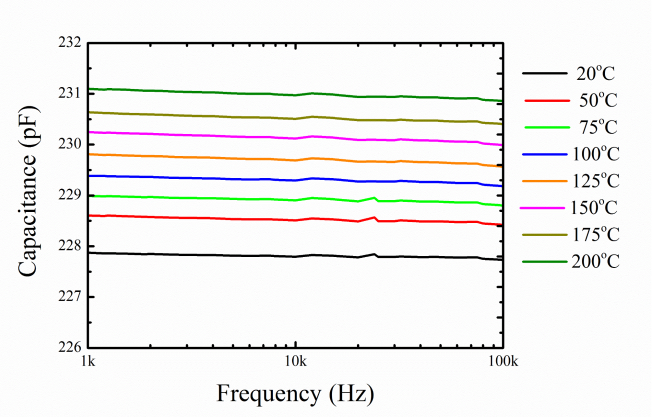

Figure S 3.13: Capacitance versus frequency of MIM capacitor at different temperatures.

FEM analysis of IDE capacitor

In this section, the increase in capacitance due to the temperature-dependent dielectric constant of the SiN_x isolation layer is validated by developing a 2D FEM model of the IDE capacitor.

The obtained relation of ϵ_r vs temperature for the SiN_x isolation layer is used to determine the total capacitance of the device and contribution of the shielded and unshielded electrodes by using a 2D FEM model. The total capacitance between the electrodes depends on the dielectric constants of the substrate and dielectric constant of the layer above the electrodes. Due to the design of the microhotplate electrodes, there are regions where the IDEs are not adequately shielded by the underlying microhotplate electrodes. For a microhotplate designed within a membrane having a diameter of 1mm, about 67% of the area underneath the IDE is shielded by the microhotplate pattern whereas 33% of the area under the IDEs is not shielded. Thus, the total capacitance is obtained by the sum of two capacitances: shielded IDEs ($C_{shielded}$) and unshielded IDEs ($C_{unshielded}$).

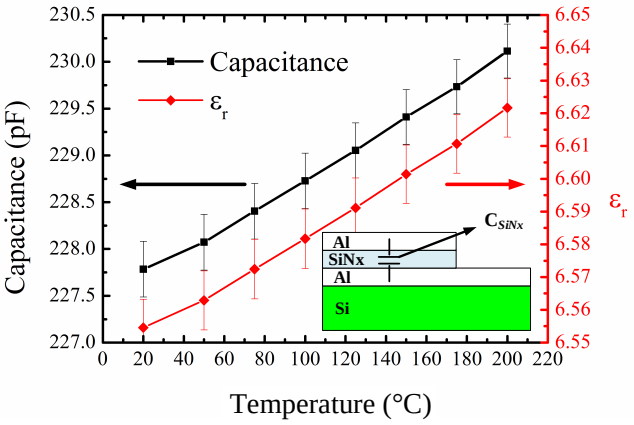

Figure S 3.14: Dielectric constant and capacitance of MIM capacitor at different temperatures.

Figure 3.15b illustrates a local cross-section of the IDE and heater structure, together with a corresponding circuit model (only capacitive components are shown.). The total capacitance is given by,

$$C_{total} = C_{shielded} + C_{unshielded} \tag{3.19}$$

where,

$$C_{shielded} \text{ and } C_{unshielded} = C_{IDE} + C_{parasitic} \tag{3.20}$$

The parasitic capacitance contributing to the shielded IDEs is mainly due to the isolation layer capacitance (C_{1s}). However, the parasitic capacitances for the unshielded IDEs are due to the isolation layer capacitance (C_1), membrane layer capacitance (C_2), and capacitance through the space underneath the membrane (C_3) as described in Figure 3.15a.

A 2D FEM model is developed by considering the half spacial wavelength for aluminum IDE pair with SiN_x membrane, TiN electrode, SiN_x isolation layer (Figure 3.15c and 3.15d)[55][56]. One electrode terminal is defined with potential $V_0 = 1V$ and second electrode terminal is defined as ground. The other sides of the 2D model are at a boundary condition of zero charge. The electric field for the FEM is computed by solving Gauss's law with electric potential V_0 as the independent variable[56]. The capacitance of the IDEs in the FEM model is calculated by computing the terminal charges at the electrodes given by,

$$C_{total} = N \cdot \frac{Q}{V_0} \tag{3.21}$$

where, N is the number of electrode pairs. The IDE dimensions based on the design parameters are W = 2μm, G = 1μm and the number of electrodes

(N) is 164. The thickness of the isolation layer is 1μm and thickness of aluminum electrodes is 1μm. The device capacitance is simulated at a frequency of 10kHz. The capacitance C_{total} is obtained as a function of the dielectric constant of the silicon nitride layer and the change in capacitance (ΔC) for the temperature steps is calculated. The resulting change in capacitance (ΔC) of the IDE capacitor is found to be increasing linearly with temperature as shown in Figure 3.16.

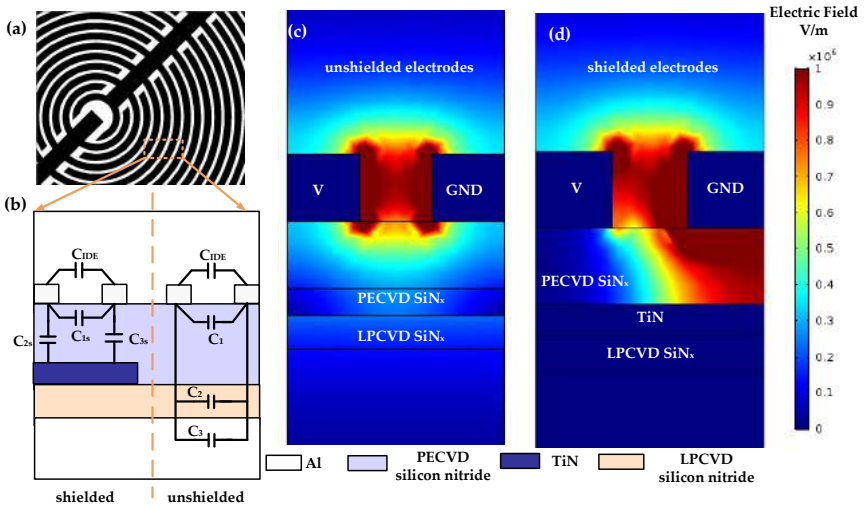

Figure S 3.15: FEM Modelling of IDE capacitor. (**a**) Mask layout of a circular IDE. (**b**) Cross-section view of IDE with microhotplate electrodes. (**c**) Electric field distribution of unshielded electrodes. (**b**) Electric field distribution of shielded electrodes.

Capacitance Calibration

The linear change in the capacitance of the bare device (ΔC) with increasing temperatures as described in Figure 3.17, is found to be mainly due to the change in the dielectric constant of PECVD SiN_x isolation layer with temperature, and it is validated by the above two experiments. At a temperature of 200°C, the difference between FEM data and experimental calibration of ΔC is 12% for single temperature steps, and 17% for fast temperature steps (Figure 3.17). The length of the electrode, the area of the shielded and unshielded electrode pair need to be more accurately determined for the 2D model. Thus, the FEM model can be used for flexible designs of the IDE capacitor integrated with microhotplate. The linear fit derived in this section is used as the calibration factor for temperature-dependent capacitance sensing study in Section 3.5 in the main manuscript.

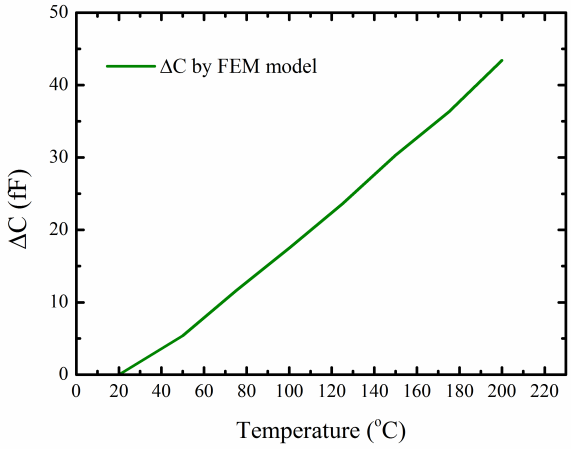

Figure S 3.16: ΔC versus temperature of the bare device obtained by FEM model.

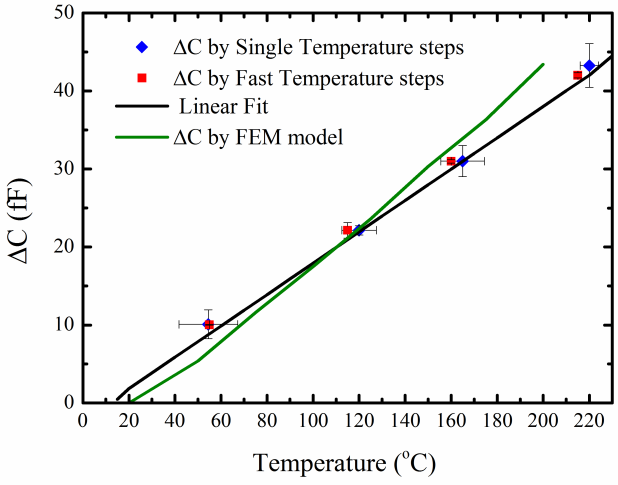

Figure S 3.17: ΔC versus temperature of the bare device obtained by FEM model.

3.5.7. Temperature-dependent methanol and water vapor sensing response

The measured response has two calibration steps for the data analysis of temperature-dependent sensing response. First, the measured data is calibrated with temperature-dependent isolation layer capacitance (ΔC_{SiN_x}). In

the second step, the baseline drift is calibrated. The data analysis for the capacitance sensing response to exposure of methanol and water vapor at a constant concentration of 5000ppm for different temperatures is shown in Figure 3.18a - 3.18i and Figure 3.19a - 3.19i, respectively.

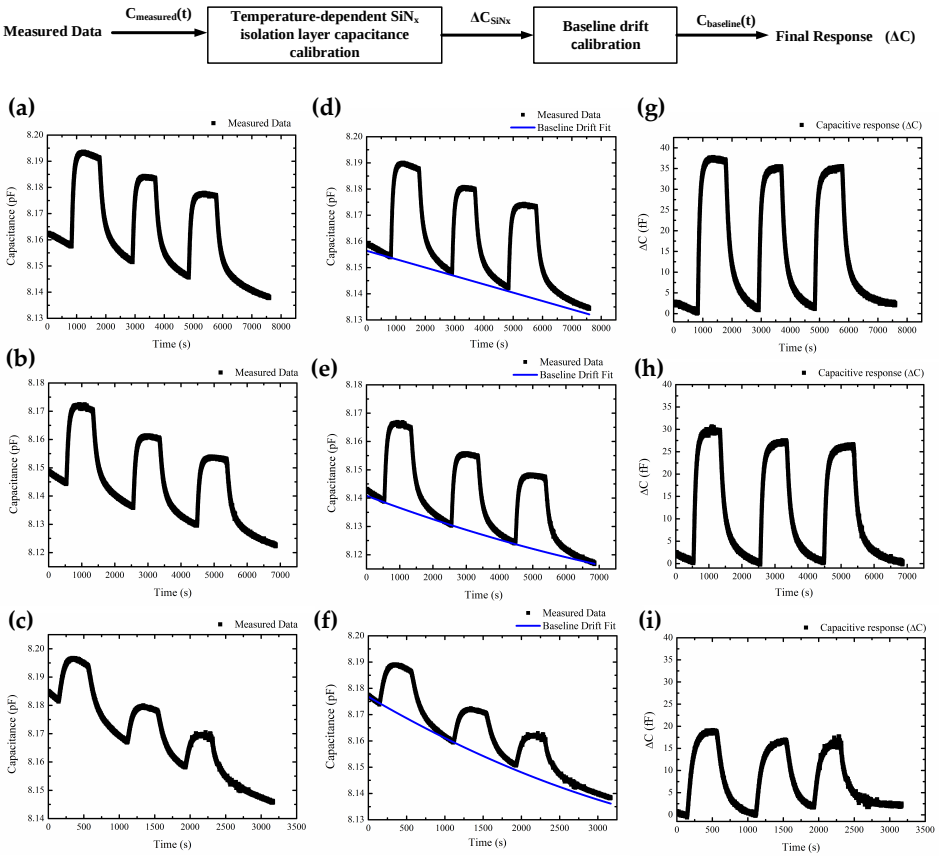

Figure S 3.18: Capacitive response for exposure to methanol concentration of 5000ppm at (**a**) 30°C (**b**) 40°C (**c**) 50°C. Capacitive response after SiN_x isolation layer capacitance calibration (**d**) 30°C (**e**) 40°C (**f**) 50°C. Final Capacitive response (Δ C) after baseline drift calibration (**g**) 30°C (**h**) 40°C (**i**) 50°C.

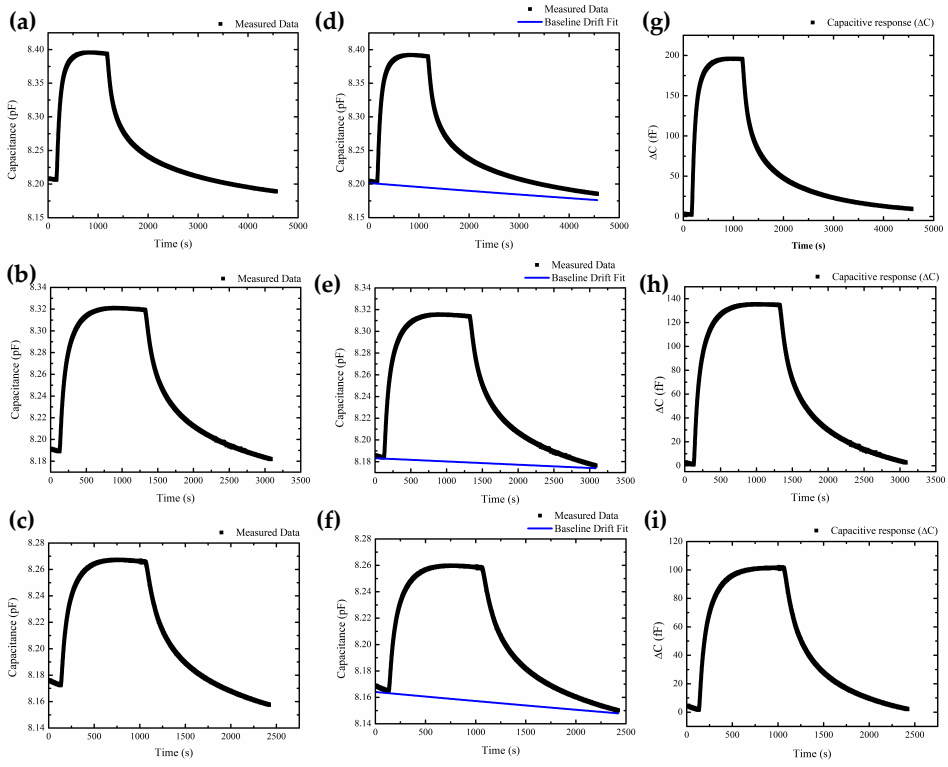

Figure S 3.19: Capacitive response for exposure to water vapor concentration of 5000ppm at (**a**) 30°C (**b**) 40°C (**c**) 50°C. Capacitive response after SiN_x isolation layer capacitance calibration (**d**) 30°C (**e**) 40°C (**f**) 50°C. Final Capacitive response (Δ C) after baseline drift calibration (**g**) 30°C (**h**) 40°C (**i**) 50°C.

3.5.8. Stability test

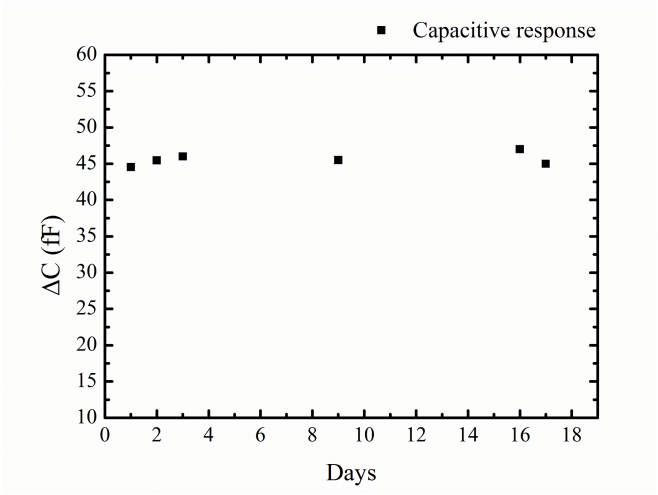

Figure S 3.20: Stability test with ZIF-8 MOF to Methanol concentration of 5000ppm.

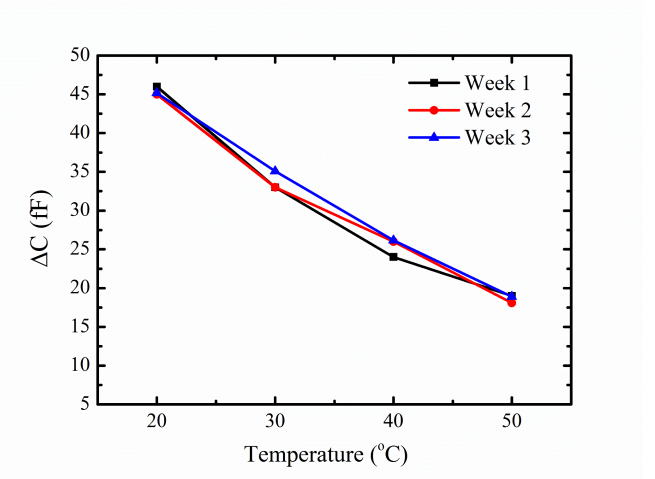

Figure S 3.21: Temperature dependent capacitance response to 5000ppm methanol measured over three weeks.

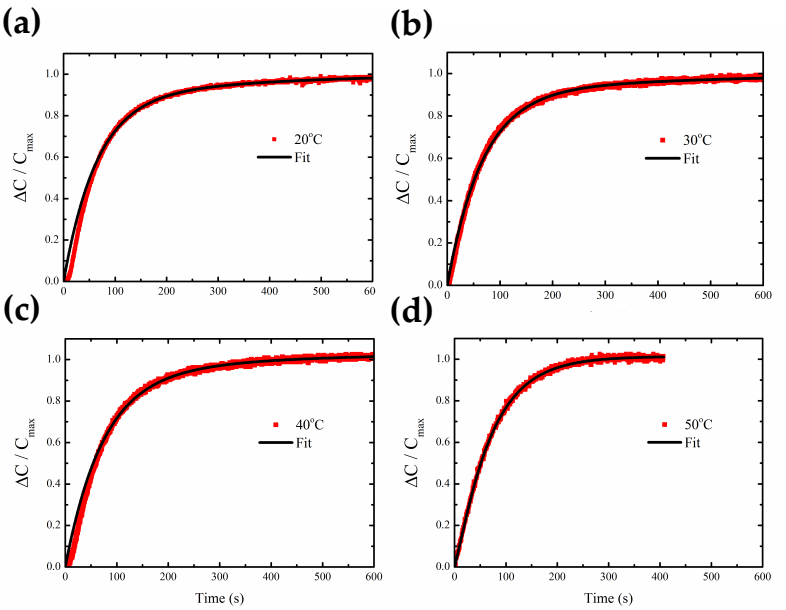

Figure S 3.22: Time-dependent adsorption kinetic fit for exposure to methanol concentration of 5000ppm at (**a**) 20°C (**b**) 30°C (**c**) 40°C (**d**) 50°C.

3.5.9. Temperature-dependent adsorption and desorption kinetic modelling

In this section, the time-dependent kinetics of methanol fitted using double exponential model at different temperatures is described. The curve fit is obtained using Equation 3.22 for the adsorption process and described in Figures 3.22a - d. Equation 3.23 is used for the curve fit of the desorption process and shown in Figures 3.23a - d. The kinetic parameters extracted for the adsorption and desorption curves with corresponding regression co-coefficients is shown in Table 3.7 and Table 3.8 respectively.

$$\frac{\Delta C}{C_{max}} = A_{1a}(1 - e^{-k_1}) + A_{2a}(1 - e^{-k_2}) \tag{3.22}$$

$$\frac{\Delta C}{C_{max}} = A_{1d}(e^{-k_3}) + A_{2d}(e^{-k_4}) \tag{3.23}$$

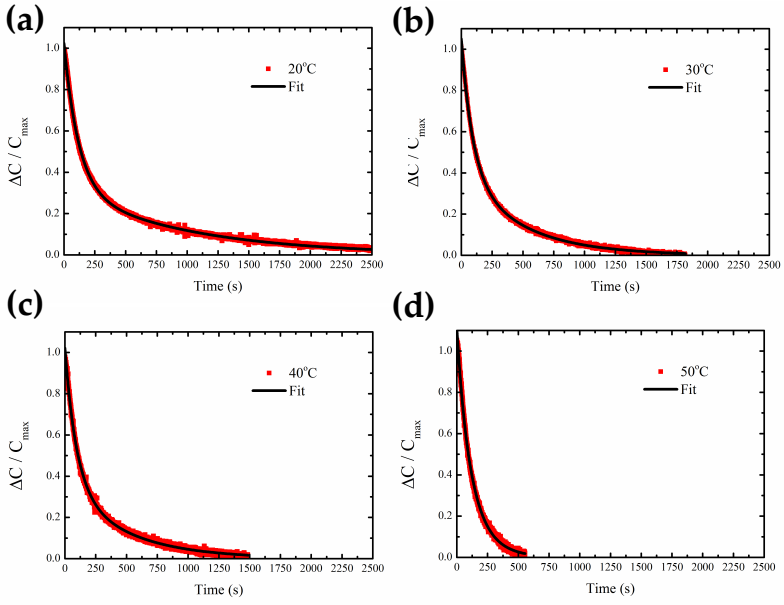

Figure S 3.23: Time-dependent adsorption kinetic fit for exposure to methanol concentration of 5000ppm at (**a**) 20°C(**b**) 30°C (**c**) 40°C (**d**) 50°C.

Table 3.7: Table of kinetic parameters and regression co-efficient for adsorption curves.

Temperature	$\mathbf{k}_1$	$\mathbf{k}_2$	$\mathbf{R}^2$
20	0.0158	0.0029	99.95
30	0.0151	0.0021	99.81
40	0.0141	0.0035	99.86
50	0.0131	0.0049	99.89

Table 3.8: Table of kinetic parameters and regression co-efficient for desorption curves.

Temperature	$\mathbf{k}_3$	$\mathbf{k}_4$	$\mathbf{R}^2$
20	0.0141	0.0010	99.86
30	0.0109	0.0021	99.89
40	0.0107	0.0020	99.85
50	0.0108	0.0060	99.80

References

[1] A. Mirzaei, S. Leonardi, and G. Neri, *Detection of hazardous volatile organic compounds (vocs) by metal oxide nanostructures-based gas sensors: A review,* Ceramics International **42**, 15119 (2016).

[2] L. E. Kreno, K. Leong, O. K. Farha, M. Allendorf, R. P. Van Duyne, and J. T. Hupp, *Metal–organic framework materials as chemical sensors,* Chemical Reviews **112**, 1105 (2011).

[3] M. G. Campbell and M. Dincă, *Metal–organic frameworks as active materials in electronic sensor devices,* Sensors **17**, 1108 (2017).

[4] C. Yim, M. Lee, W. Kim, S. Lee, G.-H. Kim, K. T. Kim, and S. Jeon, *Adsorption and desorption characteristics of alcohol vapors on a nanoporous zif-8 film investigated using silicon microcantilevers,* Chemical Communications **51**, 6168 (2015).

[5] M. G. Campbell, S. F. Liu, T. M. Swager, and M. Dincă, *Chemiresistive sensor arrays from conductive 2d metal–organic frameworks,* Journal of the American Chemical Society **137**, 13780 (2015).

[6] M. Ko, L. Mendecki, and K. A. Mirica, *Conductive two-dimensional metal–organic frameworks as multifunctional materials,* Chemical Communications (2018).

[7] B. Hoppe, K. D. Hindricks, D. P. Warwas, H. A. Schulze, A. Mohmeyer, T. J. Pinkvos, S. Zailskas, M. R. Krey, C. Belke, S. König, *et al.*, *Graphene-like metal–organic frameworks: morphology control, optimization of thin film electrical conductivity and fast sensing applications,* CrystEngComm **20**, 6458 (2018).

[8] B. Chen, Z. Yang, Y. Zhu, and Y. Xia, *Zeolitic imidazolate framework materials: recent progress in synthesis and applications,* Journal of Materials Chemistry A **2**, 16811 (2014).

[9] S. Eslava, L. Zhang, S. Esconjauregui, J. Yang, K. Vanstreels, M. R. Baklanov, and E. Saiz, *Metal-organic framework zif-8 films as low-κ dielectrics in microelectronics,* Chemistry of Materials **25**, 27 (2012).

[10] X.-C. Huang, Y.-Y. Lin, J.-P. Zhang, and X.-M. Chen, *Ligand-directed strategy for zeolite-type metal–organic frameworks: zinc (ii) imidazolates with unusual zeolitic topologies,* Angewandte Chemie International Edition **45**, 1557 (2006).

[11] J. Hromadka, B. Tokay, S. James, R. P. Tatam, and S. Korposh, *Optical fibre long period grating gas sensor modified with metal organic framework thin films,* Sensors and Actuators B: Chemical **221**, 891 (2015).

[12] J. Hromadka, B. Tokay, R. Correia, S. P. Morgan, and S. Korposh, *Highly sensitive volatile organic compounds vapour measurements using a long period grating optical fibre sensor coated with metal organic framework zif-8,* Sensors and Actuators B: Chemical **260**, 685 (2018).

[13] G. Lu and J. T. Hupp, *Metal- organic frameworks as sensors: a zif-8 based fabry- pérot device as a selective sensor for chemical vapors and gases,* Journal of the American Chemical Society **132**, 7832 (2010).

[14] S. Sachdeva, S. J. Koper, A. Sabetghadam, D. Soccol, D. J. Gravesteijn, Kapteijn, E. J.R Sudhölter, J. Gascon, and L. C.P.M de Smet, *Gas phase sensing of alcohols by metal organic framework–polymer composite materials,* ACS Applied Materials & Interfaces **9**, 24926 (2017).

[15] S. Sachdeva, M. R. Venkatesh, B. E. Mansouri, J. Wei, A. Bossche, F. Kapteijn, G. Q. Zhang, J. Gascon, L. C.P.M. de Smet, and E. J.R. Sudhölter, *Sensitive and reversible detection of methanol and water vapor by in situ electrochemically grown cubtc mofs on interdigitated electrodes,* Small **13** (2017).

[16] K.-P. Yoo, M. J. Lee, K.-H. Kwon, J. Jeong, and N.-K. Min, *Dielectric properties of on-chip-cured polyimide films,* Thin Solid Films **518**, 5986 (2010).

[17] U. Kang and K. D. Wise, *A high-speed capacitive humidity sensor with on-chip thermal reset,* IEEE Transactions on Electron Devices **47**, 702 (2000).

[18] C.-L. Zhao, M. Qin, and Q.-A. Huang, *A fully packaged cmos interdigital capacitive humidity sensor with polysilicon heaters,* IEEE Sensors Journal **11**, 2986 (2011).

[19] D. Mutschall and E. Obermeier, *A capacitive co2 sensor with on-chip heating,* Sensors and Actuators B: Chemical **25**, 412 (1995).

[20] R. Blue and D. Uttamchandani, *Chemicapacitors as a versatile platform for miniature gas and vapor sensors,* Measurement Science and Technology **28**, 022001 (2016).

[21] A. Demessence, C. Boissiere, D. Grosso, P. Horcajada, C. Serre, G. Férey, G. J. Soler-Illia, and C. Sanchez, *Adsorption properties in high optical quality nanozif-8 thin films with tunable thickness,* Journal of Materials Chemistry **20**, 7676 (2010).

[22] J. Staginus, Z. Chang, E. J.R Sudhölter, L. C.P.M. de Smet, and G. C. Meijer, *Water-enhanced guarding of polymer-coated ide platforms as a key mechanism for achieving response immunity towards parasitic coupling events,* Sensors and Actuators A: Physical **234**, 239 (2015).

[23] *National center for biotechnology information. pubchem compound database; cid=795,* `https://pubchem.ncbi.nlm.nih.gov/compound/795`, accessed Mar. 31, 2018.

[24] P. Bhattacharyya, *Technological journey towards reliable microheater development for mems gas sensors: a review,* IEEE Transactions on Device and Materials Reliability **14**, 589 (2014).

[25] V. Toffoli, S. Carrato, D. Lee, S. Jeon, and M. Lazzarino, *Heater-integrated cantilevers for nano-samples thermogravimetric analysis,* Sensors **13**, 16657 (2013).

[26] C. Alepee and N. Moser, *Micro-hotplate device and sensor comprising such micro-hotplate device,* `https://patents.google.com/patent/US9228967` (2013), uS Patent 9228967B2.

[27] J. Creemer, D. Briand, H. Zandbergen, W. Van der Vlist, C. De Boer, N. F. de Rooij, and P. Sarro, *Microhotplates with tin heaters,* Sensors and Actuators A: Physical **148**, 416 (2008).

[28] M. Venkatesh, B. El Mansouri, J. Wei, A. Bossche, and G. Zhang, *Electrothermal analysis and design of a combined mems impedance and micro hotplate device for gas sensing applications,* in *Thermal, Mechanical and Multi-Physics Simulation and Experiments in Microelectronics and Microsystems (EuroSimE), 2016 17th International Conference on* (IEEE, 2016) pp. 1–9.

[29] J. Cravillon, R. Nayuk, S. Springer, A. Feldhoff, K. Huber, and M. Wiebcke, *Controlling zeolitic imidazolate framework nano-and microcrystal formation: insight into crystal growth by time-resolved in situ static light scattering,* Chemistry of Materials **23**, 2130 (2011).

[30] Y. Liu, G. Wei, L. Pan, M. Xiong, H. Yan, Y. Li, C. Lu, and Y. Qiao, *Rhombic dodecahedron zif-8 precursor: Designing porous n-doped carbon for sodium-ion batteries,* ChemElectroChem **4**, 3244 (2017).

[31] A. Schejn, L. Balan, V. Falk, L. Aranda, G. Medjahdi, and R. Schneider, *Controlling zif-8 nano-and microcrystal formation and reactivity through zinc salt variations,* CrystEngComm **16**, 4493 (2014).

[32] R. Igreja and C. Dias, *Analytical evaluation of the interdigital electrodes capacitance for a multi-layered structure,* Sensors and Actuators A: Physical **112**, 291 (2004).

[33] C. Silvestri, P. Picciafoco, B. Morana, F. Santagata, G. Zhang, and P. Sarro, *Electro-thermal simulation and characterization of vertically aligned cnts directly grown on a suspended microhoplate for thermal management applications,* in *IEEE Sensors* (2014) pp. 827–830.

[34] H.-E. Endres, R. Hartinger, M. Schwaiger, G. Gmelch, and M. Roth, *A capacitive co2 sensor system with suppression of the humidity interference,* Sensors and Actuators B: Chemical **57**, 83 (1999).

[35] M. Elkhayat, S. Mangiarotti, M. Grassi, P. Malcovati, and A. Fornasari, *Capacitance humidity micro-sensor with temperature controller and heater integrated in cmos technology,* (2018) pp. 383–387.

[36] H. Yin, H. Kim, J. Choi, and A. C. Yip, *Thermal stability of zif-8 under oxidative and inert environments: A practical perspective on using zif-8 as a catalyst support,* Chemical Engineering Journal **278**, 293 (2015).

[37] J. Tang, J. Fang, Y. Liang, B. Zhang, Y. Luo, X. Liu, Z. Li, X. Cai, J. Xian, H. Lin, *et al.*, *All-fiber-optic voc gas sensor based on side-polished fiber wavelength selectively coupled with cholesteric liquid crystal film,* Sensors and Actuators B: Chemical **273**, 1816 (2018).

[38] J. Wei, C. Yue, Z. Chen, Z. Liu, and P. Sarro, *A silicon mems structure for characterization of femto-farad-level capacitive sensors with lock-in architecture,* Journal of Micromechanics and Microengineering **20**, 064019 (2010).

[39] S. Homayoonnia and S. Zeinali, *Design and fabrication of capacitive nanosensor based on mof nanoparticles as sensing layer for vocs detection,* Sensors and Actuators B: Chemical **237** (2016), 10.1016/j.snb.2016.06.152.

[40] N. Banerjee, S. Roy, C. K. Sarkar, and P. Bhattacharyya, *High dynamic range methanol sensor based on aligned zno nanorods,* IEEE Sensors Journal **13**, 1669 (2013).

[41] M. Parmar and K. Rajanna, *Copper (ii) oxide thin film for methanol and ethanol sensing,* International Journal on Smart Sensing and Intelligent Systems **4** (2011).

[42] L. Yadava, R. Verma, and R. Dwivedi, *Sensing properties of cds-doped tin oxide thick film gas sensor,* Sensors and Actuators B: Chemical **144**, 37 (2010).

[43] M. Barzegar, M. Berahman, *et al.*, *Sensing behavior of flower-shaped mos2 nanoflakes: case study with methanol and xylene,* Beilstein journal of nanotechnology **9**, 608 (2018).

[44] H. Guo, X. Chen, Y. Yao, G. Du, and H. Li, *Detection of ethanol and methanol vapors using polymer-coated piezoresistive si bridge,* Sensors and Actuators B: Chemical **155**, 519 (2011).

[45] K. Zhang, R. P. Lively, C. Zhang, W. J. Koros, and R. R. Chance, *Investigating the intrinsic ethanol/water separation capability of zif-8: an adsorption and diffusion study,* The Journal of Physical Chemistry C **117**, 7214 (2013).

[46] A. J. Fletcher, E. J. Cussen, D. Bradshaw, M. J. Rosseinsky, and K. M. Thomas, *Adsorption of gases and vapors on nanoporous ni2 (4, 4 '-bipyridine) 3 (no3) 4 metal- organic framework materials templated with methanol and ethanol: Structural effects in adsorption kinetics,* Journal of the American Chemical Society **126**, 9750 (2004).

[47] A. Kondo, N. Kojima, H. Kajiro, H. Noguchi, Y. Hattori, F. Okino, K. Maeda, T. Ohba, K. Kaneko, and H. Kanoh, *Gas adsorption mechanism and kinetics of an elastic layer-structured metal–organic framework,* The Journal of Physical Chemistry C **116**, 4157 (2012).

[48] M. J. Al-Marri, Y. O. Kuti, M. Khraisheh, A. Kumar, and M. M. Khader, *Kinetics of co2 adsorption/desorption of polyethyleneimine-mesoporous silica,* Chemical Engineering & Technology **40**, 1802 (2017).

[49] H. Huang, W. Zhang, D. Liu, B. Liu, G. Chen, and C. Zhong, *Effect of temperature on gas adsorption and separation in zif-8: A combined experimental and molecular simulation study,* Chemical engineering science **66**, 6297 (2011).

[50] C. Silvestri, M. Riccio, R. H. Poelma, B. Morana, S. Vollebregt, F. Santagata, A. Irace, G. Q. Zhang, and P. M. Sarro, *Thermal characterization of carbon nanotube foam using mems microhotplates and thermographic analysis,* Nanoscale **8**, 8266 (2016).

[51] A. Pike and J. W. Gardner, *Thermal modelling and characterisation of micropower chemoresistive silicon sensors,* Sensors and Actuators B: Chemical **45**, 19 (1997).

[52] *Example—Resistive Heating, COMSOL Multiphysics,* https://www.comsol.com/forum/thread/attachment/65707/resistive_heating_sbs-10665.pdf ().

[53] *Heating Circuit, COMSOL Multiphysics,* https://www.comsol.com/model/download/468651/models.sme.heating_circuit.pdf ().

[54] M. Madou, *Fundamentals of Microfabrication: The Science of Miniaturization, Second Edition* (Taylor & Francis, 2002).

[55] A. V. Mamishev, K. Sundara-Rajan, F. Yang, Y. Du, and M. Zahn, *Interdigital sensors and transducers,* Proceedings of the IEEE **92**, 808 (2004).

[56] J. Oberländer, Z. B. Jildeh, P. Kirchner, L. Wendeler, A. Bromm, H. Iken, P. Wagner, M. Keusgen, and M. J. Schöning, *Study of interdigitated electrode arrays using experiments and finite element models for the evaluation of sterilization processes,* Sensors **15**, 26115 (2015).

4

Porous Organic Framework (POFs)

Parts of this chapter is part of the manuscript to be submitted - "Porous Organic framework as affinity layer for capacitive sensing of ethanol and methanol vapors", **Venkatesh, M.R.**; Sumit Sachdeva; Wei, J.; Bosma, D; Bossche, A.; Zhang, G.Q., Scholdhter, Ernst *MDPI Sensors* , *To be Submitted*

4.1. Introduction

Volatile Organic Compounds (VOC)s are organic chemical compounds, having low boiling point (50°C–250°C) and form vapors under ambient atmospheric conditions[1]. Methanol and ethanol are the most common VOCs found in indoor air environment that are obtained from sources such as paints, adhesives and automotive fuels. Continuous exposure to VOCs above the threshold limit values (TLV) for a period more than eight hours can cause drowsiness, headache and difficulty in breathing. The TLV for methanol and ethanol is 200ppm and 1000ppm respectively[1]. Thus, continuous monitoring of exposure levels of VOCs is important for healthy indoor air environment. Detection of such VOCs for long duration require portable and mobile devices having low-cost, miniaturized and low-power sensors. Wafer-scale semiconductor process technologies allow fabrication of miniaturized and low-cost devices for sensing studies such as, field effect transistor (FET), resistive and capacitive transducers. Chemical sensors developed with capacitor transducers defined as chemicapacitors, have advantages due to their low-power consumption, simple device fabrication and ability to detect target analytes operating at ambient atmospheric conditions[2][3].

A chemicapacitor sensor consists of two main components, a capacitor transducer such as interdigitated electrodes (IDEs) fabricated by patterning metal layer on a silicon substrate, and a thin film of the affinity layer deposited on top of the IDEs that can selectively interact with certain analytes present in the environment. In these sensors, the changes in the measured capacitance are dependent on the changes in the effective dielectric constant of the affinity layer, interaction of the analytes with the affinity layer by hydrogen bonding or Lewis acid-base interactions, changes in the effective affinity layer thickness due to swelling and amount of analyte absorbed in the affinity layer[2–5]. Polymers and porous materials deposited as thin film on IDEs are mainly used as the affinity layers in the development of chemicapacitor sensors. Polymers such as Polydimethylsiloxane (PDMS), Poly(methyl methacrylate) (PMMA), Poly(2-hydroxyethyl methacrylate) (PHEMA) and (epoxydised novolac) EPR coated on IDE capacitor operating at room temperature, have been studied for the detection of methanol, ethanol, toluene and water vapor[4]. In addition, polymer films such as Polyethylenimine (PEI), Poly(butyl methacrylate) PBMA and Poly(ethyl methacrylate) PEMA also show capacitive response to increasing concentrations of ethyl acetate and water vapor[6]. Thus, polymer films as affinity layers for chemicapacitor sensors have advantages such as, simple material synthesis procedures, availability of numerous polymers, controlled deposition on capacitor transducers and sensitive detection of certain VOCs. Among the porous materials used for capacitive gas sensors, crystalline porous materials such as Metal-Organic Framework (MOFs) have been studied due to their advantages of selective gas adsorption capability. Thin film of MOFs such as CuBTC MOF as affinity layers for chemicapacitor sensors have been successfully studied for the detection of methanol and water vapor. The detection of alcohols resulting from the changes in the effective dielectric

constant in the MOF layer is mainly due to the diffusion of gas molecules and interaction with the porous framework of MOFs. Polymer-MOF composite studied with dispersion of NH2-MIL-53(Al)MOF nanoparticles in Matrimid polymer matrix have shown an increased sensitivity and response time for the detection of methanol[7]. Furthermore, it is seen that such polymer-MOF composite film allows increased uptake of methanol due to the presence of porous MOF nanoparticles within the polymer framework. Addition of the nanoparticles within polymer have also been studied for capacitive CO_2 sensors. Silica nanoparticles incorporated within Polyethylenimine(PEI) and deposited on capacitor transducers, show an increased sensitivity for sensing of CO_2 due to the increase in available and accessible amine groups in polyethyleneimine[8]. Hence, it is seen that by the addition of MOFs and silicon nanoparticles in polymers improve the gas adsorption capability of the polymer film, increases the surface area for interaction with gas molecules and enhances the sensitivity for gas sensing applications. In recent years, there has been significant interest in the synthesis and process development of thin film porous polymers. Porous polymers are defined as polymers having a combination of properties of both porous materials and polymers. They are characterized with high surface areas and well-defined porosity[9]. Porous organic framework(POFs) are one type of micro-porous polymers which are derived from organic precursors which are covalently bonded having high porosity[10]. POFs are very advantageous for gas sensing applications due to their high surface areas, large porosity that enables diffusion of gas molecules and interaction within the 3D framework of the polymer at multiple pore sites. The synthesis of such porous polymers include template-based approach, direct synthesis method and block co-polymer self-assembly[9]. Among these various methods, direct synthesis method with Schiff based chemistry for one-pot synthesis of porous organic framework not only allow a simple fabrication process, but also enable to develop thin film coating on sensor devices[11]. The synthesis of nitrogen rich porous organic framework with Schiff based chemistry are done using melamine and teraphtadlehyde as the building blocks using a one-pot poly condensation approach. Such melamine based POFs functionalised with platinum(Pt) nanoparticles coated on silicon-nanowires was used for the detection of methanol[10]. In this study, the metallisation of the POF with Pt nanoparticles enhanced sensitivity to methanol vapors in the concentration range 1200ppm to 6400ppm is compared to pure POF modified silicon nanowires. Melamine based POFs being non-conductive, another approach that can be investigated is by using capacitive transducers to monitor the changes in capacitance upon exposure to ethanol and methanol vapors. In addition, melamine based POFs are rich in amine functional groups (-NH), that have higher capability to interact and form hydrogen bond with the –OH group present in ethanol and methanol.

4.2. Experimental

4.2.1. Device design and fabrication

A schematic illustration of the proposed IDE capacitor device coated with porous organic framework (POF) is shown in Figure 4.1a. In this device, a p-type silicon with a thickness of 300μm is used as the substrate material. The aluminum interdigitated electrodes in a circular structure are patterned on a 500nm silicon nitride dielectric layer. POF dispersed in 1-propanol are drop-casted using a pipette on the capacitor region to ensure complete coverage of the surface IDE capacitor. The area of the capacitor electrodes with POF coating should be sufficient to obtain higher base capacitance with measurable changes in the capacitance upon exposure to ethanol and methanol vapors. Along with this, the design parameters of the IDE electrodes such as width of the electrodes (W), gap between the electrodes (G) and number of electrodes (N) must be optimised to obtain a higher base capacitance within a defined area of the bare device. The total capacitance of the bare IDE capacitor device considering the design parameters of the electrodes and materials used in the device fabrication can be evaluated by developing a 2D Finite element model (FEM) in COMSOL multiphysics.

A cross-section of the device is shown in Figure 4.1b. LPCVD silicon nitride with a thickness of 500nm is used as the dielectric material. The diameter of the active region of the sensor for the IDE capacitor is taken as 500nm and 1000μm to have sufficient area for coating of the POF by drop-casting using the pipette. Aluminum electrodes having a thickness of 500nm with varying width (W), gap (G) and number of electrodes accommodated within the diameter of the active region of the sensor is used in the development of the 2D FEM model. In an IDE capacitor device, the periodicity of the electrodes are modelled by spatial wavelength (λ) given by (λ) = 2*(W+G)[4]. In the 2D FEM model, a half spatial wavelength ($\lambda/2$) is defined from the centre of the driving capacitor electrode to the centre of the ground electrode is developed as illustrated in Figure 4.1b. The minimum gap of the electrode is set to 1μm, which is greater than the optical lithography limits in the fabrication process.

Table 4.1: 2D FEM Analysis of IDE Capacitor

Capacitor diameter (μm)	**Width (μm)**	**Gap (μm)**	**Number of gaps**	**Capacitance (pF)**
500	5	5	50	3.974
	5	2	70	7.404
	3	1	124	13.464
	2	1	166	15.535
1000	5	5	99	7.869
	5	2	141	14.915
	3	1	249	27.037
	2	1	333	30.808

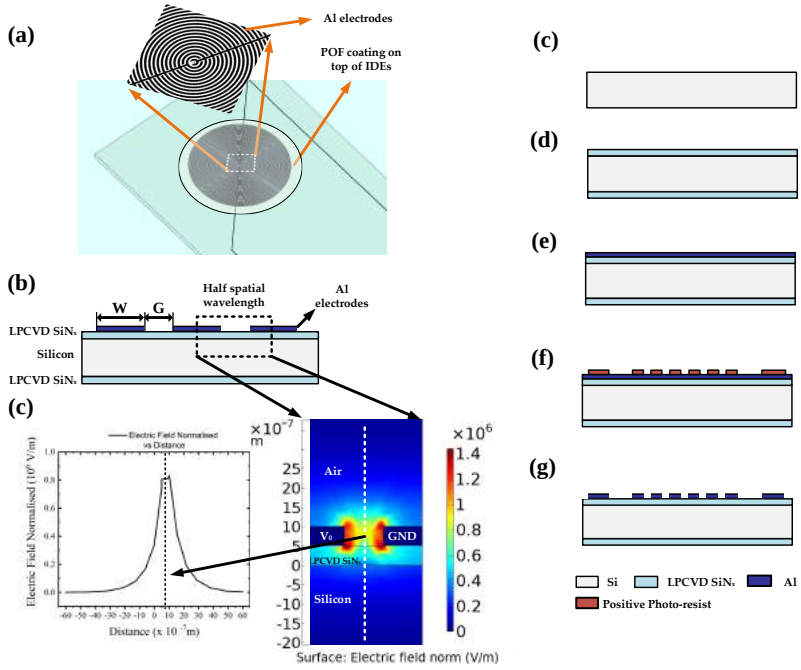

Figure 4.1: (**a**) Schematic illustration of POF coated on a circular aluminum IDE capacitor device. (**b**) Cross-section of the IDE capacitor. (**c**) Finite Element modelling (FEM) of the half spatial wavelength showing surface plot of the electric field and extension of the normalised electric field intensity. Fabrication process flowchart. (**c**) p-type Silicon substrate. (**d**) LPCVD silicon nitride deposition. (**e**) Deposition of 500nnm of Aluminum. (**g**) Patterned aluminium electrodes and resist stripping.

The electrostatic physics module from COMSOL 5.3 multiphysics software is used for the computation of potential and electric field distribution. One electrode of the IDE capacitor is set at potential of 1V and the second electrode is set to ground potential. The relative permittivity of the LPCVD silicon nitride and silicon are defined as $\epsilon_{SiNx} = 7$, $\epsilon_{Si} = 11.9$, respectively[12]. The FEM with electrostatic physics module computes the electric field in the model by solving Gauss's law considering the electric potential V_0 as the independent variable[13]. The total capacitance (C) is calculated using the terminal charge (Q) given by,

$$C = N\frac{Q}{V_0} \tag{4.1}$$

where, N is the number of gaps between the electrodes. The FEM analysis and capacitance calculation is done by varying the parameters of width(W) of the electrodes, gap (G) between the electrodes and the number of gaps (N) between the electrodes with respect to the diameter of the capacitor. The surface plot of the electric field obtained from the FEM analysis for width W

= 2μ and G = 1μm is shown in Figure 4.1c. The normalised electric field is maximum near the edge of the electrodes. The electric field distribution is extended equally to the top surface and bottom surface. The normalised electric field along the line as depicted in line graph at the centre of the gap between the electrodes and extended to a height of 50μm from the electrode surface. It is seen that the about 90% of the normalised electric field is extended up to a height of 3μm from the electrode surface. The capacitance obtained for different parameters of width(W), gap(G) and number of gaps(N) from the 2D FEM analysis is tabulated in Table 4.1. It is seen that the total capacitance increases by increasing the number of electrodes and reducing the gap between the electrodes. The device with capacitor diameter area of 1000μm having W = 2μm and G = 1μm has highest base 30.8pF in air. In order to achieve higher base capacitance in air, IDE capacitor designed with larger capacitor area with diameter with smaller gap between the electrodes can be used.

The fabrication process flowchart is schematically described in Figure 4.1. A 4-inch p-type silicon wafer <100> with a thickness of 300μm is used as the substrate. A layer of low-stress, low pressure chemical vapour deposition (LPCVD) SiN_x of thickness 500nm was deposited at 850°C using a Tempress LPCVD furnace. This is followed by the deposition of 500nm aluminum (Al 1% Si) metal layer using a TRIKON SIGMA sputter coater. The IDEs were patterned by optical lithography using ASML PAS 430 stepper equipment. The Al electrodes are etched by a plasma etching method in a Trikon Omega 201 plasma etcher. The wafer is cleaned with acetone and IPA to remove the photoresist. It is then diced into individual devices in the dimension of 2.5mm by 10mm . The devices are wire-bonded on a 24/40-pin DIP package.

4.2.2. Materials

Melamine (M2659-100GG), Terephthaldehyde (T2207—100G) and Poly(sodium 4-styrenesulfonate) (PSS) (T- 243051) were purchased from Sigma Aldrich and were of 99% purity. Dimethyl Sulphoxide (23500.297) (DMSO, 99.98%) was purchased from VWR.

4.2.3. Synthesis of POF

The synthesis procedure is schematically illustrated in Figure 4.2a. First, melamine and terephtaldehyde were dissolved in DMSO separately by dissolving 25mmol of melamine in 150mL of DMSO and 37.5mmol of terephtaldehyde in 150mL of DMSO respectively. The two solutions were mixed and heated to 50°C for 2 hours to fully dissolve all components, followed by 186°C under reflux conditions for 3 days. The obtained product was filtered and then washed with acetone to remove the unconsumed reactants and the DMSO. The obtained material was dried and stored for further use. The reaction yield was ≈50%.

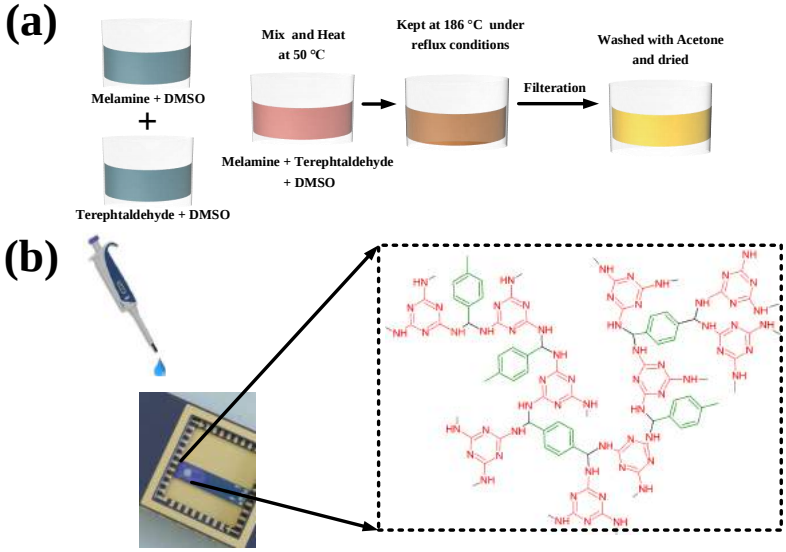

Figure 4.2: Synthesis of POFs and preparation of sensing devices (**a**) Synthesis procedure. (**b**) Illustration of MEMS IDE capacitor and POF coating procedure.

4.2.4. POF coating procedure

The preparation of 4.5 wt% of POF solution was done by dissolving 20.3 mg of POF in 450μl of 1-propanol. The solutions were placed in a ultrasonication bath and mixed for 30 minutes to have good uniform mixture of POF in 1-propanol. A pipette was used to cast 1μl of the dispersed solution on the devices as illustrated in Figure 4.2b. The devices are dried under ambient atmospheric conditions for a day before the gas sensing experiments.

4.2.5. Material Characterization

Scanning Electron Microscopy (SEM) images of the bare device and device coated with POF films were acquired at different magnifications using a JEOL JSM 6010LA microscope. The nitrogen sorption measurements were carried out in a Micromeritics TriStar II 3020 at 77K. The POF surface area determined by Brunauer-Emmet-Teller (BET) method were calculated using the nitrogen adsorption data at 77 K in the relative pressure (P/P_0) range from 0.01 to 0.3, where P_0 was 765 mmHg.

4.2.6. Gas sensing setup

The sensing experiments of the POF coated device with vapors of ethanol, methanol and water was done in a custom-built gas setup schematically illustrated in Figure 4.3. In this system, dry nitrogen was passed through two

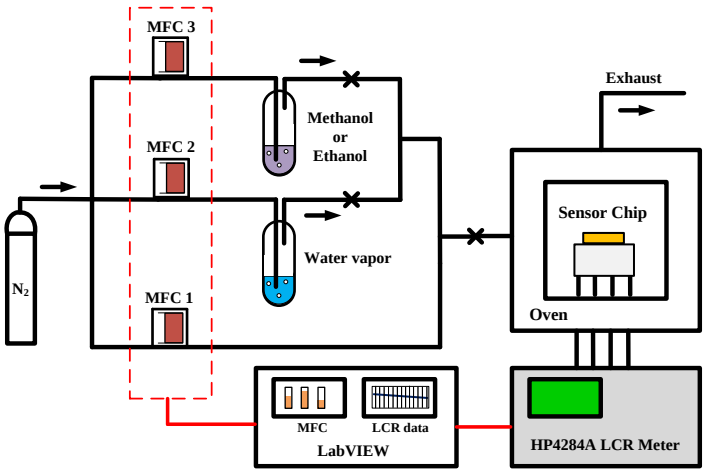

Figure 4.3: Schematic illustration of the gas sensing setup

bubblers containing ethanol, methanol or water vapor (MFC 2, MFC 3) to generate saturated stream of the vapors calculated using the Antoine equation[7]. The vapors were diluted with a parallel stream of dry nitrogen (MFC1) and passed to the gas chamber. A constant flow rate of 200ml/min was maintained during the sensing experiments. A LabVIEW software application was used for controlling the mass flow controllers (MFCs) and data acquisition from HP4284A LCR meter. The capacitance of the devices coated with POF for different concentration of ethanol and methanol vapors were measured at a frequency of 10kHz and voltage of 1V. Before the sensing studies, a preconditioning step was done by passing dry nitrogen at a flow rate of 200ml/min until stabilization of the capacitance of the coated devices was obtained.

4.3. Results and Discussions

4.3.1. Device and Material Characterization

The SEM images of the bare IDE capacitor device are shown in Figure 4.4a and Figure 4.4b. The bare device consists of circular IDEs with width(W) of 2μm and gap(G) of 1μm. The SEM images of the coating of POF on the IDE devices are shown in Figure 4.4c and Figure 4.4d. It is observed that the electrodes are covered with a flaky POF film with good adhesion on the Al electrodes. The POF film is not continuous and there are voids as seen in Figure 4.4c. However, the presence of voids does not significantly affect the sensing measurements as the change in capacitance is mainly influenced by the change in the effective dielectric constant of the sensing film with adsorption of target gas analytes. In an IDE capacitor device, the depth of the fringing electric field lines above the electrodes is proportional to half of the spatial wavelength (λ), where λ = 2*(W + G)[14]. In the current device with W = 2μm and G = 1μm, the

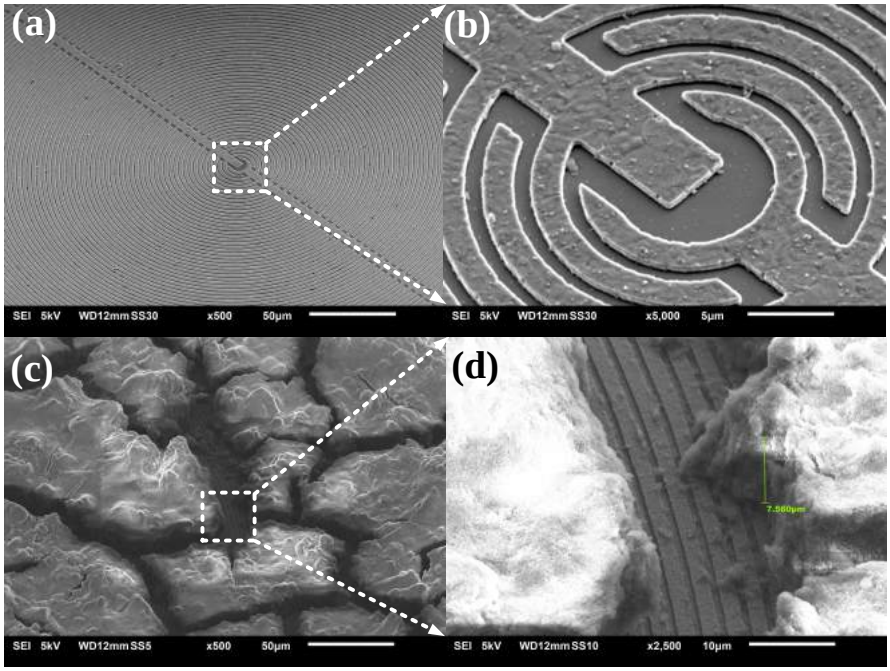

Figure 4.4: SEM Images (**a**) Fabricated device IDE capacitor devices. (**b**) A close-up view of the aluminum IDE electrodes. (**c**) POF coated on the IDE capacitor device coated device. (**d**) A close-up image of POF on top of IDE electrodes with thickness measurement of the POF film.

spatial wavelength $\lambda = 6\mu$m. The measured thickness of the POF layer by SEM on the device is 7.56μm as shown in Figure 4.4d. Thus, the thickness of the POF coating is greater than half of the spatial wavelength ($0.5*\lambda = 3\mu$m) ensuring that the affinity layer is within the electric field of the IDE capacitor.

4.3.2. BET measurements

The adsorption and desorption isotherm of N_2 at 77K of the synthesised POF is shown in Figure 4.5a. It is seen that there is a rapid uptake of N_2 at lower relative pressures ($P/P_0 < 0.3$) indicating the presence of micropores. A hysteresis is seen at relatively high pressures ($P/P_0 > 0.8$) indicating the presence of mesopores in the material. Furthermore, there is a sharp increase seen at higher relative pressures ($P/P_0 > 0.9$) that shows the presence of larger pores. The calculated BET specific surface area of the POF was 722 m^2/g, which is in within the range of specific surface area 640 m^2/g reported earlier[10], but lower than the reported value of 1377 m^2/g for the material synthesised in the first time. The micropore volume determined from the N_2 isotherm plot was 0.158306 cm^3/g. The pore size distribution (PSD) obtained from the N2

adsorption isotherm was calculated using Density Functional Theory (DFT). A plot of pore size distributin (PSD) with increasing pore diameter is shown in Figure 4.5b. The pore diameter obtained from this calculation was found to be in the range from 1 to 30nm. This range shows the presence of micropores to mesopores within the POF layer. This is inline in the earlier reported work indicating the presence of micro to mesopores in the synthesis POF layer[10].

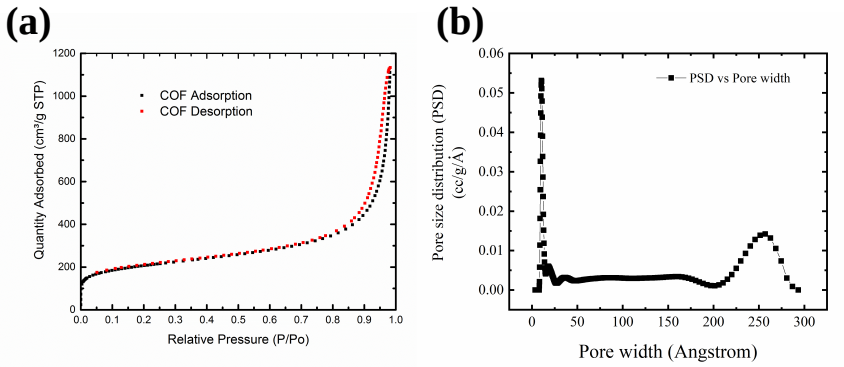

Figure 4.5: (**a**) N_2 adsoprtion and desorption isotherm obtained at 77K (**b**)Plot of Pore sixe distribution versus Pore width using DFT calculations.

4.3.3. Sensing Measurements

The electrical characterisation of the bare device and the device coated with POF by impedance spectroscopy in the frequency range from 100Hz to 100kHz is shown in Figure 4.6a. The device coated with POF has a small increase in the capacitance in comparison to the bare device as shown in Figure 4.6b. The measured impedance (|Z|) of the bare device at 10kHz is 369.104kΩ, whereas the impedance decreases to 358.159kΩ at 10kHz for the device coated with POF. Furthermore, the values of the phase angle (θ) of the device coated with POF is in the range of $-90° < \theta < -87°$ in the frequency range from 100Hz to 100kHz indicating that POF coated device are capacitive in nature.

Sensing measurements of the POF coated device were done for increasing concentration of ethanol and methanol vapors in dry nitrogen from 500ppm to 7000ppm. The capacitance of the device were measured at a constant voltage of 1V and frequency of 10kHz during the exposure to ethanol and methanol vapors. A drift in the baseline of the measured capacitance was observed during the sensing measurements as shown in Supplementary section 1, Figure S 4.1a and Figure S 4.1b) The baseline drift calculation was done and the change in capacitance (ΔC) was determined. The changes in the capacitance (ΔC) for different concentration of methanol and ethanol vapors after baseline drift correction are shown in Figure 4.7a and Figure 4.7b, respectively. The adsorption of methanol and ethanol vapors in the porous framework of the POF film

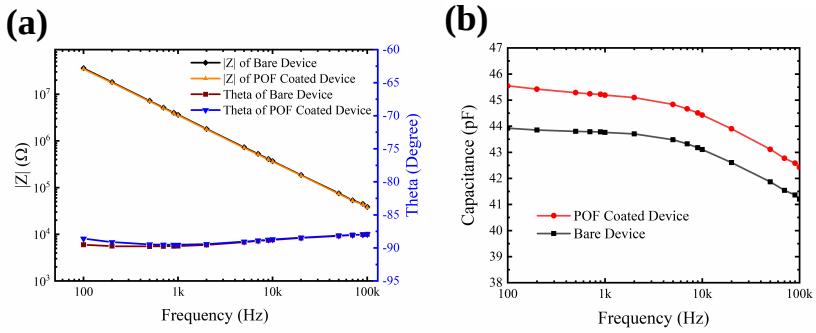

Figure 4.6: (**a**) Impedance and phase angle versus frequency (**b**) Capacitance of bare device and device coated with POF versus frequency.

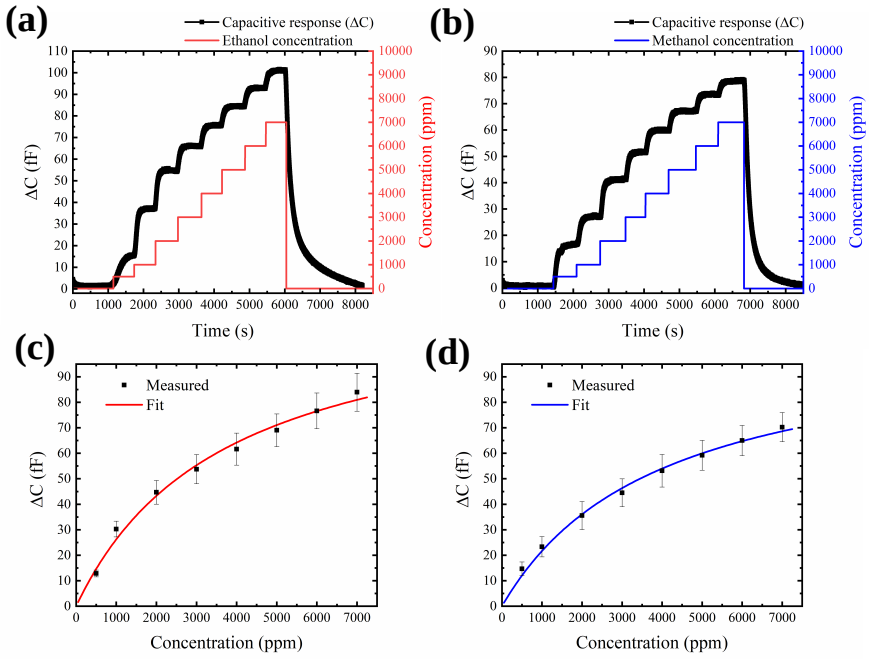

Figure 4.7: (**a**) Sensing response for increasing ethanol concentration from 500ppm to 7000ppm. (**b**)Sensing response for increasing methanol concentration from 500ppm to 7000ppm.(**c**) Calibration curve of change in capacitance versus ethanol concentration with Langmuir adsorption isotherm fit. (**d**) Calibration curve of change in capacitance versus methanol concentration with Langmuir adsorption isotherm fit.

causes changes in the effective dielectric constant in the medium leading to an increase in the capacitance for increasing vapor concentration A calibration

curve for the change in capacitance (ΔC) with concentration of ethanol and methanol vapors from 500ppm to 7000ppm is shown in Figure 4.7c and Figure 4.7d, respectively. The change in capacitance (ΔC) is observed to be linear at lower concentration ranges between 500ppm to 2000ppm but saturates at higher concentration measured upto 7000pm indicating that the maximum adsorption capacity in the POF framework within the concentration is limited. Furthermore, the change in capacitance is found to be higher for ethanol vapors in comparison to methanol vapors in the concentration range from 500ppm to 7000ppm. The average change in capacitance (ΔC) at 2000ppm of ethanol and methanol vapors are 44.68fF and 35.55fF, respectively. The non-linear sensing response for concentration in the range from 500ppm to 7000ppm for ethanol and methanol vapors was fitted with the Langmuir adsorption isotherm model given by[7],

$$\frac{\Delta C}{C_{sat}} = \frac{K_{eq} C_m}{1 + K_{eq} C_m} \tag{4.2}$$

where, C_s indicated the saturation response of the capacitance, K_{eq} is the affinity constant and C_m is the concentration of methanol or ethanol vapors. The values obtained for K_{eq} and C_{sat} for ethanol are 101 bar^{-1} and 131.7fF, respectively. Similarly, the values obtained for K_{eq} and C_{sat} from the Langmuir adsorption model for methanol are 124.14 bar^{-1} and 267.76fF, respectively. The saturation value of the capacitance (C_{sat}) and the affinity constant K_{eq} is much higher for ethanol than methanol vapors in the same concentration range indicating that higher affinity of POF towards ethanol than methanol.

The reversibility tests for 2000ppm of ethanol and methanol vapors in dry nitrogen were performed. The measured capacitance have a drift in the baseline as shown in Supplementary Figure S 4.2a and Figure S 4.2d , respectively. It is seen that the sensor response returns to the initial baseline capacitance in dry nitrogen after exposure to several cycles of the vapors. The resulting change in capacitance obtained after the baseline drift correction for ethanol and methanol vapor concentration of 2000ppm are shown in Figure 4.8a and Figure 4.8b, respectively. This shows that the adsorbed ethanol and methanol vapors in the POF do not cause changes in the dielectric properties of the POF layer, and the adsorbed vapors are completely reversible as the baseline capacitance is recovered.

In the next step, the sensor response was compared to different concentration of ethanol, methanol and watervapor in dry nitrogen. The change in capacitance (ΔC) were normalised with respect to the relative dielectric constant of each analyte (Water = 78, Methanol = 32.7,Ethanol = 24.2). The comparison the normalised change in capacitance $\Delta C/\epsilon_r$ for ethanol, methanol and watervapor in the concentration range from 500ppm to 7000ppm is shown in Figure 4.8c. It is observed from the comparison response that POF film has higher affinity towards ethanol vapors in comparison to methanol and watervapor. This response can be attributed to the stronger interaction of the amine groups present in the POF film towards ethanol vapors than methanol.

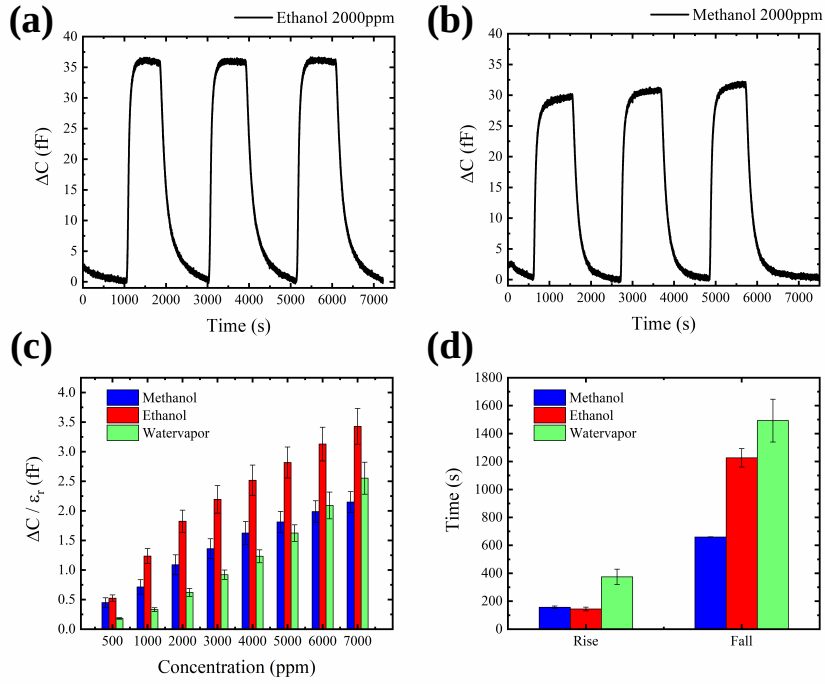

Figure 4.8: (**a**) Reversibility response for ethanol concentration of 2000ppm. (**b**)Reversibility response for methanol concentration of 2000ppm.(**c**) Comparative sensor response normalized with the dielectric constant between methanol, ethanol and water vapor. (**d**) Comparison of sensor recovery and response time for constant concentration of 5000ppm of methanol, ethanol and water vapor.

Next, the response and recovery time of ethanol, methanol and watervapor for concentration of 5000ppm are compared. The response time is defined as the time taken to reach 90% of the saturated capacitance value and the recovery time is defined as the time taken to reach 10% of the baseline capacitance value. The POF film was exposed to a constant concentration of 5000ppm of ethanol, methanol and watervapor in dry nitrogen and the resulting change in capacitance were measured. The rise time and recovery time for each analyte were determined and the comparative response is shown in Figure 4.8d. From, this comparative study it is seen that ethanol vapors are adsorbed slightly faster than methanol and watervapor. However, the recovery time for the vapors are longer than the response time with watervapor taking the most time during the recovery.

Cross-sensitivity tests were performed by adding different concentration of ethanol vapors in the presence of 11500ppm of watervapor ($\approx$ 50% relative humidity). The sensor response showing the change in capacitance for ethanol concentration in the range from 500ppm to 7000ppm in the presence

of 11500ppm of watervapor is shown in Figure 4.9. During the initial phase, the change in capacitance is due to the addition of watervapor until saturation of the capacitance due to watervapor is obtained. In the next phase, the increase in capacitance is observed by the addition of increasing concentration of ethanol. From this cross-sensitivity tests, it is seen that the addition of ethanol does not compete with affinity watervapor within the POF layer and ethanol response is independent in the presence of watervapor.

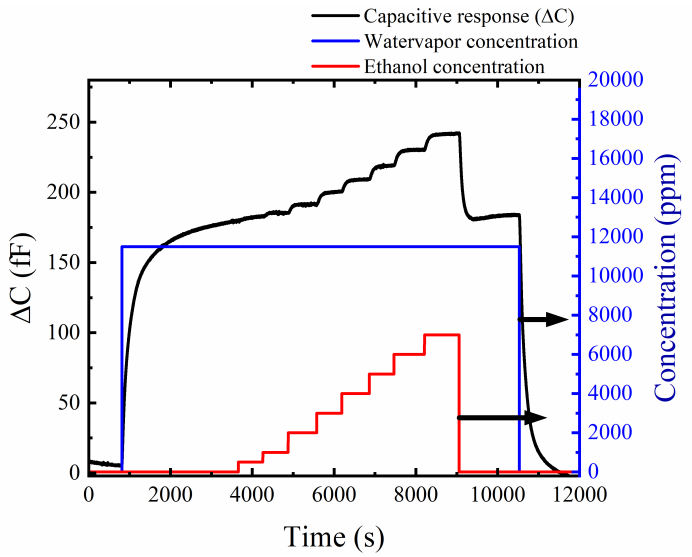

Figure 4.9: Change in capacitance (ΔC) for ethanol concentration in the range of 500ppm to 7000ppm in the presence of 11500ppm of watervapor (≈ 50% relative humidity).

4.3.4. Effect of temperature on the sensing response

To investigate the sensing response of the device coated with POF layer at different temperatures, the device was exposed to a constant concentration of 5000ppm of ethanol, methanol and watervapor in dry nitrogen and the changes in capacitance were measured. The resulting sensing response obtained for the change in capacitance (ΔC) as a function of temperature from 20°C to 50°C is shown in Figure 4.10a. With increasing temperature the change in capacitance decreases indicating that the adsorbed amount of ethanol, methanol or watervapor in the POF layer decreases. The adsorption of the analytes as function of temperature can be further analysed to determine the enthalpy of adsorption of the analytes using the Arrhenius relation given by[15],

$$v = v_0 e^{\frac{-\Delta H}{RT}} \tag{4.3}$$

where, v is the relative change in the capacitance, v_0 is the exponential

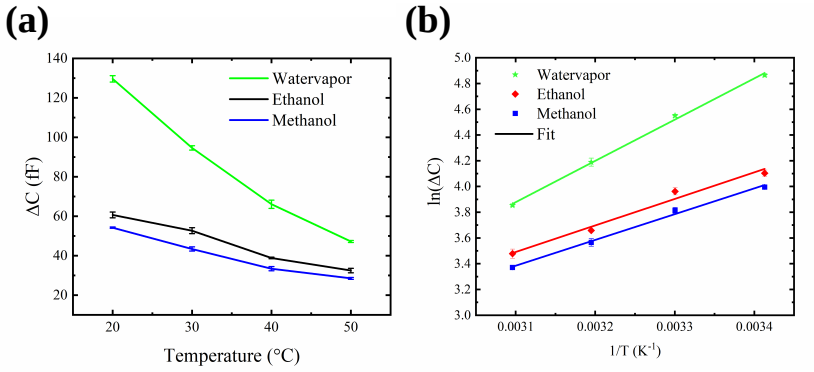

Figure 4.10: (**a**) Comparison of change in capacitance (ΔC) for 5000ppm of ethanol , methanol and watervapor at different temperatures. (**b**) Arrhenius relation of capacitance versus temperature.

constant, R is the gas constant and *(ΔH)* is the difference in the activation energy of the adsorption and desorption process. The Arrhenius behaviour can be further related to the temperature dependent capacitance response given by,

$$\Delta C = C_{max} e^{\frac{-\Delta H}{RT}} \tag{4.4}$$

where, C_{max} represents the equilibrium capacitance and ΔC is the change in capacitance for different concentration of the vapors. A linear fit obtained from the plot of logarithm of ΔC versus temperature (1/T) using is shown in Figure 4.9b. The enthalpy of adsorption *(ΔH)* determined from the fit for ethanol, methanol and watervapor are -17.12kJ/mol, -16.68kJ/mol and -26.67kJ/mol It is seen that the enthalpy of adsorption *(ΔH)* for the analytes have a negative value indicating that the adsorption process is exothermic in nature. Moreover, the enthalpy of adsorption obtained for ethanol and methanol indicate a higher affinity of the POF layer towards methanol and ethanol vapors in comparison to watervapor.

4.3.5. Conclusions

In this study, melamine based porous organic framework (POFs) as affinity layers were coated on aluminum IDE capacitor for investigating the sensing response towards ethanol, methanol and watervapor. FEM modelling of the IDE capacitor electrodes were performed to determine the optimised width and gap of the electrodes within a capacitor diameter of 1μ. Melamine based POF were successfully synthesis by Schiff based chemistry process and layer of 7μm were deposited on the devices. The surface area of the The capacitive sensor response obtained for varying concentration of ethanol and methanol from 500ppm to 7000ppm shows that the sensor has large dynamic concen-

tration range. The comparative study of capacitive response normalised with the dielectric constant of the different analytes shows that POF layer has higher affinity towards ethanol vapors in comparison to methanol and water-vapor. Furthermore, ethanol was adsorbed faster than in the POF network in comparison to methanol and watervapor. Cross-sensitivity measurement of ethanol vapors in the presence of watervapor shows the capability of the independent detection of ethanol vapors in the presence of watervapor. The ability to detect vapors of ethanol and methanol at room temperature shows the application of such POF coated device for low power gas sensor system applications.

4.4. Supplementary Information

4.4.1. Sensing response to ethanol and methanol vapors

The measured capacitance in the POF coated device for increasing ethanol and methanol concentration from 500ppm to 7000ppm is shown in Figure S 4.1a and Figure S 4.1d, respectively. The capacitive response after baseline drift towards ethanol and methanol vapors are shown in After the baseline drift calibration is done, the data for sensing response towards methanol is shown in Figure S 4.1c and Figure S 4.1f, respectively.

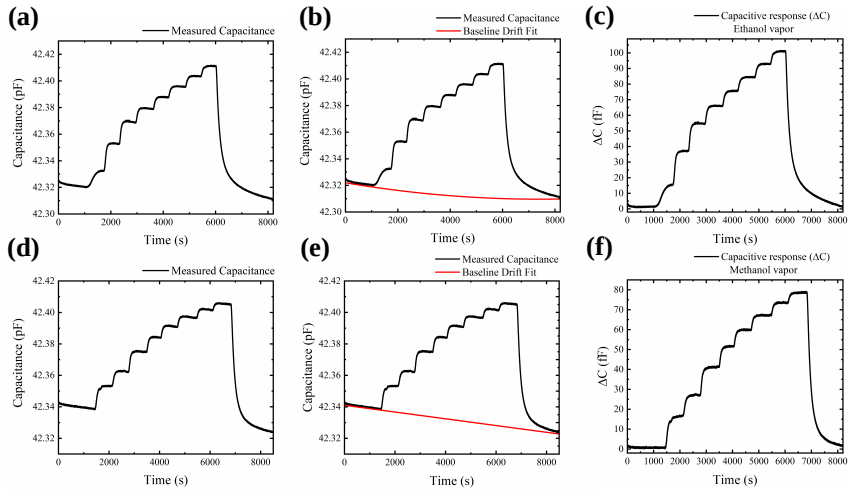

Figure S 4.1: (**a**) Capacitive response for increasing ethanol concentration. (**b**) Baseline drift fit for capacitive response for ethanol vapors. (**c**) Change in capacitance after baseline drift correction for ethanol vapor. (**d**) Capacitive response for increasing methanol concentration. (**e**) Baseline drift fit for capacitive response for methanol vapors. (**f**) Change in capacitance for methanol vapor after baseline drift correction.

4.4.2. Reversibility tests

The capacitive response to repeated cycle of vapors of ethanol and methanol at a constant concentration of 200ppm is shown in Figure S 4.2a and Figure S 4.2d, respectively. The baseline drift correction is done for the measured capacitance and the change in capacitance after baseline drift correction is shown in Figure S 4.2c and Figure S 4.2f for vapors of ethanol and methanol, respectively.

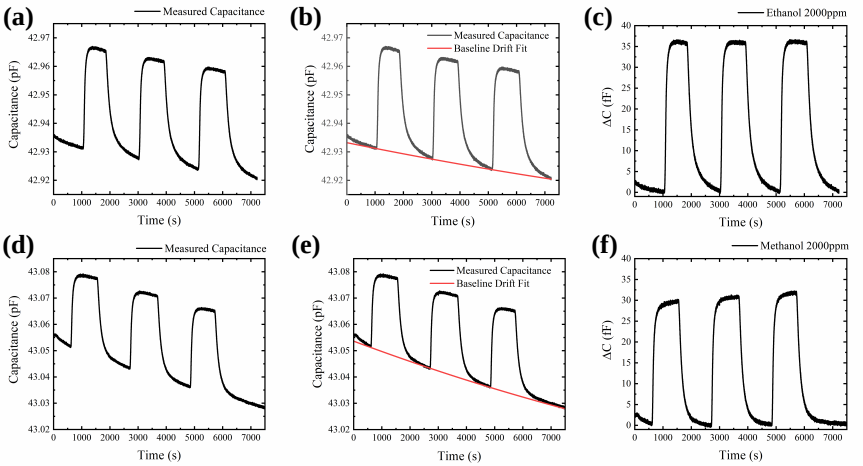

Figure S 4.2: (**a**) Capacitive response for ethanol concentration of 2000ppm. (**b**) Baseline drift fit for capacitive response for ethanol vapors at 2000ppm. (**c**) Change in capacitance after baseline drift correction for ethanol vapors at 2000ppm. (**a**) Capacitive response for methanol concentration of 2000ppm. (**b**) Baseline drift fit for capacitive response for methanol vapors at 2000ppm. (**c**) Change in capacitance after baseline drift correction for methanol vapors at 2000ppm.

References

[1] A. Mirzaei, S. Leonardi, and G. Neri, *Detection of hazardous volatile organic compounds (vocs) by metal oxide nanostructures-based gas sensors: A review,* Ceramics International **42**, 15119 (2016).

[2] S. Patel, T. Mlsna, B. Fruhberger, E. Klaassen, S. Cemalovic, and D. Baselt, *Chemicapacitive microsensors for volatile organic compound detection,* Sensors and Actuators B: Chemical **96**, 541 (2003).

[3] R. Blue and D. Uttamchandani, *Chemicapacitors as a versatile platform for miniature gas and vapor sensors,* Measurement Science and Technology **28**, 022001 (2016).

[4] M. Kitsara, D. Goustouridis, S. Chatzandroulis, M. Chatzichristidi, I. Raptis, T. Ganetsos, R. Igreja, and C. Dias, *Single chip interdigitated electrode capacitive chemical sensor arrays,* Sensors and Actuators B: Chemical **127**, 186 (2007).

[5] F.-P. Steiner, A. Hierlemann, C. Cornila, G. Noetzel, M. Bachtold, J. Korvink, W. Gopel, and H. Baltes, *Polymer coated capacitive microintegrated gas sensor,* in *Solid-State Sensors and Actuators, 1995 and Eurosensors IX.. Transducers' 95. The 8th International Conference on*, Vol. 2 (IEEE, 1995) pp. 814–817.

[6] K. Manoli, D. Goustouridis, P. Oikonomou, S. Chatzandroulis, M. Sanopoulou, and I. Raptis, *Capacitive sensor arrays with controllable deposition of the sensing polymer area for vocs applications: Design and measurement considerations,* Procedia Chemistry **1**, 176 (2009).

[7] S. Sachdeva, S. J. Koper, A. Sabetghadam, D. Soccol, D. J. Gravesteijn, Kapteijn, E. J.R Sudhölter, J. Gascon, and L. C.P.M de Smet, *Gas phase sensing of alcohols by metal organic framework–polymer composite materials,* ACS Applied Materials & Interfaces **9**, 24926 (2017).

[8] J. Boudaden, A. Klumpp, H.-E. Endres, and I. Eisele, *Capacitive co2 sensor,* in *Multidisciplinary Digital Publishing Institute Proceedings*, Vol. 1 (2017) p. 472.

[9] D. Wu, F. Xu, B. Sun, R. Fu, H. He, and K. Matyjaszewski, *Design and preparation of porous polymers,* Chemical reviews **112**, 3959 (2012).

[10] A. Cao, M. Shan, L. Paltrinieri, W. H. Evers, L. Chu, L. Poltorak, J. H. Klootwijk, B. Seoane, J. Gascon, E. J. Sudhölter, *et al.*, *Enhanced vapour sensing using silicon nanowire devices coated with pt nanoparticle functionalized porous organic frameworks,* Nanoscale **10**, 6884 (2018).

[11] M. G. Schwab, B. Fassbender, H. W. Spiess, A. Thomas, X. Feng, and K. Mullen, *Catalyst-free preparation of melamine-based microporous polymer networks through schiff base chemistry,* Journal of the American Chemical Society **131**, 7216 (2009).

[12] M. Madou, *Fundamentals of Microfabrication: The Science of Miniaturization, Second Edition* (Taylor & Francis, 2002).

[13] J. Oberländer, Z. B. Jildeh, P. Kirchner, L. Wendeler, A. Bromm, H. Iken, P. Wagner, M. Keusgen, and M. J. Schöning, *Study of interdigitated electrode arrays using experiments and finite element models for the evaluation of sterilization processes,* Sensors **15**, 26115 (2015).

[14] A. V. Mamishev, K. Sundara-Rajan, F. Yang, Y. Du, and M. Zahn, *Interdigital sensors and transducers,* Proceedings of the IEEE **92**, 808 (2004).

[15] S. Sachdeva, D. Soccol, D. J. Gravesteijn, F. Kapteijn, E. J. Sudholter, J. Gascon, and L. C. de Smet, *Polymer–metal organic framework composite films as affinity layer for capacitive sensor devices,* ACS sensors **1**, 1188 (2016).

5

Tin Oxide (SnO_2) Nanoparticles

Parts of this chapter is part of the manuscript to be submitted - "A facile, rapid and green synthesis of tin oxide nanoparticle thin film produced by Spark Ablation for MEMS ethanol sensor", **Venkatesh, M.R.**; Max Koole; Boyao Zhang; Sumit Sachdeva; Wei, J.; Joost van Ginkel; Bossche, A.; Zhang, G.Q. *MDPI Sensors* , *To be Submitted*

5.1. Introduction

Volatile Organic Compounds (VOCs) are organic compounds present in the gas phase in indoor air at ambient temperature and humidity conditions. VOCs are emitted from building materials, paints, washing liquids, wooden floors commonly found in houses, offices, restaurants, and malls[1]. VOCs deteriorate the quality of air leading to indoor air pollution. The long-term exposure of VOCs in indoor environments can cause sick building syndrome(SBS) and building-related illness(BRI). Indoor air quality monitoring can help identify sources, proper ventilation management, and minimize building-related illness[2]. Among the VOCs identified in the indoor air, ethanol is one of the most common organic compounds emitted from household items such as cosmetics, paints, and dish washing liquids. Ethanol is a colorless transparent liquid having a boiling point of 78.3°C. The threshold limit value(TLV) for repeated exposure to ethanol without causing significant health effects is 1000ppm. Long-term exposure to ethanol vapor above the TLV can cause dizziness, fatigue and nausea[3]. Thus, detecting and monitoring ethanol concentration in homes and offices is helpful for people to obtain a better healthy indoor air quality.

In chemi-resistive based gas sensors, the gas concentration are determined by measuring the change in the electrical resistance of the sensing material on exposure to the gas. For example, metal oxides such as SnO_2, CuO, ZnO, In_2O_3 are used as sensing materials for measuring ethanol vapors in several studies[4][5][6]. Among these metal oxides, SnO_2 is one of the most extensively studied materials due to several advantages such as sensitive and stable response towards reducing gases such as ethanol, cost-effective synthesis, and thermal stability[7]. In a thick-film SnO_2 based sensors, the gas molecules cannot penetrate the layers and the interaction of the gases occurs only at the surface sites available at the geometric boundary of the layer. However, by reducing the grain size of SnO_2 materials, the number of active sites for the adsorption of gas molecules can be increased[8]. The sensitivity is also known to be related to the depth of the space charge region (L) formed at the surface of the SnO_2 nanoparticles layer having a grain size (D). The sensitivity can be improved when the particle size (D) is approximately two times the values of the depth of space charge region ($D \approx 2L$)[9]. Thus, the development of nanostructures and nanoparticles thin film of SnO_2 provides a good direction towards improving the sensor performance such as sensitivity, selectivity ,and response time.

SnO_2 nanoparticles are synthesized by liquid phase, solid-phase and vapor-phase methods. Liquid-phase methods include sol-gel process, hydro thermal, microwave irradiation, sonochemical and microemulsion process; solid-phase method include, mechanical grinding and ball milling process, and vapor-phase based synthesis are done by flame spray pyrolysis, laser ablation, and spark discharge[10]. In comparison to liquid-phase and solid-phase methods, vapor-phase based synthesis of SnO_2 nanoparticles has advantages such as reduced contamination of the nanoparticles due to impurities, utilising non-toxic or-

ganic solvents, reduced waste generation, continuous and flexible processing of nanoparticles than batch-wise process[10][11]. In this study, vapor-based synthesis of SnO_2 nanoparticles using the spark discharge method is discussed. A spark generator used for the spark discharge synthesis of nanoparticles consists of two opposing metal or metal oxide electrodes with a diameter in the range of 3mm to 6.35mm and separated by a few millimeters. The electrodes are placed in a closed chamber connected to a high voltage power supply and a variable parallel capacitor having a maximum capacitance of 20nF. A stream of inert gas is passed into the chamber at a flow rate of 0.8-1lpm. As the voltage across the electrodes is increased, a spark discharge is initiated due to the breakdown of the inert gas molecules. This results in the evaporation of the electrode material within the vicinity of the spark. The cooling of the vapor cloud is fast since the vapour cloud is small compared to the evaporation-condensation process resulting in the production of a large number of nanoparticles[11][12]. The spark discharge method enables the formation of nanoparticles with high purity since only the electrode material that forms the nanoparticle is heated during the process. Along with this, the spark discharge method allows the controlled synthesis of various sizes of nanoparticles, enables direct deposition on the substrate and devices, and reduces the wastage of source materials.

In recent studies, there has been a growing interest in synthesizing metal oxide nanoparticles by spark discharge method for gas sensing applications[13–16]. Tungsten oxide (WO_x) nanoparticles synthesized using spark discharge show sensitive and reversible responses to 1ppm of NO_2 at 200°C[13]. SnO_2 nanoparticles with particle sizes in the range of 15-20nm processed by gas-phase spark discharge synthesis show sensitive and fast response to H_2 at 100ppm with reduced sensitivity to watervapor[14]. The spark discharge synthesis method also allows the ability to deposit the nanoparticle thin film on the devices directly. In the previous studies discussed, SnO_2 and WO_x nanoparticles synthesized with spark discharge method are mainly deposited on custom devices such as gold electrodes on ceramic substrate or Pt based resistive heater with sensing electrodes fabricated on a ceramic substrate for studying the sensing response at high temperatures[13][14]. Metal-oxide materials such as SnO_2 films exhibit sensing response upon exposure to gases in the operating temperature ranges of 300°C to 500°C. SnO_2 based gas sensors thus require a heating element along with sensing electrodes for measuring changes in resistance on exposure to gaseous analytes at higher operating temperatures. In commercially available Taguchi gas sensors, Pt/Tungsten-based resistive heating elements fabricated on a ceramic substrate together with SnO_2 coated sensing electrodes are used for gas sensing applications. The disadvantage of using resistive heating elements on a ceramic substrate is higher power consumption, non-uniform temperature distribution, and limited chip integration of readout electronics[17]. The development of devices using silicon MEMS technology enables integration of both sensing electrodes and resistive heating element(termed as microhotplate) on the same chip. Furthermore, microhotplate developed using silicon MEMS technology have benefits such as,

thermal isolation capability between the active sensing area and the substrate using suspended membrane structures, achieving lower power consumption, and on-chip integration of electrical readout circuits[17][18].

5.2. Experimental

5.2.1. Device Design

In this work, a microhotplate with TiN/Mo/TiN as the metal stack is fabricated on a suspended membrane type structure using a silicon-on-insulator(SOI) substrate. A schematic illustration and cross-section of the device are shown in Figure 5.1a and Figure 5.1c, respectively. A p+ epitaxial silicon layer of 50μm thickness on a buried oxide is used as the substrate material. The SnO_2 nanoparticles are deposited using a spark discharge equipment and an impaction chamber containing a nozzle to direct the nanoparticles in the aerosol phase to the substrate. The diameter of the nozzle limits the area of deposition of SnO_2 nanoparticles. A large area in the range of 1mm-2.5mm on the device is required to have a uniform deposition of SnO_2 nanoparticles film on the active region of the sensor. Due to this limitation, the active region of the microhotplate is larger, having a diameter of 1.5mm is developed. The dimension of the microhotplate is larger than a typical microhotplate device having diameter of 0.5mm to 1mm. A circular microhotplate consisting a of a stack of TiN/Molybdenum/TiN metal film deposited and patterned on a thermal oxide layer, as shown in Figure 5.1a. The sensing electrodes are patterned at the center of the circular microhotplate. Microhotplate with TiN and molybdenum as the metal layer show good stability for high-temperature operation up to 700°C, and thus, it is preferred choice of microhotplate metal layer used in this work[19][20]. The active region with the microhotplate is suspended using silicon beams as support to the substrate by etching the front and backside of the silicon. The silicon beams function as a heat-spreading layer and mechanical support to the microhotplate active area. PECVD SiO_2 as a passivisation layer is deposited on the microhotplate electrodes, and contact pads are opened to deposit platinum probe contacts to the sensing electrodes, as shown in the layout in Figure 5.1c. A similar configuration of the microhotplate device with platinum probe contacts was used for the time-resolved X-ray diffraction study of the sintering process of Cu nanoparticle paste[21]. The microhotplate coated with Cu nanoparticle operated at 200°C enabled the study of reduction of Cu_8O and Cu crystallisation in the sintering process within an interval of 1s. The current device structure developed is an improved version based on the previous work for the study of time-resolved XRD of nanoparticles and gas sensing response of thin-film nanoparticles[21][22].

A 3D finite element model(FEM) of the device is developed in COMSOL Multiphysics® 5.3 for evaluating the temperature distribution of the proposed design and structure. The device area has a diameter of 1.5mm with a 50um thick silicon layer below the microhotplate area. The circular design of the microhotplate layout as shown in Figure 5.1c with a metal stack of 300nm molybdenum/TiN on a 1μm thermal oxide layer is added in the model. The

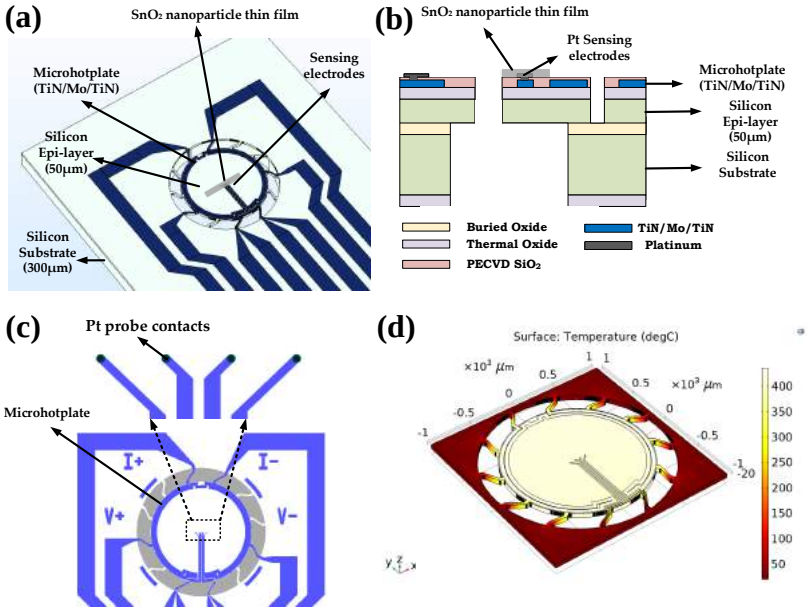

Figure 5.1: (**a**)Schematic illustration of the MEMS microhotplate with SnO_2 nanoparticle film depsoited on the sensing electrodes. (**b**) Cross-section view of the device. (**c**) Patterned 300nm TiN/Mo/TiN microhotplate on the front side of the wafer. (**d**) Patterned 300nm TiN/Mo/TiN microhotplate on the front side of the wafer

material parameters used in the COMSOL multiphysics module for the electro-thermal analysis of the device is shown in the Table 5.1. The heat transfer physics is defined on the entire model. This module is coupled to the electric current physics module defined for the microhotplate and sensing electrodes. The temperature co-efficient of resistance(TCR) for the TiN and Mo film used in the model are $\alpha_{TiN} = 0.01425°C^{-1}$ and $\alpha_{Mo} = 0.001216°C^{-1}$ respectively[19][20]. The heat transfer due to convection is defined on the entire domain with convective heat transfer co-efficient in the range of forced convection of gases given by, $h_{conv} = 100\ Wm^2K^{-1}$ [23]. The input current to the microhotplate is varied in the range from 40mA to 90mA.

Table 5.1: Material parameters used for the COMSOL FEM simulation[17][24].

Material	Thermal Conductivity (k) W/mK	Density Kg/m3	Heat Capacity (Cp) J/kgK
Silicon	157	2320	700
Thermal Oxide	1.4	2200	730
TiN	19.2	5220	600
Mo	138	1022	250

The surface plot of the temperature distribution across the active region of the microhotplate obtained from the FEM simulation is shown in Figure

5.1d. The temperature is found to be uniform within the circular area of the microhotplate. However, the temperature is higher at the metal patterns close to the edge of the active area. The average temperature for an input current of 75mA is 411.81°C. This is within a deviation of 5.67% from the centre to the edge of the active region. The silicon beams show a gradient of temperature distribution from the high-temperature active region to the low-temperature substrate. The results of the average temperature and deviation from the FEM simulation are shown in Table 5.2. The deviation in temperature distribution increases with the increase in the average temperature ranges. For sensing experiment with SnO_2 nanoparticles developed in this study, the temperature distribution in the active region close to the sensing electrodes is uniform around 400°C.

Table 5.2: Temperature distribution analysis of microhotplate by FEM simulation.

Average Temperature (°C)	**Max Temperature (°C)**	**Min Temperature (°C)**	**Deviation**
90.65	92.85	90.06	0.99%
142.23	146.05	141.21	1.73%
217.12	223.31	215.45	2.81%
324.88	334.50	322.27	4.38%
411.81	424.26	408.43	5.67%
589.51	607.85	584.51	8.37%

5.2.2. Device fabrication

The process steps for the device fabricated in this study are shown in Figure 5.2. A 4 inch p-type <100> silicon-on-insulator(SOI) wafer with silicon thickness 300μm, and 50μm (p+) epitaxial silicon on a 2μm oxide (BOX) is used as the starting material (Figure 5.2a). In the next step, thermal oxide is grown by wet oxidation process and a metal stack of TiN/Mo/TiN with a thickness of 50nm/200nm/50nm respectively is deposited on the front side of the wafer. The TiN/Mo/TiN microhotplate is patterned and etched by a plasma etching process using a Trikon Omega 201 plasma etcher. An isolation layer of 1μm of PECVD SiO_2 is deposited on top of the TiN/Mo/TiN electrodes (Figure 5.2b - Figure 5.2d). The front side and back side of the silicon is patterns and etched by deep reactive silicon etching (DRIE) Bosch process (Figure 5.2e). The buried oxide layer (BOX) at the backside of the wafer is removed by protecting the front side of the wafer by photoresist to obtain a suspended 50μm thick silicon structure (Figure 5.2f). The contact pads to the microhotplate metal and the sensing electrodes are opened by etching PECVD SiO_2 layer (Figure 5.2g). A 200nm platinum thin film is deposited at the contact pad areas by evaporation and lift-off method (Figure 5.2h). The wafers are cleaned and diced into devices having a dimension of 5mm in width and 10mm in length. The devices are packaged in a 40pin DIP packages.

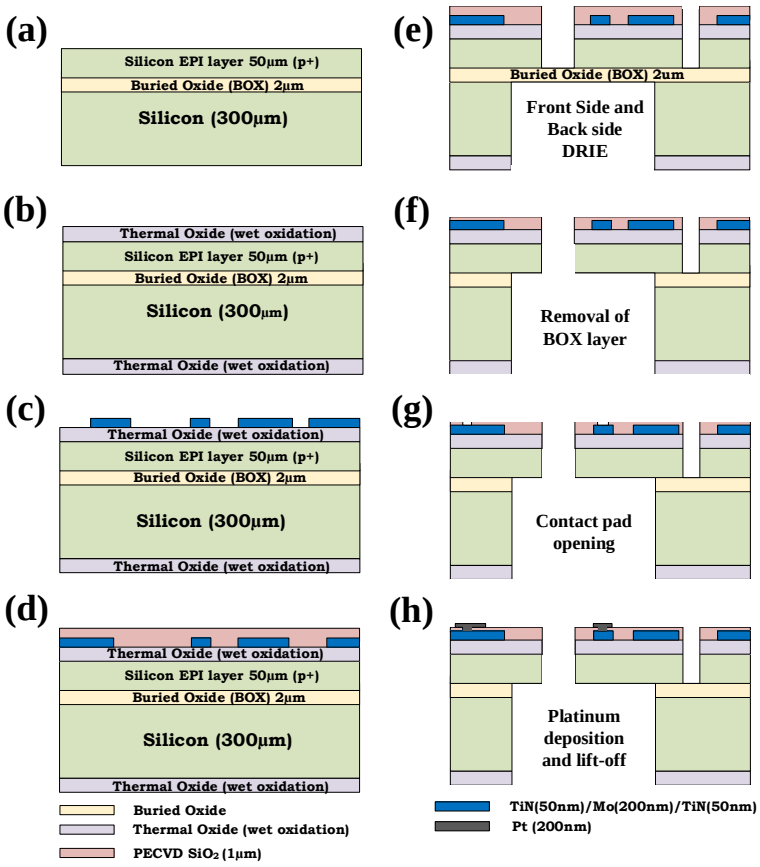

Figure 5.2: Device fabrication process flowchart (**a**) Silicon on Insulator(SOI) substrate with 50μm p+ epilayer and 2μm of buried oxide(BOX) layer. (**b**) Thermal oxide by wet oxidation. (**c**) Patterned 300nm TiN/Mo/TiN microhotplate on the front side of the wafer. (**d**) 1μm PECVD silicon oxide deposition on front side of the wafer. (**e**) DRIE on front and backside of the wafer. (**f**) Wet etching of BOX layer. (**g**) Contact opening for the pads. (**h**) Platinum deposition (200nm) and lift-off.

5.2.3. Synthesis of Tin oxide (SnO_2) nanoparticles

A schematic illustration of the synthesis and deposition of SnO_2 nanoparticles on the fabricated microhotplate devices using a commercial spark discharge equipment from VSP-G1 Nanoparticle Generator from VSPARTICLE B.V[25] is shown in Figure 5.3. In this setup, the spark chamber consists of two high purity tin(Sn) electrodes placed opposite and close to each other are connected to a high-voltage power supply in parallel to a capacitor having a maximum capacitance of 20nF. The inlet of the spark chamber is connected to oxygen gas cylinder(2% oxygen in nitrogen), and it is passed into the chamber as the carrier gas at a constant flow rate of 1.2lpm. The sparks created in

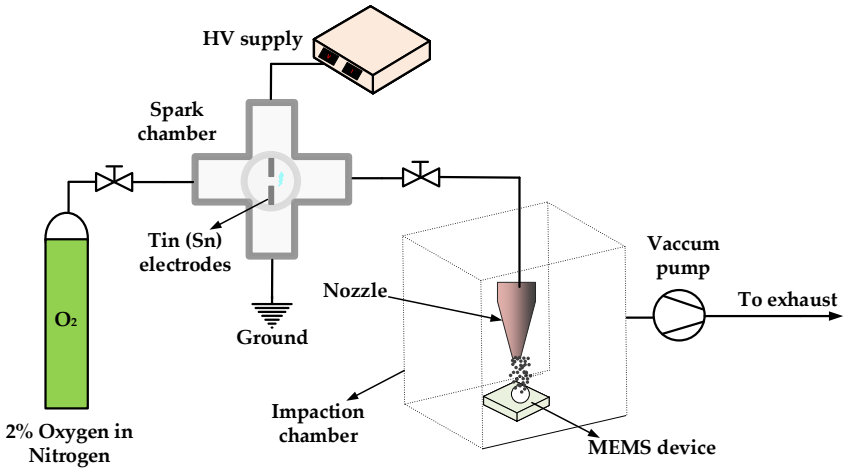

Figure 5.3: Schematic illustration of the synthesis of SnO_2 nanoparticles and preparation of sensing devices.

the vicinity of the two electrodes during the discharge process, typically in the duration of microseconds, vaporize the electrode material. A constant current of 3mA applied from the high voltage source periodically recharges the capacitor after discharge occurs at the breakdown voltages[11][12]. The vapor cloud formed during the spark discharge process is cooled rapidly by the gas flow passing through the gap between the electrodes. This results in the formation of SnO_2 atomic clusters by nucleation that grows into SnO_2 nanoparticles by vapor condensation and coagulation. The aerosol containing SnO_2 nanoparticles is passed to an impaction chamber that contains a nozzle to deposit the nanoparticles on the device. The nozzle is controlled by a stepper motor that accurately allows positioning and deposition of the SnO_2 nanoparticles on the active area of device. The movement speed of the nozzle is varied to optimise the thickness of the SnO_2 nanoparticle thin film.

5.2.4. Device and Material characterization

Transmission electron microscope (TEM) images of the as-synthesized SnO_2 nanoparticles placed on TEM copper grids were acquired using JEOL JEM-1400 plus TEM microscope. Scanning electron microscope (SEM) images of the SnO_2 nanoparticle thin film were acquired using a JEOL JSM-6010LA SEM microscope. X-ray diffraction (XRD) of the as-synthesized and annealed SnO_2 nanoparticle thin film deposited on a silicon (100) substrate were done using Bruker D8 Advance diffractometer with Cu Kα radiation source. XRD measurements were done at 2θ angles in the range 20° - 60° with 2° offset, a step size of 0.033°, and a 6s counting time per step. The thickness of the deposited SnO_2 nanoparticle film on silicon substrate was measured using a

Dektak profilometer. The electrical characterisation of the microhotplate devices in the temperature range 20°C to 200°C were done using a Thermochuck temperature controller and Agilent 4156C parameter analyzer. The resistance of the devices obtained at different temperature was used to extract the temperature coefficient resistance (TCR) of the devices.

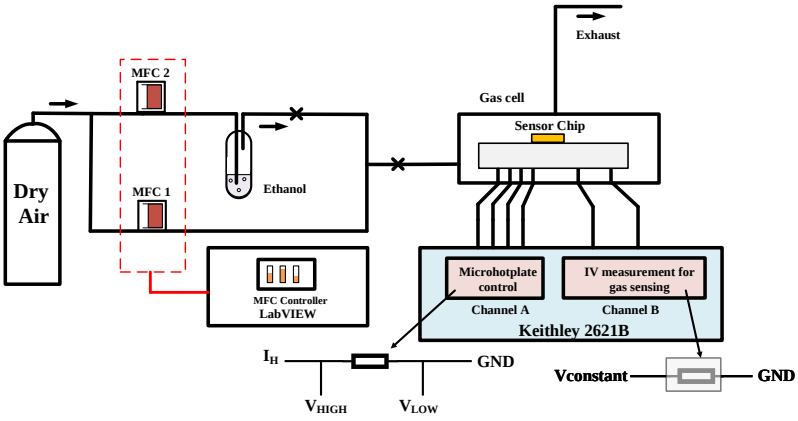

Figure 5.4: Schematic of the gas sensing setup

5.2.5. Gas sensing setup

The sensing response of the deposited SnO_2 nanoparticle film on the MEMS device towards ethanol vapors was done in a custom gas test setup, as shown in Figure 5.4. In this setup, dry air was passed through a bubbler to generate ethanol vapors, and this vapor was diluted with a parallel stream of dry air to obtain the desired concentration of ethanol vapors. The ethanol vapors with the desired concentration was passed to the gas cell at a constant rate of 200mL/min using a LABVIEW program controlling the respective mass flow controllers(MFCs). A two-channel Keithley 2621B source measurement unit(SMU) was used for the DC IV measurements. Channel A of the SMU was used to apply a constant power to obtain the desired temperature of the microhotplate. Channel B of the SMU was connected to the sensing electrode and a 2-probe I-V measurement was done. A constant voltage was applied to the sensing electrodes and the resulting changes in the current were measured upon exposure to various concentrations of ethanol vapor.

5.3. Results and Discussions

5.3.1. Particle size and crystal structure

The TEM images of the as-deposited SnO_2 nanoparticles placed on a TEM grid is shown in Figure 5.5a. It can be seen from the TEM images that the SnO_2 nanoparticles formed by spark discharge synthesis method mainly consist of agglomerates consisting of primary particles. The selected area diffraction

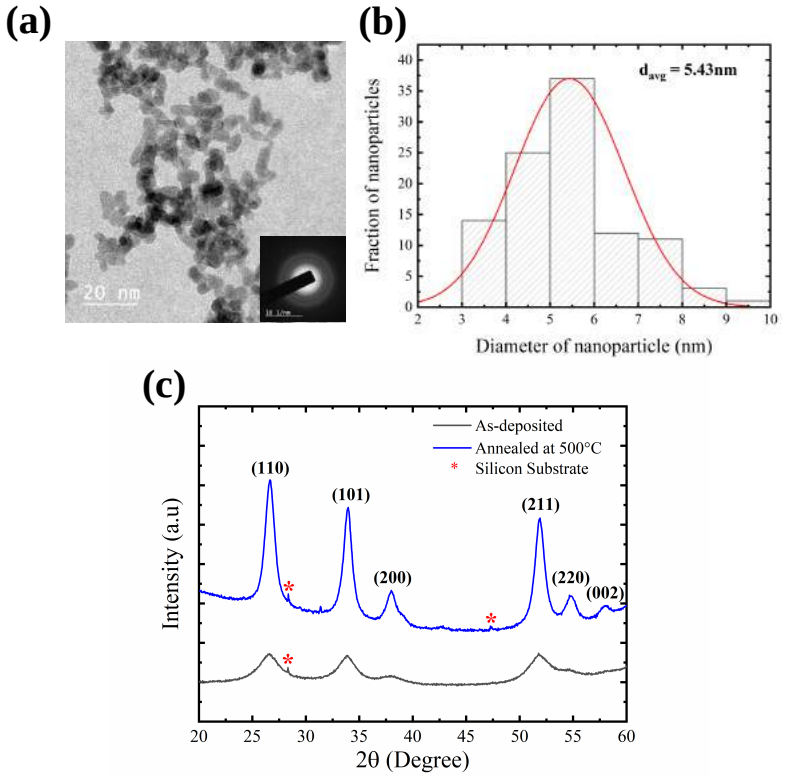

Figure 5.5: (**a**) TEM Image and SAED pattern(inset) of as-deposited SnO_2 nanoparticles. (**b**) particle size distribution of as-deposited SnO_2 nanoparticles. (**c**) XRD pattern of the as-deposited and annealed SnO_2 nanoparticles.

pattern (SAED) in the inset of Figure 5.5a shows that the synthesized SnO_2 nanoparticles are crystalline in nature. The particle size distribution obtained from the TEM from the analysis of TEM images is shown in Figure 5.5b. From the histogram data, it is seen that the range of the size of SnO_2 nanoparticle particles is around 4nm to 6nm, with an average particle size of 5.43nm.

The XRD analysis of the SnO_2 nanoparticle film deposited on a silicon (100) substrate for the as-deposited and SnO_2 nanoparticles annealed at 500°C for 2 hours is shown in Figure 5.5c. The XRD peaks are identified by comparison with the JCPDS database. From this graph, the characteristic peaks for the annealed thin film for (110), (101), (200), (211), (220) ,and (002) planes are located at 2θ = 26.6, 33.9°, 38°, 51.8°, 54.8° and 57.9° respectively. The peaks obtained are in agreement with the JCPDS standard SnO_2 XRD peak(card number 00-041-1445). The XRD data analysis confirms that the SnO_2 nanoparticle film synthesized by the spark discharge method in this study is crystalline in nature. Furthermore, it can be seen that XRD peaks of

the as-deposited film are broader, whereas the XRD peaks of annealed SnO_2 film are higher in intensity and sharper. The peak sharpening shows that the crystallite size of SnO_2 nanoparticles increases after the annealing process [26].

5.3.2. Morphology of thin film SnO_2 nanoparticles

The deposition of SnO_2 nanoparticle thin film on a silicon substrate is done by positioning and controlling the movement speed of the nozzle close to the substrate. The SEM images of the as-deposited SnO_2 nanoparticle films at room temperature for different movement speeds of the nozzle are shown in Figure 5.6. Figure 5.6a to Figure 5.6d shows the SEM images of the deposited nanoparticle film with increasing speed of the nozzle set to 0.2mm/min, 0.35mm/min, 0.6mm/min, and 1.1mm/min. The thickness of the deposited nanoparticle film measured using a dektak profilometer for different movement speed is tabulated in Table 5.3. It can be seen that the thickness of the nanoparticle film decreases by increasing the movement speed of the nozzle. The thin films deposited at 0.2mm/min have an average thickness of 10μm, whereas thin films deposited at 0.6/min have a thickness of 3μm. Furthermore, comparing the SEM images from Figure 5.6a to Figure 5.6d, it can be seen that nanoparticle film deposited at 0.2mm/min have large cracks laterally and deeper into the film, but the cracks on the film reduce with an increased movement speed of the nozzle. The formation of cracks during the deposition of nanoparticle films on the substrate occurs due to mechanical stress induced by the bombardment of nanoparticles on deposited layers, cohesive forces between nanoparticles closing the voids, and deformation of the crystallites[13]. Figure 5.6e and Figure 5.6f are the SEM images of nanoparticle film deposited with a nozzle movement speed of 0.6mm/min and 1.1mm/min for three cycles, respectively. The sample deposited at a nozzle movement speed of 0.6mm/min has a thickness of 7μm but with large cracks visible as seen in the SEM image Figure 5.6e. However, the sample deposited with a nozzle movement speed of 1.1mm/min has a thickness of 3μm with reduced cracks in the film (Figure 5.6f). Thus, the deposition of the nanoparticle film with multiple cycles at higher movement speed of the nozzle increases the thickness and reduces crack formation in the film.

Table 5.3: Deposition parameters of SnO_2 nanoparticles film by spark discharge method.

Nozzle speed during deposition (mm/min)	**Thickness (μm)**	**Morphology analysis by SEM**
0.2	10	Visibility of large cracks in the film
0.35	5	Visibility of cracks in the film
0.6	3	Less cracks visible in the film
0.6 (3 cycles)	7	Visibility of cracks in the film
1.1 (3 cycles)	3	Less cracks visible in the films

In the next step, the samples were annealed in air at 500°C for 2 hours, and the SEM images of the annealed samples are compared with as-deposited nanoparticle film as shown in Figure 5.7. Figure 5.7a and 5.7b are the SEM images of the as-deposited and annealed film, deposited at 0.6mm/min for

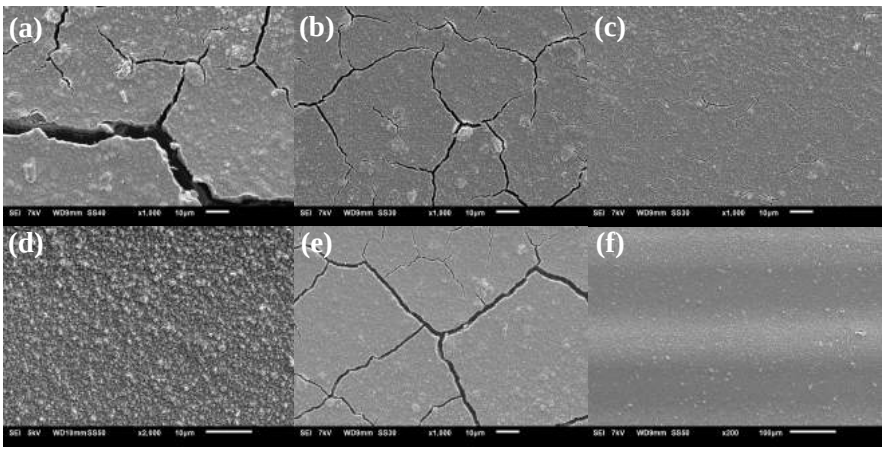

Figure 5.6: SEM image of thin film of SnO_2 nanoparticle with different deposition parameters (**a**) 0.2mm/min. (**b**) 0.35mm/min. (**c**) 0.6mm/min. (**d**) 1.1mm/min. (**e**) 0.6mm/min for 3 cycles. (**f**) 1.1mm/min for 3 cycles.

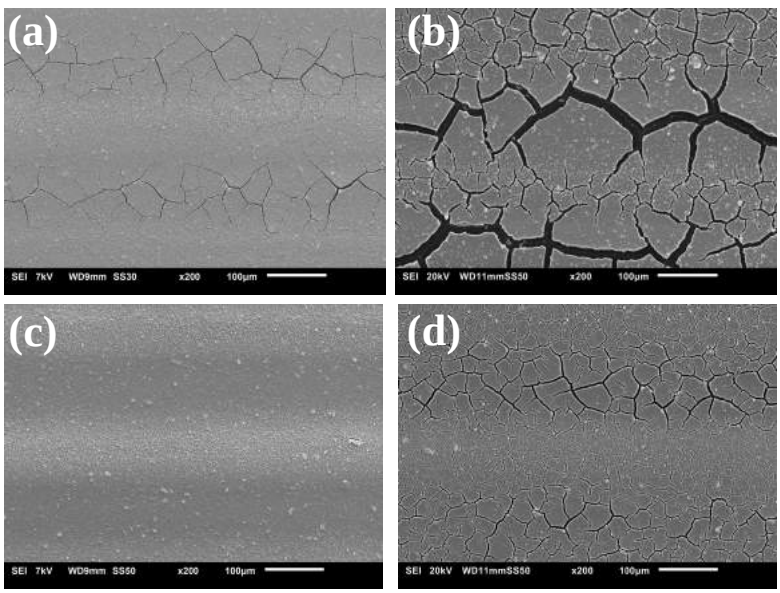

Figure 5.7: SEM image of thin film of SnO_2 nanoparticles as-deposited (left column) and annealed at 500°C for 2 hours in air (right column). (**a**) as-deposited SnO_2 nanoparticles at 0.6mm/min for 3 cycles. (**b**) Annealed SnO_2 nanoparticles film (0.6mm/min for 3 cycles). (**c**) as-deposited for 1.1mm/min for 3 cycles. (**d**) Annealed SnO_2 nanoparticles film (1.1mm/min for 3 cycles)

three cycles, Figure 5.7c and 5.7d are the SEM images for samples deposited at 1.1mm/min for three cycles. The sample deposited at a nozzle movement speed of 0.6mm/min (three cycles) having a thickness of 7μm shows large growth in cracks after annealing(Figure 5.7b). The growth of cracks across the film is found to be less in the film deposited at a nozzle movement speed of 1.1mm/min(three cycles) with a thickness of 3μm, as shown in Figure 5.7d. The increase in the crack occurs due to thermal expansion and an increase in the residual stress in the film. Furthermore, the sintering of the nanoparticles at higher temperatures results in the shrinkage of the material and the widening of the cracks. The large cracks can cause discontinuity in the electrode to film contacts, thereby increasing the overall resistance of the film. Thus, a nanoparticle thin film with a minimised crack formation and sufficient thickness are preferred for the deposition on the sensing devices. The nozzle movement speed parameter at 1.1mm/min for three cycles was subsequently used for the deposition of SnO_2 nanoparticles on the device with a microhotplate integrated with sensing electrodes.

The SEM image of the bare device consisting of a circular TiN/Mo/TiN microhotplate with sensing electrodes is shown in Figure 5.8a. The active region with the microhotplate is suspended by the silicon beams across the circular area, as shown in Figure 5.8a. The device was placed inside the impaction chamber of the spark discharge equipment for the deposition of the synthesized SnO_2 nanoparticles. A control program was developed to accurately place the nozzle at the top of the active region of the device. SnO_2 nanoparticles were deposited to cover the sensing electrode area having Pt contact pads. The SEM image of the device coated with SnO_2 nanoparticle film is shown in Figure 5.8b. It can be seen that the SnO_2 nanoparticle film forms a uniform layer at the center of the active area covering the sensing electrodes.

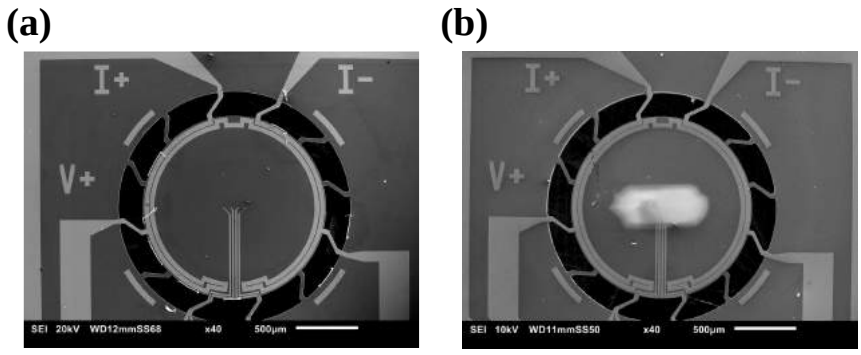

Figure 5.8: (**a**) Bare Device. (**b**) Device-coated with SnO_2 nanoparticle thin-film.

5.3.3. Gas sensing study

In this section, the device coated with SnO_2 nanoparticle film is tested for the sensing response to ethanol in the concentration range from 100ppm to 1000ppm. In the first step, the temperature coefficient of resistance (TCR) of the fabricated TiN/Mo/TiN microhotplate device is done. The sensing response of the device at different temperature is done to obtain the operating temperature of the sensor. Finally, the sensing response for the varying concentration of ethanol vapors, response and recovery time of the sensor, and selectivity studies with methanol and ethanol vapors is discussed.

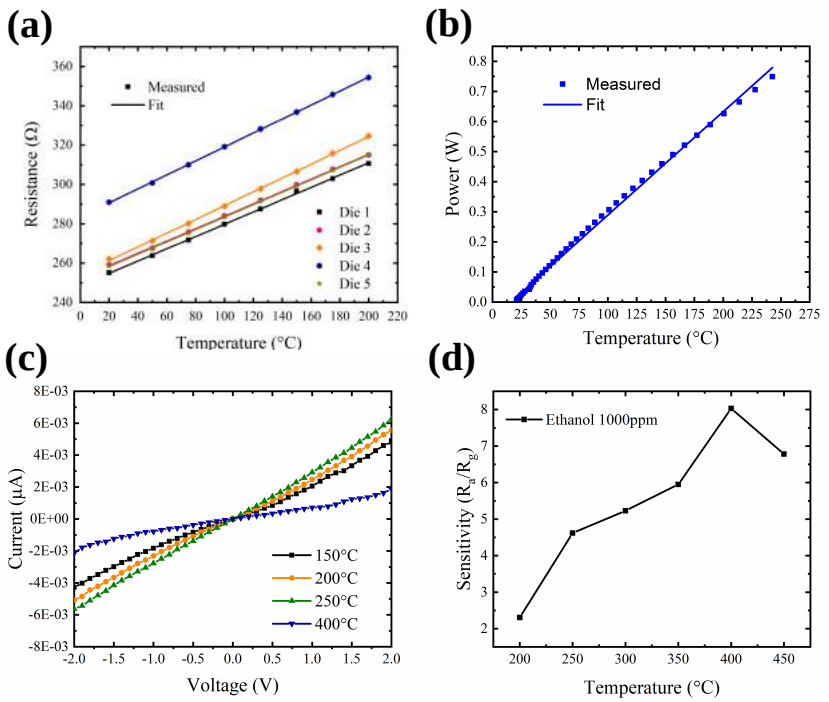

Figure 5.9: (**a**) Microhotplate resistance versus temperature characterisation. (**b**) Power consumption of the bare device versus temperature. (**c**) I-V characteristics of the SnO_2 nanoparticle film at different temperatures. (**d**) Sensing response to 1000ppm of ethanol vapors at different temperatures.

The resistance as a function of the temperature of five TiN/Mo/TiN microhotplate devices is shown in Figure 5.9a. The average resistance of the microhotplate at room temperature (20°C) is 258.60Ω.

The TCR of the devices is calculated by using the equation below[19],

$$\alpha(T) = \frac{R_T - R_0}{R_0 \cdot (T - T_0)} \tag{5.1}$$

where, R_0 is the resistance of the microhotplate at room temperature

(20°C), and R(T) is the resistance of the microhotplate at various measured temperatures from 20°C to 200°C. The TCR of the microhotplate devices is nearly constant ,and the average TCR is 0.000122/°C. From Figure 5.9a, the room temperature of devices has a small variation, mainly caused due to fabrication process variations.

The steady-state power consumption of the microhotplate in the air as a function of temperature is shown in Figure 5.9b. The power consumption of the device to reach a temperature of 100°C and 200°C is 300mW and 625mW, respectively. Using a linear fit as shown in Figure 5.9b, the power consumption of the device for different operating temperatures is extracted. In order to reach an operating temperature of 400°C in the device for sensing response to ethanol, a current of ≈42 mA is passed through the microhotplate, corresponding to the maximum power consumption of ≈1.3 W. The large power consumption in the device is due to the large circular active region of the microhotplate having a diameter of 1.5mm. The large active region of the microhotplate is used to provide a large area for controlled deposition of SnO_2 nanoparticles from the nozzle of the spark discharge chamber. However, utilising a smaller active area and improving the deposition mechanism with a smaller nozzle can reduce the size of the devices, thereby reducing the power consumption.

The temperature calibration of the microhotplate was used to measure the I–V characteristics of SnO_2 nanoparticle film at different operating temperatures in dry air, as shown in Figure 5.9c. It is seen that the current increases as the operating temperature is increased from 150°C and 250°C, but the current is found to be decreasing at the operating temperature of 400°C. This is because, at a lower operating temperatures, the oxygen molecules are mostly physisorbed at the surface of SnO_2 material. However, at higher temperatures in the range around 400°C, the oxygen species such as O_2^-, O^- and O^{2-} are chemisorbed on the surface by the transfer of an electron from the conduction band of the SnO_2 material[27]. Thus, the current decreases, resulting in the increase of resistance of the SnO_2 nanoparticle film in the operating temperature range of 400°C. The sensing response of SnO_2 nanoparticle thin film to ethanol vapors was determined by measuring the time-dependent changes in the resistance at different concentrations of ethanol vapors in dry air. For reducing gases such as ethanol, the sensitivity (S) of the sensor is defined as the ratio of resistance of the SnO_2 nanoparticle film in the air (R_a) to the resistance of SnO_2 nanoparticle film in ethanol (R_g) given by[28],

$$S = \frac{R_a}{R_g} \tag{5.2}$$

Prior to the gas sensing measurements, the sensors were annealed at 500°C for 2 hours in the air. In the next step, the sensing response to 1000ppm of ethanol at different operating temperatures were done to determine the operating temperature at which the maximum response to ethanol can be obtained. The power applied to the microhotplate is varied to obtain a particular tem-

perature. A constant voltage of 2V is applied to the sensing electrodes, and the resistance of SnO_2 at different operating temperatures were measured. The sensitivity of the sensor obtained at different operating temperatures is shown in Figure 5.9d. The sensitivity of the sensor increases as the temperature is increased from 200°C to 400°C. However it decreases at a temperature of 450°C. The maximum response is obtained at 400°C, and this temperature is taken as the operating temperature in further sensing measurements. The rate of adsorption and desorption is constant at temperatures from 200°C to 400°C due to which the sensitivity increases. However, at a temperature higher than 400°C, the rate of desorption is higher than the rate of adsorption that leads to a decrease in the sensor's sensitivity[27].

The sensing response to the increasing concentration of ethanol vapors from 100ppm to 1000ppm in dry air at an operating temperature of 400°C is shown in Figure 5.10a. It is seen that the SnO_2 nanoparticle film is sensitive to a low ethanol concentration of 100ppm, and the sensor response increases with the increasing concentration of ethanol vapors. The sensitivity of the sensor as a function of ethanol concentration is shown in Figure 5.10b. The sensitivity increases rapidly in the ethanol concentration range up to 500ppm. However, at ethanol concentration above 500ppm, the sensitivity of the sensor increases slowly, indicating that the sensor is saturated at a higher ethanol concentration. The sensing response of a metal oxide gas sensor is empirically defined by[27],

$$S = A_g \cdot P_g^{\beta} \tag{5.3}$$

where, P_g is the partial pressure of the target gas directly proportional to the concentration and sensitivity (S) characterized by the prefactor A_g and exponent β. The exponent factor β has a rational fraction value dependent on the charge of the surface species of the metal oxide film and the stoichiometry of the reactions at the surface of the film[29]. For sensing film having an ideal microstructure, the value of $\beta = 0.5$. However, the value of β varies above or below the value of an ideal microstructure. The value of β is higher than 0.5 for sensing film having large randomness and irregularity in the microstructure. On the other hand, sensing films having agglomerates and less sensitive structures, the value of β is less than 0.5[29]. The measured sensor response (S) in the linear region from 100ppm to 500ppm were fitted with the logarithm of the equation 5.3 as shown in Figure 5.10c. The value of (β) obtained from the linear fit is 0.49 +/- 0.01, which is slightly less than the value of (β) for an ideal microstructure, indicating that the presence of agglomerates in the nanoparticle film can influence the sensitivity to ethanol vapors.

The response and recovery of the sensor for multiple exposures to 200ppm ethanol vapor is shown in Figure 5.10d. The response of the sensor is found to be stable for a repeated cycle of ethanol vapors. In the next step, the response time and recovery time of the sensor are determined for different concentrations of ethanol vapors. The response time of the sensor is defined as the time taken to reach 90% of the saturation value. The recovery time is defined as the time taken to reach 10% of the baseline value. The response

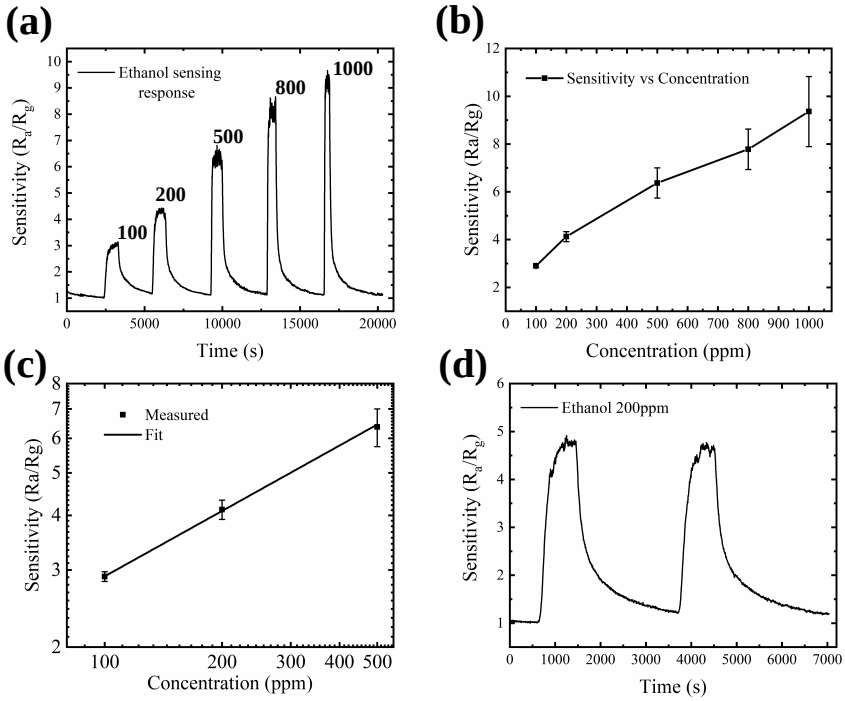

Figure 5.10: (**a**) Sensing response to ethanol vapors from 100ppm to 1000ppm at 400°C. (**b**) Sensitivity versus ethanol concentration from 100ppm to 1000ppm. (**c**) Sensitivity versus ethanol concentration from 100ppm to 500ppm with linear fit. (**d**) Sensing response to 200ppm of ethanol vapors - repeatability test.

time of the sensor for ethanol concentration from 100ppm to 1000ppm is shown in Figure 5.11a. The response time for ethanol vapor concentration of 100ppm is 357s, and it decreases to 107s for 1000ppm of ethanol vapor. The recovery time of the sensor increases with increasing ethanol concentration, as shown in Figure 5.11b. The recovery time is 1394s for ethanol vapor of 100ppm, and it increases to 2410s for 1000ppm of ethanol vapor. The sensor shows a stable and repeatable response to different concentration of ethanol vapors.

The sensitivity of the SnO_2 nanoparticle film to 200ppm and 1000ppm of methanol vapors was tested at 400°C. The comparison between the sensitivity of ethanol and methanol for 200ppm and 1000ppm is shown in Figure 5.11c. It is seen that SnO_2 film is more sensitive to ethanol than methanol, which is in agreement with earlier reported results[30]. The stability of the sensor upon exposure to 1000ppm of ethanol vapors over several days was done, and the result is shown in Figure 5.11d. The sensor is stable within the sensitivity values obtained over a period of 20 days. This shows that the SnO_2 nanoparticle film synthesized by the spark discharge method is a promising material

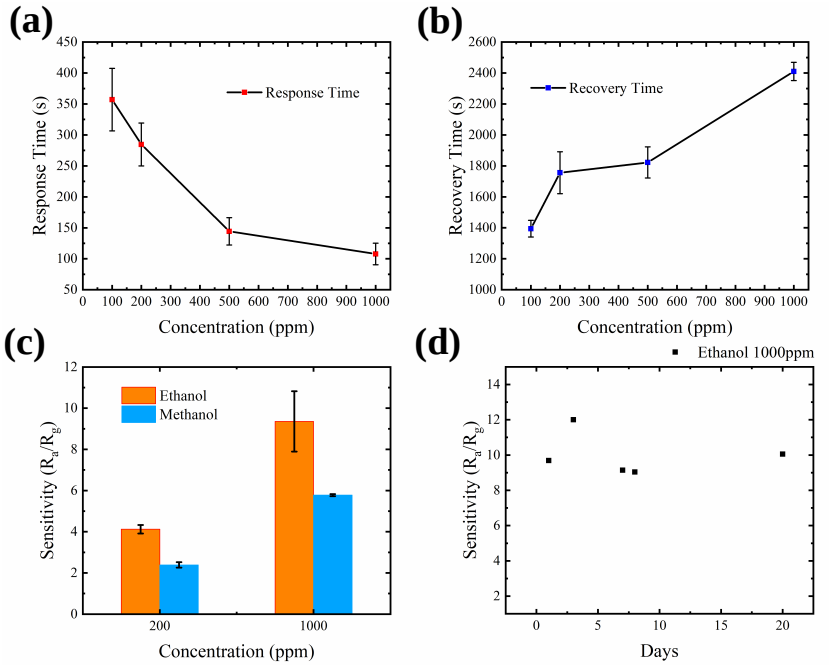

Figure 5.11: (**a**)Response time versus concentration (**b**) Recovery time versus concentration. (**c**) Cross sensitivity between ethanol and methanol vapors at 200ppm and 1000ppm (**d**) Sensor response to 1000ppm ethanol over long period.

for sensing ethanol vapors.

5.3.4. Sensing mechanism of ethanol

The interaction of various gaseous analytes with n-type metal oxides semiconductor such as, SnO_2 mainly occurs in a two-step process. In the first process in dry air, the oxygen species O_2^-, O^- and O^{2-} are chemisorbed on the surface of the film in the temperature ranges from 350°C to 450°C. The transfer of electrons from the conduction band of SnO_2 to the oxygen species results in the formation of a depletion layer thereby increasing the resistance of the film in the steady state in dry air. In the next process, the exposure of SnO_2 material to reducing gases or oxidizing gases varies the resistance. The resistance of SnO_2 film decreases upon exposure to reducing gases such as ethanol or methanol, whereas the resistance increases during exposure to oxidizing gases such as nitric oxide. The reaction mechanism for the formation of the oxygen species is shown below[27][31],

$$O_2 + e^- \longrightarrow O_2^- \tag{5.4}$$

$$O_2^- + e^- \longrightarrow 2\,O^- \tag{5.5}$$

$$O^- + e^- \longrightarrow O^{2-} \tag{5.6}$$

In the next process, the interaction of SnO_2 film with reducing gases such as ethanol leads to the formation of intermediates that react with oxygen species at the surface. The reaction mechanisms of ethanol vapors with SnO_2 nanoparticle film are defined by the below,

$$C_2H_5OH \longrightarrow C_2H_4 + H_2O \tag{5.7}$$

$$C_2H_5OH \longrightarrow CH_3CHO + H_2 \tag{5.8}$$

$$C_2H_4 + 6\,O^- \longrightarrow 2\,CO_2 + 2\,H_2O + 6\,e^- \tag{5.9}$$

$$CH_3CHO + 5\,O^- \longrightarrow 2\,CO_2 + 2\,H_2O + 5\,e^- \tag{5.10}$$

Equation 5.7 and Equation 5.8 are the acidic oxide and basic oxide intermediates formed by the reaction of ethanol vapor with SnO_2 respectively. The reaction mechanisms of the respective intermediates with the oxygen species are described in Equation 5.9 and Equation 5.10. The reaction products are CO_2, H_2O, and free electrons. The electrons trapped within the oxygen species can return to the conduction band of the SnO_2 leading to the decrease in resistance of the SnO_2 film. These changes in resistance for different concentration of ethanol vapors are measured as the sensor response.

5.3.5. Conclusions

In this study, SnO_2 nanoparticle thin film was synthesized by spark discharge of Sn electrodes and deposited on a custom-made TiN/Mo/TiN microhotplate device with integrated Pt sensing electrodes. The deposited SnO_2 nanoparticles are crystalline in nature as characterised by TEM and XRD. Annealing SnO_2 nanoparticles at higher temperatures at higher temperatures result in increased particle sizes and extensive crack formation across the film. An optimised deposition process was developed to enable SnO_2 nanoparticle thin film deposition with reduced cracks on the devices after annealing. The resistance change of the TiN/Mo/TiN microhotplate with temperature is found to be linear, and the average TCR of the microhotplate is 0.000122/°C. The sensitivity of the SnO_2 thin film upon exposure to 1000ppm of ethanol vapors was highest at 400°C. The SnO_2 thin film shows a stable and reversible response to ethanol vapors in dry air in the concentration range from 100ppm to 1000ppm. The response time and recovery time of the sensor are 357s and 1394s for ethanol concentrations of 100ppm and 1000ppm, respectively. Cross-sensitivity studies with methanol and ethanol vapors show that the SnO_2 thin film is more sensitive to ethanol than methanol vapors. The spark discharge method can be

used to study the properties of mixed metal-oxide nanoparticles using two or more different electrodes for gas sensing application. The ability to accurately deposit on the surface of MEMS sensor devices without additional tool and process steps allows the integration of different nanoparticles for developing a MEMS gas sensor array.

References

[1] P. WOLKOFF, *Volatile organic compounds sources, measurements, emission, and the impact on indoor air quality,* Indoor Air, 1995 (1995).

[2] A. Bacaloni, S. Insogna, and L. Zoccolillo, *Indoor air quality. volatile organic compounds: Sources, sampling and analysis,* in *Chemistry, Emission Control, Radioactive Pollution and Indoor Air Quality* (IntechOpen, 2011).

[3] T. Lin, X. Lv, Z. Hu, A. Xu, and C. Feng, *Semiconductor metal oxides as chemoresistive sensors for detecting volatile organic compounds,* Sensors **19**, 233 (2019).

[4] Q. Wan, Q. Li, Y. Chen, T.-H. Wang, X. He, J. Li, and C. Lin, *Fabrication and ethanol sensing characteristics of zno nanowire gas sensors,* Applied Physics Letters **84**, 3654 (2004).

[5] A. Umar, A. A. Ibrahim, U. T. Nakate, H. Albargi, M. A. Alsaiari, F. Ahmed, F. A. Alharthi, A. A. Alghamdi, and N. Al-Zaqri, *Fabrication and characterization of cuo nanoplates based sensor device for ethanol gas sensing application,* Chemical Physics Letters **763**, 138204 (2021).

[6] T. T. Nguyen, H.-N. Choi, M. J. Ahemad, D. Van Dao, I.-H. Lee, and Y.-T. Yu, *Hydrothermal synthesis of in2o3 nanocubes for highly responsive and selective ethanol gas sensing,* Journal of Alloys and Compounds **820**, 153133 (2020).

[7] A. Sharma, A. Ahmed, A. Singh, S. Oruganti, A. Khosla, and S. Arya, *Recent advances in tin oxide nanomaterials as electrochemical/chemiresistive sensors,* Journal of the Electrochemical Society (2021).

[8] T. Miller, S. Bakrania, C. Perez, and M. Wooldridge, *Nanostructured tin dioxide materials for gas sensor applications,* Functional Nanomaterials **30**, 1 (2006).

[9] N. Yamazoe, *New approaches for improving semiconductor gas sensors,* Sensors and Actuators B: Chemical **5**, 7 (1991).

[10] D. Mohanta and M. Ahmaruzzaman, *Tin oxide nanostructured materials: an overview of recent developments in synthesis, modifications and potential applications,* RSC advances **6**, 110996 (2016).

[11] G. Biskos, V. Vons, C. U. Yurteri, and A. Schmidt-Ott, *Generation and sizing of particles for aerosol-based nanotechnology,* KONA Powder and Particle Journal **26**, 13 (2008).

[12] N. S. Tabrizi, M. Ullmann, V. Vons, U. Lafont, and A. Schmidt-Ott, *Generation of nanoparticles by spark discharge,* Journal of Nanoparticle Research **11**, 315 (2009).

[13] N. A. Isaac, M. Valenti, A. Schmidt-Ott, and G. Biskos, *Characterization of tungsten oxide thin films produced by spark ablation for no2 gas sensing,* ACS applied materials & interfaces **8**, 3933 (2016).

[14] A. Vasiliev, A. Varfolomeev, I. Volkov, P. Arsenov, A. Efimov, V. Ivanov, A. Pislyakov, A. Lagutin, and T. Maeder, *Gas sensor with reduced humidity response based on metal oxide nanoparticles synthesized by spark discharge,* Oriental Journal of Chemistry **34**, 648 (2018).

[15] A. Efimov, I. Volkov, A. Varfolomeev, A. Vasiliev, and V. Ivanov, *Tin oxide nanoparticles produced by spark ablation: Synthesis and gas sensing properties,* Orient. J. Chem **32**, 2909 (2016).

[16] A. A. Efimov, I. A. Volkov, V. Ivanov, A. A. Vasiliev, A. Varfolomeev, A. V. Pislyakov, A. S. Lagutin, and T. Maeder, *Spark discharge synthesis of semiconductor nanoparticles for thick-film metal oxide gas sensors,* Procedia Engineering **168**, 1036 (2016).

[17] P. Bhattacharyya, *Technological journey towards reliable microheater development for mems gas sensors: a review,* IEEE Transactions on Device and Materials Reliability **14**, 589 (2014).

[18] A. Pike and J. W. Gardner, *Thermal modelling and characterisation of micropower chemoresistive silicon sensors,* Sensors and Actuators B: Chemical **45**, 19 (1997).

[19] L. Mele, F. Santagata, E. Iervolino, M. Mihailovic, T. Rossi, A. Tran, H. Schellevis, J. Creemer, and P. Sarro, *A molybdenum mems microhotplate for high-temperature operation,* Sensors and Actuators A: Physical **188**, 173 (2012).

[20] J. Creemer, D. Briand, H. Zandbergen, W. Van der Vlist, C. De Boer, N. F. de Rooij, and P. Sarro, *Microhotplates with tin heaters,* Sensors and Actuators A: Physical **148**, 416 (2008).

[21] B. Zhang, J. Wei, A. J. Böttger, H. W. van Zeijl, P. M. Sarro, and G. Zhang, *Mems enabled fast time-resolved x-ray diffraction characterization platform for copper nanoparticle sintering in heterogeneous integration applications,* in *2019 20th International Conference on Solid-State Sensors, Actuators and Microsystems & Eurosensors XXXIII (TRANSDUCERS & EUROSENSORS XXXIII)* (IEEE, 2019) pp. 1772–1775.

[22] B. Zhang, *Low temperature sintering of copper nanoparticles: Mechanism and die attach application*, Ph.D. thesis, Delft University of Technology (2020).

[23] F. P. Incropera, A. S. Lavine, T. L. Bergman, and D. P. DeWitt, *Fundamentals of heat and mass transfer* (Wiley, 2007).

[24] M. J. Madou, *Fundamentals of microfabrication: the science of miniaturization* (CRC press, 2002).

[25] VSPARTICLE, *Vsp-g1 nanoparticle generator,* `https://vsparticle.com/products/vsp-g1-nanoparticle-generator`.

[26] M. P. Subramaniam, G. Arunachalam, R. Kandasamy, P. Veluswamy, and I. Hiroya, *Effect of ph and annealing temperature on the properties of tin oxide nanoparticles prepared by sol–gel method,* Journal of Materials Science: Materials in Electronics **29**, 658 (2018).

[27] S. Santra, A. Sinha, A. De Luca, S. Ali, F. Udrea, P. Guha, S. Ray, and J. Gardner, *Mask-less deposition of au–sno2 nanocomposites on cmos mems platform for ethanol detection,* Nanotechnology **27**, 125502 (2016).

[28] M. Kennedy, F. Kruis, H. Fissan, B. Mehta, S. Stappert, and G. Dumpich, *Tailored nanoparticle films from monosized tin oxide nanocrystals: particle synthesis, film formation, and size-dependent gas-sensing properties,* Journal of Applied Physics **93**, 551 (2003).

[29] R. W. Scott, S. Yang, G. Chabanis, N. Coombs, D. Williams, and G. Ozin, *Tin dioxide opals and inverted opals: near-ideal microstructures for gas sensors,* Advanced Materials **13**, 1468 (2001).

[30] H. Gong, Y. Wang, S. Teo, and L. Huang, *Interaction between thin-film tin oxide gas sensor and five organic vapors,* Sensors and Actuators B: Chemical **54**, 232 (1999).

[31] S. Mishra, C. Ghanshyam, N. Ram, S. Singh, R. Bajpai, and R. Bedi, *Alcohol sensing of tin oxide thin film prepared by sol-gel process,* Bulletin of Materials Science **25**, 231 (2002).

6

Summary

A MEMS gas sensor consists of a transducer, mainly a resistive or capacitive transducer coated with a thin film of specific functional materials. Functional materials can change their electrical, optical, magnetic, or mechanical properties based on the stimuli received. In a chemi-resistive or chemi-capacitive gas sensing system, thin film of functional materials coated on the transducers are a class of materials that can change the resistivity or dielectric properties of the adsorption or chemisorption of volatile organic compounds such as methanol and ethanol. A combination of efficient design of the MEMS transducer, read-out system, and robust sensing material is a key requirement for the development of good and reliable sensors. In this thesis, the study of thin-film dielectric and semiconducting nanoparticles integrated on MEMS transducers for the detection of volatile organic compounds (VOCs), namely ethanol and methanol vapors are presented.

In Chapter 2, the in-situ electrochemical growth of CuBTC MOFs, as an affinity layer, directly on custom-fabricated Cu Interdigitated Electrodes (IDEs), acting as a transducer. Crystalline affinity layers of 5-7μm height were grown on IDEs with a width and a gap of both 50μm, a height of 6-8μm and 100 electrodes. These capacitive sensors were exposed to methanol and water vapor at 30°C. The affinities showed to be completely reversible with higher affinity towards water compared to methanol. For exposure to 1000ppm methanol, a fast response was observed with a capacitance change of 5.57pF at equilibrium. The observed capacitance change with methanol concentration followed nicely a Langmuir adsorption isotherm, from which was deduced a value for the equilibrium affinity K_e=174.8 bar^{-1}. The CuBTC thin affinity layer on the Cu-IDEs show fast, reversible, and sensitive response to methanol and water vapor making quantitative detection in the range of 100-8000ppm possible.

In Chapter 3, capacitors made of interdigitated electrodes (IDEs) as a transducer platform for the sensing of volatile organic compounds (VOCs)

have advantages due to their lower power operation and fabrication using standard micro-fabrication techniques. Integrating a micro-electromechanical system (MEMS), such as a microhotplate with IDE capacitor, further allows study of the temperature-dependent sensing response of VOCs In this paper, the design, fabrication, and characterization of a low-power MEMS microhotplate with IDE capacitor to study the temperature-dependent sensing response to methanol using Zeolitic imidazolate framework (ZIF-8), a class of metal-organic framework (MOF), is presented. A Titanium nitride (TiN) microhotplate with aluminum IDEs suspended on a silicon nitride membrane is fabricated and characterized. The power consumption of the ZIF-8 MOF-coated device at an operating temperature of 50 °C is 4.5 mW and at 200 °C it is 26 mW. A calibration methodology for the effects of temperature of the isolation layer between the microhotplate electrodes and the capacitor IDEs is developed. The device coated with ZIF-8 MOF shows a response to methanol in the concentration range of 500 ppm to 7000 ppm. The detection limit of the sensor for methanol vapor at 20 °C is 100 ppm. In situ study of sensing properties of ZIF-8 MOF to methanol in the temperature range from 20 °C to 50 °C using the integrated microhotplate and IDE capacitor is presented. The kinetics of temperature-dependent adsorption and desorption of methanol by ZIF-8 MOF are fitted with double-exponential models. With the increase in temperature from 20 °C to 50 °C, the response time for sensing of methanol vapor concentration of 5000 ppm decreases by 28%, whereas the recovery time decreases by 70%.

In Chapter 4, the development of porous organic framework as affinity layer for capacitive vapor sensing are discussed. Porous Organic framework (POF) are microporous polymers that show the capability for adsorbing of volatile organic compounds such as ethanol and methanol. Integrating such POFs as affinity layer on capacitive transducer such as interdigitated electrodes can be operated as chemicapacitor sensors towards VOCs. In this work, melamine based POF were synthesised and deposited on aluminum IDE capacitor devices. The POF coated device have good and repeatable sensing response towards vapors of ethanol and methanol in a large dynamic range from 500ppm to 7000ppm. Cross-sensitivity studies in the presence of watervapor indicate that the sensors can be operated in the presence of moisture without hindering the sensor response. The capability of room temperature detection of ethanol and methanol vapors further enable development of POF based sensors for low power gas sensor systems.

In Chapter 5, SnO_2 nanoparticles are synthesized by spark discharge method in this work, and the sensing response to ethanol vapors is demonstrated. The particle size, crystal structure, and morphology are studied by transmission electron microscopy, X-ray diffraction, and scanning electron microscopy. The as-deposited primary particles are having a size ranging from 4 to 6nm. The design, fabrication, and characterisation of TiN/Mo microhotplate with Pt electrodes platform for depositing SnO_2 nanoparticles for sensing studies is presented. The deposition parameters of SnO_2 nanoparticle film are optimised

to achieve a deposition of a uniform thin film across the sensing electrodes. The sensitivity of the sensor during exposure to 100ppm and 1000ppm of ethanol vapors in dry air at 400°C is 2.89 and 9.3, respectively. The response time for 100ppm and 1000ppm of ethanol vapors are 327s and 107s, respectively. The SnO_2 nanoparticle film shows a stable and reversible response to ethanol concentration from 100ppm to 1000ppm. The flexible and facile synthesis of nanoparticles by spark discharge method and integration of the nanoparticle thin film directly on MEMS devices show promise in developing MEMS sensor arrays for multi-gas sensing application.

Acknowledgements

Over the course of the Phd project, I had a good learning experience in functional materials, MEMS device development and characterisation, integration and testing of the sensors towards methanol and ethanol vapors. I would like to thank Prof Kouchi Zhang for providing me the opportunity to work in the Phd research project in ECTM-BRC group, for constant support and motivation to work on this research project. I would like to thank my supervisors Dr Andre Bossche, Dr Jia Wei for their support and supervision in the project. A special thanks to Dr Jia Wei for the reviews and daily discussions in improvements in the technical areas of the project. I would also like to thank Dr Fabio Santagata and Dr Elina Iervolino for their support during the initial phase of the project. The development of a gas sensor is a multi-disciplinary project and it requires co-ordination with multiple groups towards a successful research project. During the course of the project, the coordination and support of the Organic Materials and Interfaces(OMI) group, Department of Chemical engineering, TUDelft has helped immensely in the completion of this research project. I would like to thank Dr Sumit Sachdeva, Duco Bosma, Prof Louis de Smet and Prof Ernst J.R. Sudhölter for their kind guidance and support in the utilisation of the gas sensor testing facilities.

The coordination and fruitful technical discussions with the members of the ECTM group and EKL had been of immense help during the course of my research project. I would like to thank Prof Lina Sarro, Dr Sten Vollebregt for providing me opportunity to be teaching assistant of the IC Technology course. At EKL, technical discussions with Dr Gregory Pandraud, Johannes van Wingerden, Silvana Milosavljevic helped me in the development of the MEMS microhotplate devices. Within ECTM group, I would like to thank Dr Rene Poelma, Dr Henk van Zeijl, Dr Boyao Zhang, Dr Brahim El Mansouri, Dr Luke Middelburg, Dr Daniel Yi, Dr Robert Sokolovskij, Dr Zahra Kolahdouz Esfahani, Dr Cinzia Silvestri, Joost van Ginkel for their kind technical support and discussions. A special thanks to Marian for helping in the administrative process and documentations.

List of Publications

Patent

1. Santagata ,Fabio, Iervolino, Elina,Dong, Mingzhi, **Venkatesh, Manjunath Ramachandrappa**, Zhang, Guoqi *INTELLIGENT MULTI-FUNCTIONAL ELECTRONIC DEVICE*, WO/2017/045606, 03-23-2017.

Publications

1. **Venkatesh, M.R.**; Max Koole; Boyao Zhang; Sumit Sachdeva; Wei, J.; Joost van Ginkel; Bossche, A.; Zhang, G.Q. "A facile, rapid and green synthesis of tin oxide nanoparticle thin film produced by Spark Ablation for MEMS ethanol sensor", *MDPI Sensors*, *To be Submitted*.

2. **Venkatesh, M.R.**; Sumit Sachdeva; Wei, J.; Bossche, Zhang, G.Q.; de Smet, L.; J.R. Sudhölter, E. "Porous Organic Frameworks (POFs) as affinity layers for capacitive vapour sensing" *MDPI Sensors*, *To be Submitted*.

3. **Venkatesh, M.R.**; Sumit Sachdeva; Wei, J.; Bossche, Zhang, G.Q.; de Smet, L.; J.R. Sudhölter, E. "A low-power MEMS Capacitive sensor with Integrated Microhotplate: Application as Methanol Sensor using a Metal-Organic Framework Coating as Affinity Layer" *MDPI Sensors - Special Issue* **2019**.

4. Sachdeva, S.; **Venkatesh, M.R.**; Mansouri, B.E.; Wei, J.; Bossche, A.; Kapteijn, F.; Zhang, G.Q.; Gascon, J.; de Smet, L.; J.R. Sudhölter, E. "Sensitive and reversible detection of methanol and water vapor by in situ electrochemically grown CuBTC MOFs on interdigitated electrodes". *Small* **2017**, *13*, 1604150 **Co-First Author, Front Cover Article**.

5. **Manjunath.R.Venkatesh**, Mansouri, Brahim El,Wei, Jia ,Bossche, Andre, G.Q.Zhang, "Electro-thermal analysis and design of a combined MEMS impedance and micro-hotplate device for gas sensing applications". *Thermal, Mechanical and Multi-Physics Simulation and Experiments in Microelectronics and Microsystems (EuroSimE),* **2016**, 17th International Conference on. IEEE, 2016, pp. 1–9.,

6. Zhang, G. Q., H. van Zeijl, W. D. van Driel, R. Poelma, Z. K. Esfahani, **M. R. Venkatesh**, L. Middelburg, and B. El Mansouri, "Smart Systems Integration in the era of Solid State Lighting." *SSI 2017*

7. Pan Liu, Henk van Zeijl, **Manjunath.R.Venkatesh**, Manjunath R Venkatesh, Robert Sokolovskij, Ralph Kurt, Guoqi Zhang , "Review on Retrofit G4 LED Lamps: Technology, Challenges, and Future Trends". *IEEE ECTC 2015*

8. **Manjunath.R.Venkatesh**, P.Liu, H.W.van Zeijl, G.Q.Zhang, "Modelling and Simulation of monolithic integration of rectifiers for solid state lighting applications". *presented in EuroSimE 2014 - IEEE International Conference on Thermal, Mechanical and Multi-Physics Simulation and Experiments in Microelectronics and Microsystems,*